Strojniški vestnik

Journal of Mechanical Engineering

no. 1
year 2018
volume 64

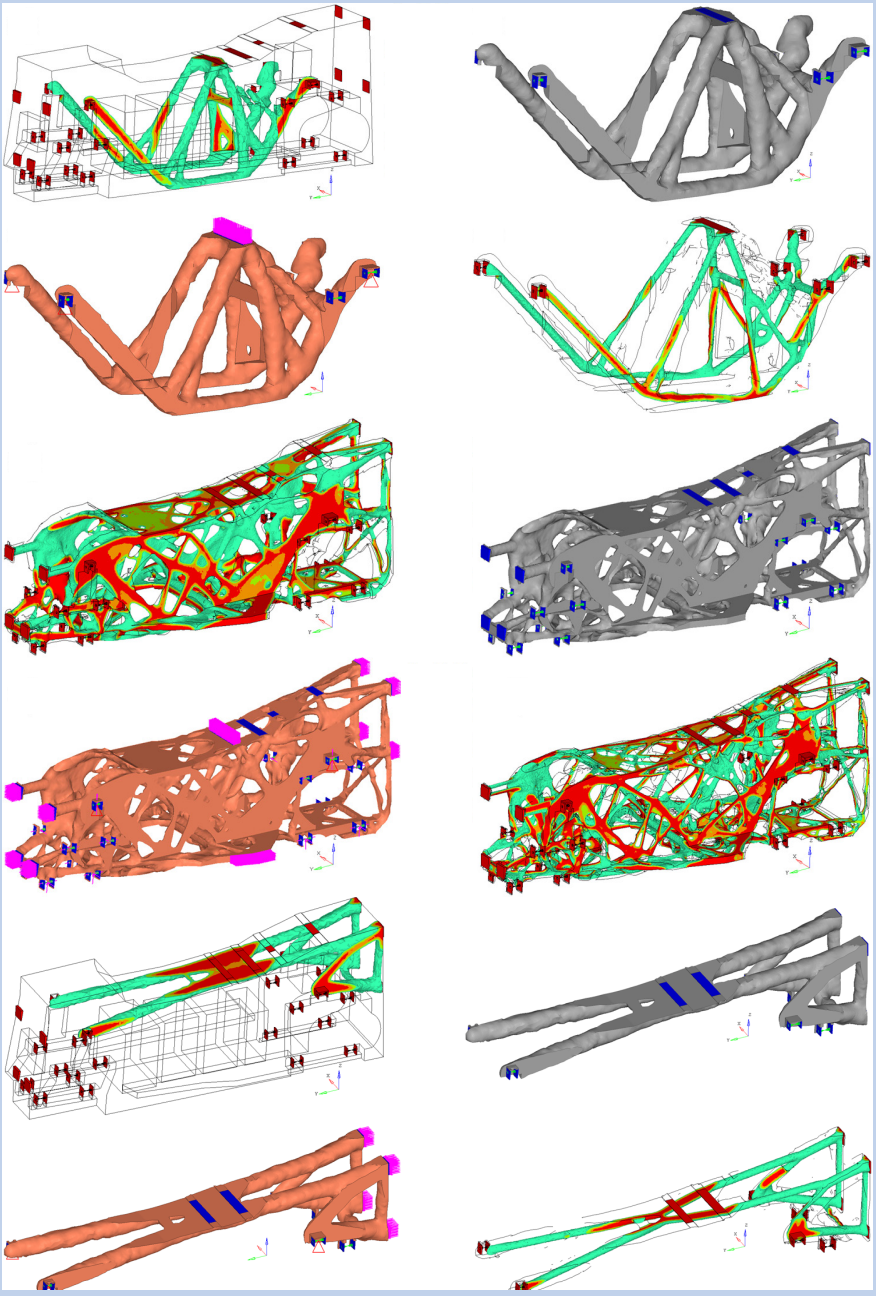

Strojniški vestnik – Journal of Mechanical Engineering (SV-JME)

Aim and Scope

The international journal publishes original and (mini)review articles covering the concepts of materials science, mechanics, kinematics, thermodynamics, energy and environment, mechatronics and robotics, fluid mechanics, tribology, cybernetics, industrial engineering and structural analysis.

The journal follows new trends and progress proven practice in the mechanical engineering and also in the closely related sciences as are electrical, civil and process engineering, medicine, microbiology, ecology, agriculture, transport systems, aviation, and others, thus creating a unique forum for interdisciplinary or multidisciplinary dialogue.

The international conferences selected papers are welcome for publishing as a special issue of SV-JME with invited co-editor(s).

Editorial Office

University of Ljubljana, Faculty of Mechanical Engineering

SV-JME, Aškerčeva 6, SI-1000 Ljubljana, Slovenia

Phone: 386 (0)1 4771 137

Fax: 386 (0)1 2518 567

info@sv-jme.eu, http://www.sv-jme.eu

Print: Abografika, printed in 300 copies

Founders and Publishers

University of Ljubljana, Faculty of Mechanical Engineering, Slovenia

University of Maribor, Faculty of Mechanical Engineering, Slovenia

Association of Mechanical Engineers of Slovenia

Chamber of Commerce and Industry of Slovenia, Metal Processing Industry Association

Cover: The material density distributions, derived geometry, FEM models and calculation results of the topology optimization runs for a new electrified quad structure that were obtained by applying the methodology of the assessment of load case influences and the multiple run approaches within the conceptual design phase of the Integrative CAE-Driven Design Process. The first four figures (from left to the right) exemplify the first and the second calculation run for the bending load case, the central four figures represent the second and third calculation run for the combined load cases, and the last four figures reveal the first and the second calculation run for the static crash rear load case.

Image Courtesy: Virtual Vehicle Research Center, Dept. Integrated Vehicle Development, Austria

General information

Strojniški vestnik – Journal of Mechanical Engineering is published in 11 issues per year (July and August is a double issue).

Institutional prices include print & online access: institutional subscription price and foreign subscription €100,00 (the price of a single issue is €10,00); general public subscription and student subscription €50,00 (the price of a single issue is €5,00). Prices are exclusive of tax. Delivery is included in the price. The recipient is responsible for paying any import duties or taxes. Legal title passes to the customer on dispatch by our distributor.

Single issues from current and recent volumes are available at the current single-issue price. To order the journal, please complete the form on our website. For submissions, subscriptions and all other information please visit: *http://en.sv-jme.eu/.*

You can advertise on the inner and outer side of the back cover of the journal. The authors of the published papers are invited to send photos or pictures with short explanation for cover content.

We would like to thank the reviewers who have taken part in the peer-review process.

ISSN 0039-2480

The journal is subsidized by Slovenian Research Agency.

Strojniški vestnik - Journal of Mechanical Engineering is available on http://www.sv-jme.eu, where you access also to papers' supplements, such as simulations, etc.

Contents

Strojniški vestnik - Journal of Mechanical Engineering
volume 64, (2018), number 1
Ljubljana, January 2018
ISSN 0039-2480

Published monthly

Papers

Strojniški vestnik - Journal of Mechanical Engineering 64(2018)1, 3-16

DOI:10.5545/sv-jme.2017.4489 Original Scientific Paper
Received for review: 2017-03-29
Received revised form: 2017-06-15
Accepted for publication: 2017-08-29

Integrative CAE-Driven Design Process in the Embodiment Design Phase of L7e Vehicle Structures

Roman Pawel Jedrzejczyk[1,*] – Michael Sigmar Alb[1,2] – Thomas Jost[1]

[1] Virtual Vehicle Research Center, Austria
[2] University of Padova, Italia

In the past decade, the mechanical engineering industry has searched for a design methodology that could systematically unify the support of computer-aided engineering (CAE) tools for the design process. More recently, some propositions have been put forward for the CAE-driven design process (CDDP), but the efficiency of these design processes is questionable. We have proposed improvements and new arrangements that result in the integrative CDDP (ICDDP), which makes CDDP more reliable, efficient and predictive. The ICDDP redefines the role of CAE tools and positions the optimization technology as a fundamental driving force behind the whole design process. Consequently, the ICDDP orders design phases as: (1) conceptual design, (2) design crystallization and (3) design sophistication, which steer the design process sequentially. The accurately established linkages between the sequential design steps enhance the smooth recurrence of the ICDDP for new product executions. In addition, this work demonstrates the application of the conceptual design phase to design a new L7e (eQuad) vehicle structure. This phase of the ICDDP illustrates the specific steering methodology for the topology optimization of a new eQuad structure as well as the geometric solution derivation step that reveals the transformation of bionic shapes into rough manufacturable geometry. Additionally, the numerical verification of the simple geometric model is presented for the load cases given. Our results exemplify the fact that the ICDDP allows engineers to design new innovative and lightweight structures.

Keywords: CAE-driven design, L7e vehicle structure, conceptual design, topology optimization, lightweight design, geometric solution derivation

Highlights

- *A design process that applies the concept of CAE-driven design is presented for new lightweight structures.*
- *The explanation of optimization technologies that depicts the driving force behind CAE-driven design.*
- *One of the first applications of the Integrative CAE-driven design process is proved for the embodiment design phase of the L7e vehicle structure.*

0 INTRODUCTION

Over the last years, the idea of a simulation-driven design process has emerged **[1]**. The simulation-driven design process also includes the computer-aided engineering (CAE)-driven design process (CDDP). The CDDP offers a combination of simulation tools along with an adoptable and systematic approach to the design process. This combination enhances the possibility of applying as many simulation tools as necessary and enables designers to take advantage of reliable simulation methods. Sellgren **[1]** postulated that in major steps of the design process, computer-based modelling and simulations could support and provide the necessary information to reduce the working time.

Engineers and designers can profit from the CDDP by tailoring the design process to their needs. However, the broad definition of design sequence steps for a design process is usually poor and generic and only insufficiently link the design steps within the entire process. As a result, there are many examples of CDDPs that attempt to concretize the meaning of the CDDP idea but do so in different ways **[2]** to **[4]**. Some efforts focus on the application of numerous simulation tools; others search for solutions in a combination of optimization technology with different simulation environments. Moreover, existing examples are quite incomplete regarding a whole design process. These examples of existing CDDPs only cover a part of the design process, thereby reducing their usefulness for engineers and designers.

While CDDPs may allow for a considerable time reduction in the development process, unintegrated CDDPs need to be rearranged whenever the development of a new product or item takes place **[5]**. As a result, an additional amount of working time is required for the ad-hoc planning of suitable design processes. Such unintegrated CDDPs aggravate the risks of introducing inadequate design steps for the development of new products that can have fatal financial consequences for the project budget.

The development of modern lightweight items or structures often demands the application of many different CAE tools. Generic CDDPs enable engineers to combine several simulation and optimization tools from different suppliers within one CDDP. On the other hand, such combinations frequently result in the

*Corr. Author's Address: Virtual Vehicle Research Center, Inffeldgasse 21/A, 8010 Graz, Austria, RomanPawel.Jedrzejczyk@v2c2.at

unintended regeneration of data exchange interfaces because of deviation in the data exchange process [6]. The revisions of interfaces can easily happen if new applications of well-known design solutions occur. Every time a new assemblage of the design tools takes place, it reduces the predictability of the design process. Moreover, several types of simulation and optimization tools increase the cost of the design process that includes additional expenses for new licenses and maintenance of simulation software, user training, etc. The licensing and maintaining of CAE software can cost considerably more than required for hardware [7]. In addition, the cost of training for the inexperienced or unfamiliar users of CAE software also remains high. The costs of user training add to the expenses of extra working time [8].

In this paper, we define the design process that employs the OptiStruct® software from the Altair® company, which links the existing tools in a specific way. The OptiStruct® software provides a variety of simulation and optimization tools for CAE applications. In this paper, we define repeatable linkages to the CDDP and the sequence of design steps to allow generalizations about the whole design process in other applications. Furthermore, we show the impact of our integrative CDDP (ICDDP) that demonstrates how the ICDDP can be implemented in structure design to fulfills its promises.

Additionally, we describe the first part of this ICDDP for topology optimization in the early embodiment design phase. Utilizing a real use case for the structure of the L7e vehicle class, we illustrate the universal character of our ICDDP that is suitable not only for automotive applications, but can be employed in many different fields of mechanical engineering such as rail, aerospace, and light and heavy machinery. The real use case of the L7e vehicle class exploits the reusable nature of the ICDDP because of the highly demanding nature of design processes in the automotive industry.

1 INTEGRATIVE CAE-DRIVEN DESIGN PROCESS

1.1 Deriving Requirements for the ICDDP

The CDDP is expected to improve the design process efficiency of new items and products, time and cost reduction. In consequence, different modelling and simulation types, such as computer-aided design (CAD), CAE, the finite element method (FEM) and computational fluid dynamics (CFD), need to be joined within one simulation environment [9]. Virtual methodologies, which are the foundation of the CDDP, magnify the possibility of recognizing and avoiding errors and mistakes during the design process, thus helping to create innovative products [6]. The CDDP allows for systematic and ordered project structures that reduce project costs, and time-to-market as well as ensuring the achievement of project goals.

Modern consumer goods, such as passenger vehicles, compete with each other for low final prices with many potential buyers. Nevertheless, extensive requirements in legal, technological, environmental, aesthetical (styling) and disposal areas complicate the design process. A new vehicle, for instance, should satisfy the occupant safety regulations [10] and [11] while allowing for reduced energy consumption [12] and [13]. Such requirements often invite competing solutions. Increases in occupant safety demand a tougher structure, which leads directly to an increase in vehicle mass. But the reduction in vehicle energy consumption can be realized mostly through mass reduction. Additionally, the shapes of the new vehicle body-in-white parts such as swooping rooflines, wheel covers and housings, extra front and rear spoilers, and rear wings, have a significant impact on the aerodynamic drag, which plays a crucial role in the development of energy-efficient commuter and premium luxury vehicles as well as track-oriented sports cars [14]. The lightweight body-in-white constructions frequently utilize a mix of various material types, which results in advanced joining technology such as adhesive bonding, rivets and blind-rivet joints, yet the fatigue life estimation is complicated for these types of connections [15]. To match these divergent demands, the optimization process should be applied during design and development [16]. Using different optimization methods, optimal solutions can be found for specific sets of requirements for example for structure design, noise, vibration and harshness, as well as suspension design in the new vehicle development process.

Consequently, Sjödin [2] presented the idea that multi-disciplinary optimization together with CAE methodology can support the design process. This approach enables the optimization of various sub-problems in the vehicle development by applying many simulation and optimization tools whenever they are necessary. Moreover, the application of the CDDP is defined overly widely. In consequence, the linkages between the steps of the CDDP are unclear and mostly insufficient.

Compared to Sjödin's idea, Konzelmann et al. [3] and Münster and Schäffer [4] considered the early design phase and arrangement of design steps for the development process. In this case, the CDDP is a

part of the vehicle development process that involves many small and different design processes. As a result, the linkages of the design steps and operations are defined freely, which can raise design uncertainty during project executions. Additionally, the widely defined backbone of the CDDP and an extensive range of different software and tools amplify a risk of the process interfaces' regeneration.

In recent years, the duration of automotive development cycles has been significantly reduced [17]. For this reason, the industry [18] and [19] requires a simple and universal methodology for the CDDP that easily adapts to specific industrial conditions and needs.

If the CDDP is defined and executed in a correct manner, it can fulfills the promises made. To obtain the full advantages of the CDDP, it is necessary to analyse the following questions first:

- What is needed for the CDDP to guarantee its unquestioned efficiency?
- How should the CDDP be defined to obtain a new lightweight structure?
- What should the first step of the CDDP be to design a new structure from scratch?

The next section of this paper provides the answers to these questions.

1.2 Description of the ICDDP

A frequently used approach for the design process of new structures is based on the VDI 2221-2223 Guidelines [20] to [22]. This approach utilizes the following four steps for the product development phase:

1. planning and task clarification,
2. conceptual design,
3. embodiment design, and
4. detail design.

These four steps represent a necessary effort for investment in a new product [5]. The planning and task clarification (Step 1) and conceptual design (Step 2) are relatively inexpensive compared to the embodiment design (Step 3) and detail design steps (Step 4) [23] and [24]. The effort of the two last development steps requires smart and innovative methodology.

The main idea of the ICDDP is based on the analysis of the current development processes for a new structure. This analysis identified three fundamental engineering areas:

- design (construction and manufacturing rules),
- simulation, and
- optimization.

The design constitutes the development process that applies the design principles including material selections, the way of construction, production costs etc., whereas the simulation (FEM, CFD, etc.) offers various methods for virtual analysis. Optimization technology matches the different opposing requirements and is the driving force of the ICDDP behind the whole development. Impulses to generate new ideas or review current ones result from the iterative nature of the optimization methodology. Therefore, the optimization technology becomes the driving force behind the ICDDP, depicted in Fig. 1.

The critical innovations, which the ICDDP brings to the whole design process with the optimization technology as a driving force, are the design operations sequences.

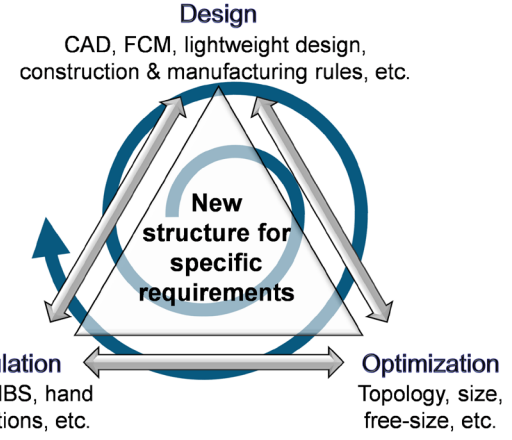

Fig. 1. *Optimization as a driving force behind the ICDDP*

In addition, the requirements and specifications, as well as the assessment of the current structure state (if available), should be available at the beginning of the development process [20]. This information helps to model the non-design areas, technological openings, and types of acting loads. Fig. 2 depicts the development steps of the ICDDP. The ICDDP is divided into three main phases: 1) conceptual design, 2) design crystallization, and 3) design sophistication.

The conceptual design phase starts the ICDDP and consists of two development steps: design space definition and model building, which are also the steps of a topology optimization (TO). The design space definition sets the boundaries for an available space for material utilization and defines rough geometric contours of new structures. In the model-building step, a simulation model containing the load case definitions is established and surrogate load cases, which consider the requirements for a new structure, can be defined. The design space definition and

model building steps follow sets of technical and non-technical specifications for a new structure that results in an FE model for the TO. The link between the conceptual design and design crystallization phases is the geometric solution derivation. This step allows engineers to transform the bionic shapes from the TO into simple engineering-based geometric elements, such as beams (profiles) and plates. The geometric solution derivation offers the opportunity to interpret the TO results precisely.

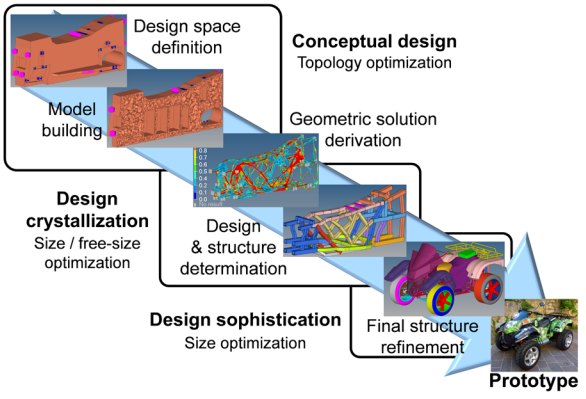

Fig. 2. *ICDDP – steps and main development phases*

The first draft design, which consists of beams and plates, takes shape in the design crystallization phase. During this phase, the size / free-size optimization methods permit engineers to discuss structure body-in-white types that crystallize the design of a new structure together with an analysis of different materials such as isotropic and orthotropic. The discussion of structure body-in-white types, which allows for the customization of a new structure, enables design proposals to be formulated. We are carrying out the ongoing scientific investigation of this topic.

More importantly, this step of the design crystallization phase determines the structure body-in-white types, material types for fundamental members (profiles and plates) and production (assembly) methods. Accordingly, the design sophistication phase strengthens a final structure refinement. In this stage, the size optimization enhances a new structure that arises in the second step as a combination of the best solutions for a specific given value of max stress, strain, etc. This enhancement involves sizing for the dimensions of profiles and plates. As a result, the ICDDP ultimately provides a new structure: a prototype for given sets of requirements and specifications.

Fig. 3 illustrates the design principles and approaches throughout the steps and main development phases of the ICDDP. For each design sequence in the ICDDP, Fig. 3 presents the necessary inputs, design actions and tools (including optional tools) as well as objectives that shape a new structure design incrementally and efficiently. These design sequences of the ICDDP utilize only one simulation software package (Altair OptiStruct®) that provides the essential optimization and simulation methods. It is possible to integrate other software types into the ICDDP if they are necessary. In contrast, the result of one software application ensures that the interfaces

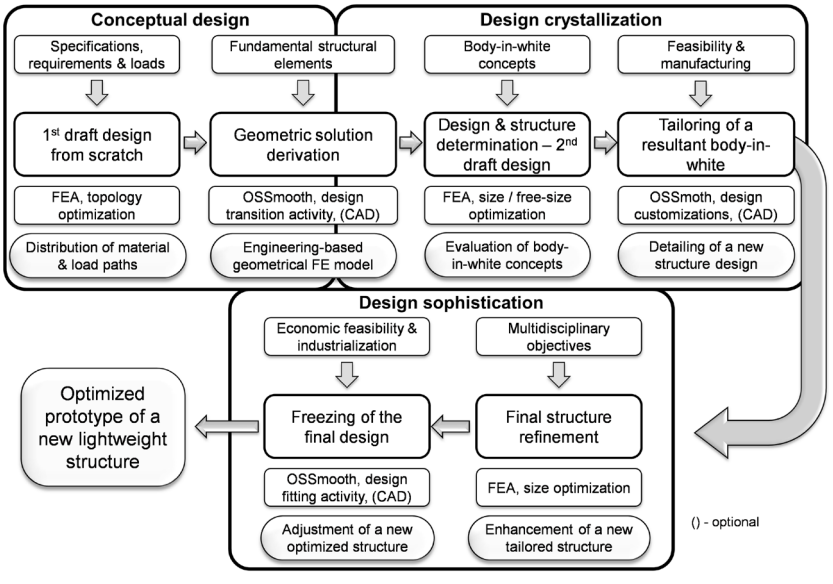

Fig. 3. *ICDDP – design principles and approaches throughout the steps and main development phases*

of the ICDDP remain the same in each step of the ICDDP. Furthermore, for the simulation software, neither additional knowledge nor special user training is required.

The main steps and design phases of the ICDDP are universal and to perform them, the other software types that make essential simulation and optimization methods available (either partially or all within one software environment) can also be applied. The ICDDP reduces the iterative design actions of a product's development such as design and calculation loops that are continuously repeated during the execution of the classic approach to product development. This removal of the recursive design actions decreases the duration of the development cycles considerably. The reduction in the development time depends on the complexity and technological advancement of a new product. Smaller reductions are expected for a single part design compared to greater reductions for the full vehicle development, which involves the design of many different modules and parts.

The ICDDP demonstrates the advantages of the conceptual design and design crystallization phases where the direct design from scratch delivers the new functional design proposals without iterative and time-consuming improvements in old designs. The ICDDP helps develop mechanical structures with different levels of complexity, i.e. body-in-white, brackets, hinges and crash boxes. More importantly, compared to the classic design approach, the ICDDP, with its more effective lightweight design (Fig. 18, section 3.2.3), provides new structures that meet specific sets of different requirements.

Altair® company provided an arrangement of optimization steps for the CDDP **[25]**, which utilizes the same simulation OptiStruct® software and divides the design process into three major steps: conceptual design, embodiment design, and detail structure design. Additionally, the authors of this paper have already published the backgrounds for the ICDDP with the optimization technology before **[26]** to **[28]**. Because of the same calculation and optimization software, analogous similarities are possible in the arrangement of the design process between these two concepts.

We tested the conceptual design phase of the ICDDP by utilizing the TO for a new all-terrain L7e class vehicle (ATV) structure. In consequence, this application raised the following questions:

- How should the TO be performed to produce the universal and optimal material distribution for the embodiment design?
- Is it possible to generalize the TO results from one material type to another?
- Is it possible to use the intensity of material distribution from the TO of isotropic material for the composite material application in the embodiment design phase?
- How can the results of the TO be interpreted for the first draft design of a new structure?
- Do the crash loads influence the form and geometry of the TO results?

The following sections provide the answers to the present questions.

2 CONCEPTUAL DESIGN PHASE OF THE ICDDP

The ICDDP allows for innovative solutions in the early design stage. The conceptual design is the first phase of the ICDDP and utilizes the TO to establish a rough design. This rough design is far from perfection, but bionic shapes of the TO results contain useful pieces of information about material intensity and distribution. The TO application must follow an efficient and reliable methodology that takes advantage of solutions arrived at and reveals as many design suggestions as possible.

Fig. 4 shows the organization of the two next sections of this paper that display the efficient and reliable methodology for the TO as well as the TO results.

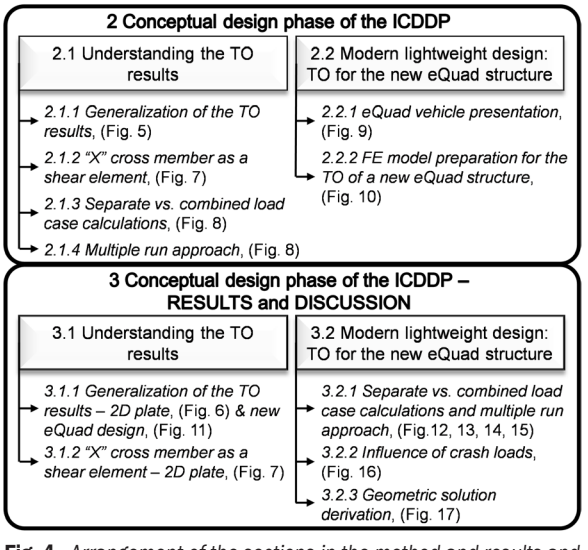

Fig. 4. *Arrangement of the sections in the method and results and discussion*

This organization helps indicate the advantages of the first ICDDP design phase and the resulting design of the new eQuad structure. Section 2 reveals

the applied methodology, whereas Section 3 details the simulation results for the examples and real use case from Section 2.

2.1 Understanding the TO Results

Engineers and designers actively search for the application of different materials that enable them to design lightweight structures. To take advantage of new design proposals provided by the TO, engineers need to understand the pieces of information and new design proposals that the TO delivers. This section demonstrates the methodology of the TO and enables better understanding of the TO results.

2.1.1 Generalization of the TO Results

The studies of many different material types can result in additional product development costs. For this reason, the authors of this paper considered the generalization of the TO results that employs the results of one material to prepare the design for the structure of another material. This idea also exploited the structure compliance (or weighted compliance) [16], [29], and [30], which was the function to minimize throughout this paper. If the generalization of the TO results works properly, it can significantly reduce the amount of working time during the early design stage and provide a great design.

The authors of this paper investigated the generalization by applying the TO to a thin plate made of five different material types: steel, titanium, aluminum, quasi-isotropic carbon fiber reinforced plastic and orthotropic CFRP. Table 1 reports the material properties selected for the FE models of the TO and shows the values for the single woven and uni-directional ply of CFRP material, respectively [31] and [32].

Table 1. *TO of the thin plate – material properties and resultant Y displacements*

Material	ρ [kg/mm³]	E [GPa]	υ [-]	Y displ [mm]
Steel	7.85e-06	210.0	0.30	-0.122
Titanium	4.40e-06	115.0	0.33	-0.222
Aluminum	2.70e-06	70.0	0.33	-0.366
Q-I CFRP	1.60e-06	78.0 / 78.0	0.06 / 6.5	-0.410
C-P CFRP	1.60e-06	126.0 / 11.0	0.28 / 6.6	-0.410
Q-I – quasi-isotropic laminate, C-P – cross-ply laminate				

We utilized the HyperLaminate® software from Altair® to prepare the quasi-isotropic and cross-ply CFRP laminates. Fig. 5a depicts the thin plate under the constant load F; the total amount was 1 kN, and the principal dimensions: length and width were 3a and a, where a is 150 mm, respectively. The volume (mass) during the TO runs of the generalization was constrained at 30 % of the initial value. Additionally, the option HOMO was applied for the DTPL card to consider the homogenized material properties [29] and [30] of defined laminates during the TO runs.

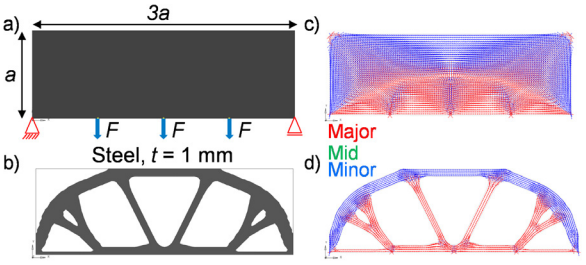

Fig. 5. *Generalization of the TO results: a) FE model, b) results for steel (t = 1 mm), c) original shape tensor plot (stress), d) optimized shape tensor plot (stress)*

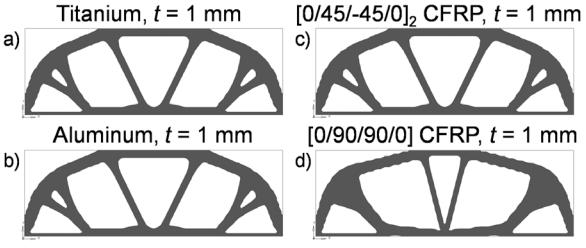

Fig. 6. *Results of the plate's TO: a) titanium, b) aluminum, c) quasi-isotropic CFRP, d) cross-ply CFRP*

2.1.2 "X" Cross Member as a Shear Element

The TO frequently produces bionic shapes in which the elementary geometric forms, such as rods and plates, dominate. These fundamental geometric elements often form "X" cross-members. These members can be thicker or thinner (Fig. 7c to d) depending on the real case in the local material distribution, but the main geometric shapes remain easy to recognize. The current paper's authors examined the formulation of the "X" cross-members as an effect of the local presence of shear loads. For this purpose, the authors studied the thin rectangular plate (Fig. 7a) with the length a = 100 mm and thickness t made of steel (material properties are listed in Table 1) under the constant shear load F, where the total amount was 1 kN. The volume fraction VF was limited to two different levels: 0.45 and 0.10.

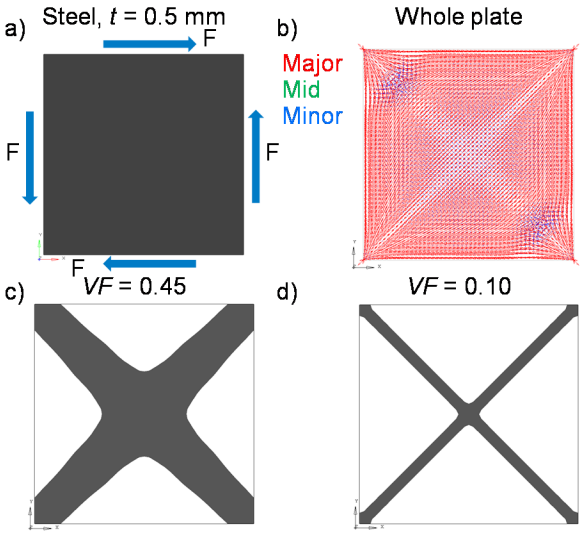

Fig. 7. *TO of the shear plate: a) FE model for steel, t = 0.5 mm, b) original shape tensor plot (stress), c) "X" shape results at VF = 0.45, d) "X" shape results at VF = 0.10*

2.1.3 Separate vs Combined Load Case Calculations

For mixed load scenarios, the TO results usually exhibit complex bionic shapes that intensify the difficulty to perform the design crystallization phase. Therefore, the authors of this paper performed an assessment of load case influences for separate and combined load cases. This assessment was based on the observation that a single separate load case reveals the bionic shapes more precisely. Instead, the combined load cases, which is a combination of single separate loads, can reduce and obscure the material and load path distributions due to a resultant character of combined loads. Consequently, a result interpretation is highly complicated for the combined load cases.

Fig. 8a demonstrates a proposal for the assessment of load case influences.

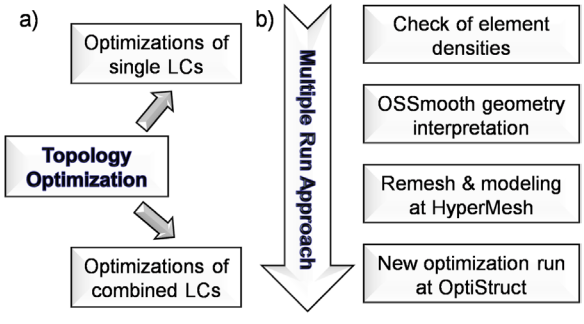

Fig. 8. *Methodology of the TO: a) assessment of load case influences, b) multiple run approach*

The method splits the TO process into the single and combined optimization runs. In this way, the bionic geometric shapes which delivered the TO for single and combined loads have an explanation for their presence. This explanation noticeably improves the interpretation of the TO results.

2.1.4 Multiple Run Approach

The TO results can demonstrate indistinctive character for a large and complex application (i.e. vehicle body structures), making the precise derivation of geometric solutions impossible. For this reason, the present paper's authors investigated a multiple run of the TO. The multiple TO run originated from Norberg and Lövgren's concept **[33]** and proposed running the TO for a given set of loads multiple times.

In contrast to Norberg and Lövgren's idea, we suggested that the multiple runs of the TO be performed with no additional control of the structure compliance. Instead, we performed the TO with a soft constraint on a resultant displacement, which is characteristic of the given set of loads. This soft constraint was not implemented into an FE TO model and can be based on user knowledge and experience, offering engineers the option of selecting the values of constraints arbitrarily. Fig. 8b demonstrates the idea of the multiple run approach. The method starts with the analysis of element density plots from the previous optimization run. The geometry interpretation is performed after the control of element densities. The OSSmooth® software within the HyperMesh® environment delivers new geometry for a specific density threshold. The meshing process is realized in HyperMesh® and the new model generated has the same boundary conditions as the starting model. The new OptiStruct® optimization run closes the loop of the multiple run approach. This loop can be repeated as many times as required. The main advantage of this method is to keep the amount of calculation time to acceptable levels. Applying this multiple run approach, the need for power and time computation increment gradually. If the method is applied, the load paths of new structures contrast more precisely.

Both present methodologies (assessment of load case influences and multiple run approach) can be applied either together for the TO, which was tested in this work, or separately, depending on the requirements.

2.2 Modern Lightweight Design: TO for the New eQuad Structure

The ICDDP enables engineers to develop a modern lightweight structure that satisfies specific sets of technical requirements. The paper's authors carried out the conceptual design phase of the ICDDP for a new eQuad structure by applying the TO. The main objective was to obtain the distribution of material and densities as well as load paths through the available three-dimensional (3D) design space.

2.2.1 eQuad Vehicle Presentation

The eQuad is an alternative, powered quadricycle, which the VIRTUAL VEHICLE Research Center adopted and further developed into a full electric specification. The lithium-ion batteries provide the electric energy to the electric engine [34]. The research center modified the original structure of the eQuad tubular space frame (Fig. 9b) by utilizing the conversion design approach because of the packaging purpose of electric powertrain components.

The vehicle is classified as an L7e vehicle [35]. The maximal speed is 45 km/h, and it can travel 30 km. The maximal permissible laden weight is 550 kg, which includes two occupants and some luggage; the mass of the vehicle tubular space frame is 82 kg.

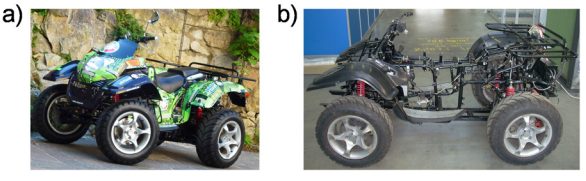

Fig. 9. *Fully electric vehicle – eQuad: a) complete vehicle, b) tubular space frame*

2.2.2 FE Model Preparation for the TO of the New eQuad Structure

Following the recommendation from [36], we defined the 13 different load scenarios for this work. These loads consider the various conditions: static, driving and crash situations. The load cases contain the forces for: vertical bending, front and rear torsion, front and rear braking, cornering, front and rear vertical bumps, bending for front and rear axles, and equivalent static front, rear and side crashes.

The estimation of the forces and load cases based on an approach of first-order models [37]. This approach enables engineers to execute instant analyses for what-if questions during the early design phase. We developed the additional equations for the first-order models that define the forces for the short-long-arm suspension type under driving conditions.

Table 2. *Load cases for the TO of the eQuad structure*

Load case	Calculation method	Dynamic coefficient
Bending	FEM	-
Torsion front	FEM	-
Torsion rear	FEM	-
Braking	1st OM (*)	Y
Braking into rear	1st OM (*)	Y
Cornering	1st OM (*)	Y
Vertical bump front	1st OM	Y
Vertical bump rear	1st OM	Y
Bending front axle	1st OM	Y
Bending rear axle	1st OM	Y
Static crash front	1st OM / WE	-
Static crash rear	1st OM / WE	-
Static crash side	1st OM / WE	-

1st OM – first-order model; WE – work-energy balance; Y – yes; (*) – new additional equations were developed

The calculative forces of driving conditions considered the dynamic behavior (Table 2) with the additional coefficients [37]. The final values were then applied to the attached points of the vehicle suspension. The authors of this work employed a work-energy balance approach [37] that determines the acting forces for the equivalent static crash loads. Additionally, we calculated the forces for the bending and torsion load cases [38] by performing the FE analyses for the current tubular space-frame. Furthermore, to assess the behavior of the vehicle during the accidents [38], we performed the virtual crash simulations on the complete FE eQuad model.

The FE model preparation for the TO contained a domain definition that allows the load paths to be generated using 3D FE mesh. This volume was limited by the available space for a new structure as well as by the vehicle equipment, which is attached to the vehicle structure.

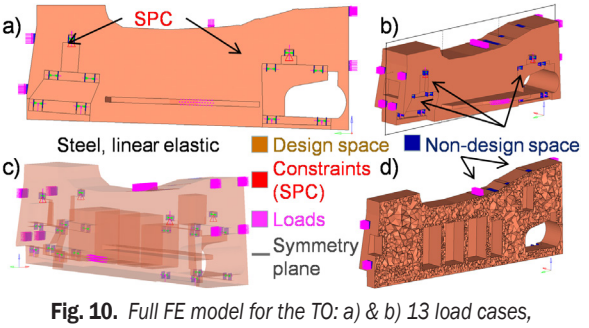

Fig. 10. *Full FE model for the TO: a) & b) 13 load cases, c) transparent view, d) cross-sectional view*

Therefore, the holes, cut-outs and geometric parts characterized the non-design space of the FE model that Fig. 10 exemplifies. Fig. 10 also presents the loads (forces) and constraints for the 13 load cases. The material model MAT1 was applied for the description of linear, temperature-independent, isotropic material properties that models the optimization domain, which was made of steel.

We employed an inertia relief approach that serves to increase optimization convergence and improve simulation stability in the case of unconstrained structures [29]. In addition, this FE model incorporated the minimum member size and longitudinal one plane symmetry that helps to regroup the elements in bigger accumulations and offers the option of obtaining symmetric material distribution even if the applied loads are asymmetric [29]. Fig. 10b illustrates the longitudinal one plane symmetry option, which is depicted as a transparent longitudinal plane. This plane also provides the cross-section view of the FE model. The FE mesh consisted of the 3D tetra linear finite elements that can model complex geometric shapes.

The total initial mass of the FE model (Fig. 10) was 2111.9 kg for the first optimization run of each load case. The authors assumed that the maximal displacements of the optimized structure should not exceed the resultant value of 2 mm (in special cases, 3 mm) for the selected load cases. The levels of volume fraction were set up for each load case (single or combined) to achieve the values of the established displacements. For the bending on the front and rear axles, the level of the volume fraction was adopted to the mean value of the other TO runs because of the larger displacements that provoked these load cases.

The limits on the maximum stresses were inconvenient to apply due to numerical obstacles that result from the change in the densities and Young's modulus for each finite element during the TO. Instead, the compliance minimization offers repeatable and stable distribution of the load paths.

3 CONCEPTUAL DESIGN PHASE – RESULTS AND DISCUSSION

The calculation results presented in this section correspond to the information about the methodology and models from the previous section. Additionally, the results are accompanied by comments. Furthermore, the quick FE reanalysis of a derivative geometric solution is illustrated at the end of this section.

3.1 Understanding the TO Results

We examined the methodology of the TO by performing the calculation for the basic examples presented in the previous sections as well as for the real use case (eQuad).

3.1.1 Generalization of the TO Results – 2D Plate & New eQuad Design

Fig. 5 and 6 exhibit the generalization of the TO results. In addition, Table 1 reports on the maximal displacements that result in the TO. The results of five different material types demonstrate the same geometric contour. Only the geometry of the cross-ply laminate reveals a slightly different shape, but it follows the main lines of the common form. More importantly, the orientation of the stress tensor depicts the geometric contour of the common form. This observation affirms that the TO highlights the load path distributions. In other words, the load path distribution illustrates the lines of force flows in the whole structure that connect the points of force applications with the support areas.

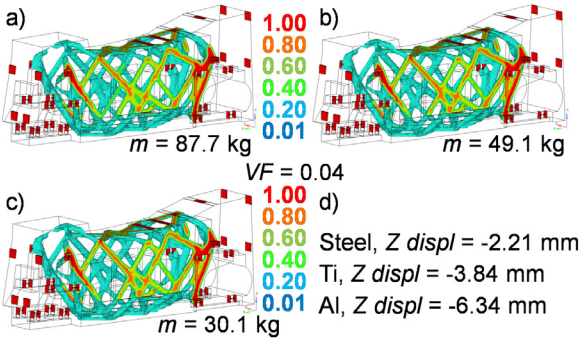

Fig. 11. *TO for the vertical bump rear load: a) steel, b) titanium, c) aluminum, d) Z displacements*

The paper's authors also examined the generalization of the TO results for a real use case that contains the 3D mesh. The TO is now available for composite material types; however, it is inconvenient for 3D volume mesh due to the orientation of material principle axes, which define the properties of orthotropic material during optimization runs. The search for the optimal orientation of material principle axes aggravates the optimization process notably. On the other hand, the generalization of the TO results overcomes this obstacle successfully. For this reason, the authors also investigated the generalization of the TO results for the 3D mesh of the real use case. Fig. 11 presents the element densities and material

distribution as well as the geometric shapes for three different material types: steel, titanium and aluminum. The minor changes in the geometric shapes result for the steel structure. The titanium and aluminum structures approximate the same geometric contour. Consequently, these facts proved the generalization of the TO results.

3.1.2 "X" Cross Member as a Shear Element – 2D Plate

Fig. 7 demonstrates the investigation of the "X" cross member formation. Changing the level of the volume fraction, the TO generally forms the same shapes as "X" cross members, in which the tensor plot of original geometry (Fig. 7b) is recognizable. Compared to this case, the real case discloses any fully detailed piece of information that characterizes the acting loads (due to the combined load cases, which provoke the complicated stress states) at the fragment of the structure. Therefore, the "X" cross members can be recognized as the element that the shear field provokes. In consequence, the translation of the "X" cross members into the "X" shape of rods or thin plates depends on the designers' interpretations.

3.2 Modern Lightweight Design: TO for a New eQuad Structure

The TO results for a new eQuad structure illustrate the methodology highlighted in the previous sections. This methodology was applied to reveal the advantages of the first ICDDP design phase for the real use case.

3.2.1 Separate vs. Combined Load Case Calculations and Multiple Run Approach

We investigated the assessment of load case influences and the multiple run approach in the real use case by performing the TO for the 13 separate load cases. We applied the multiple run approach twice.

Table 3 makes evident the mass values at the end of each optimization run as well as the maximum displacements at the end of the second run. Owing to the limited space of this work, Figs. 12 and 13 present only the two single load cases: bending and static crash rear. The assessment of load case influences demonstrated the significance of each single load case more accurately.

Considering single load case separately, the behavior of applied loads is easier to capture. Consequently, the material distribution generates the clearer load paths that display the necessary members of a new structure. These pieces of information facilitate the phase of the geometric solution derivation.

Table 3. *TO for the single load cases*

Load case	ml [kg]	mll [kg]	Max of displ [mm]
Bending	66.6	17.1	Z / -1.365
Torsion front	66.6	29.7	Z / 1.072
Torsion rear	71.8	38.6	Z / 1.038
Braking	66.6	29.2	Y / 1.540
Braking into rear	66.6	27.3	Y / -1.747
Cornering	66.6	26.7	X / -1.223
Vertical bump front	87.7	51.1	Z / -1.823
Vertical bump rear	119.3	75.4	Z / -1.549
Bending front axle	66.6	32.1	Z / 14.12
Bending rear axle	66.6	36.7	Z / 20.52
Static crash front	66.6	25.9	Y / -1.853
Static crash rear	66.6	22.7	Y / 1.823
Static crash side	66.6	49.6	Y / 1.866
ml, mll – mass after 1st and 2nd TO runs, respectively;			

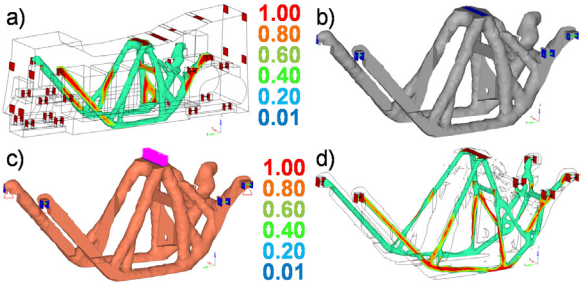

Fig. 12. *TO results of the bending: a) element densities at 1st run, b) geometry extraction of FE model at 2nd run, c) OSSmooth geometry at 2nd run, d) element densities at 2nd run*

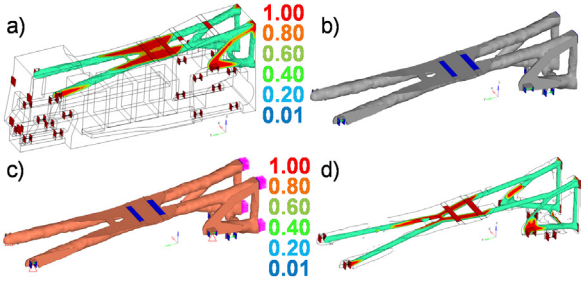

Fig. 13. *TO results of the static crash rear: a) element densities at 1st run, b) geometry extraction of FE model at 2nd run, c) OSSmooth geometry at 2nd run, d) element densities at 2nd run*

Figs. 12 and 13 exemplify the benefits of the multiple run approach. The dominance of intermediate values is pointed out in the element density plots of the first runs (Figs. 12a and 13a). The element density plots should intentionally present a contrast picture with the values of element density close to 1 for the major elements. The thickness of the single

structural members in the second TO run decreased, leading to the elements of the greater density level becoming more noticeable (Figs. 12d and 13d). Even though the second TO run reduced the remaining mass significantly, where the reduction was more than 70 % in some cases (Table 3), the stiffer elements (density near 1) were difficult to notice due to the allocation of such elements on the center lines of the geometric shapes.

More importantly, Figs. 14 and 15 affirm that the multiple run approach works properly for the combined load case by reducing the overall structural weight. Compared to the TO run of the single load cases, the paper's authors applied the TO to the combined load case three times.

Table 4. *TO for the combined load case*

Load case	ml [kg]	mll [kg]	mlll [kg]	Max of displ [mm]
CLC	214	150.6	94	Z8= -2.897 / Y12= 1.312

CLC – combined load case; ml, mll, mlll – mass after 1st, 2nd and 3rd optimization runs, respectively; Z8 – Z displacement for vertical bump rear case; Y12 – Y displacement for static crash rear case;

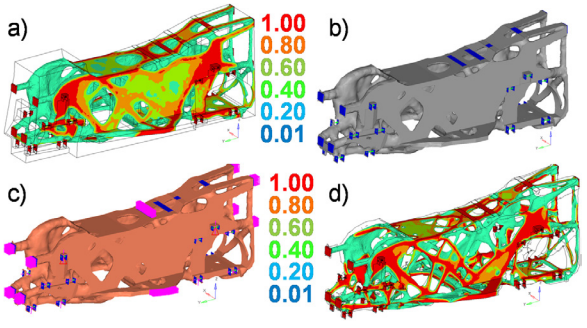

Fig. 14. *TO results of the combined loads case: a) 1st run, b) geometry extraction, c) 2nd run, d) 2nd run*

The material distributions became more discrete passing from one optimization run to the other. Additionally, Figs. 14 and 15 illustrate the areas that correspond to some plate-like shapes. The surface of such areas decreased with the steps of the multiple run method. Similarly, the element densities contrasted the dominance of higher values (Fig. 14d and 15d) that were close for the most part to 1.0.

The results of the multiple run approach revealed the distributions of the material and load paths that indicate fundamental geometric shapes of a new structure (Fig. 15d). The elements of the great density levels (near 1) highlighted the zones that actually require the material. Such polarized distributions allow for the geometric solution derivation. In addition, Table 4 illustrates the mass levels at the end of each TO run and the resultant displacement of the third run for the vertical bump rear load, which was used as the soft constraint throughout these three runs.

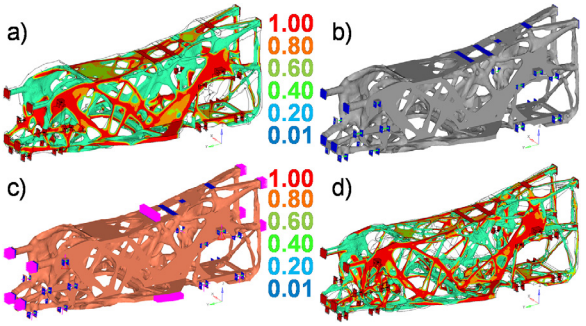

Fig. 15. *TO results of the combined loads case: a) 2nd run, b) geometry extraction, c) 3rd run, d) 3rd run*

The resultant displacement of the static crash rear loads is smaller due to the more complete outline of a new structure. Although the multiple run approach influenced the significant mass reduction, the end mass value of 94 kg is more than the mass of 82 kg for the original tubular space frame (Fig. 9b). The additional requirements for a new structure, i.e. crashworthiness, prompted the addition of weight to the TO results. For this reason, the paper's authors investigated the influence of the crash loads over the resultant geometry of a new structure.

3.2.2 *Influence of Crash Loads*

We carried out the TO runs, which included the application of the multiple run approach three times, to display the effect of crash loads on a new structure. The investigative load case consisted of all combined load cases without the crash loads. Fig. 16 demonstrates that the geometric shapes differ markedly for each step of the multiple run approach, compared with the results in Figs. 14 and 15.

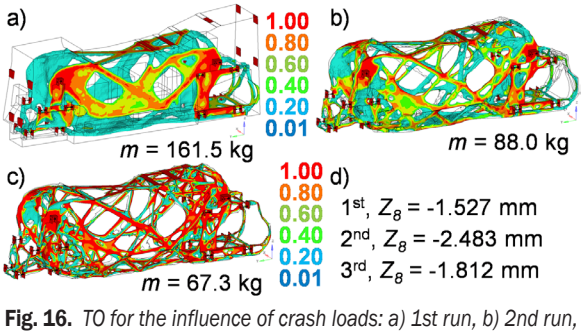

Fig. 16. *TO for the influence of crash loads: a) 1st run, b) 2nd run, c) 3rd run, d) Z displacements*

The lack of geometric shapes, which are characteristic for the crash loads, is exhibited in the front, lower central and rear parts of a new structure. Consequently, the mass levels in each of the TO runs were considerably lower than they were in the case of all combined loads.

3.2.3 Geometric Solution Derivation

We conducted the geometric solution derivation to express the fundamental manufacturable geometry from the TO results. We assumed that the distribution of material and load paths together with the knowledge of applied loads define the characteristics of acting loads, thus resulting in the bionic shapes of a new geometry.

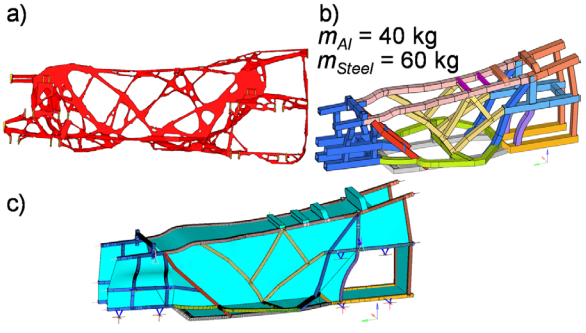

Fig. 17. *Geometric solution derivation: a) bionic OOSmooth geometry, b) CAD / FEM model interpretation, c) FE model for design crystallization*

Table 5. *FEA for the 1D beam model – maximum of the resultant displacements*

Load case	Aluminum, [mm]	Steel, [mm]
Bending	Z / -1.234	Z / -0.700
Torsion front	Z / 1.428	Z / 0.813
Torsion rear	Z / 1.703	Z / 0.977
Braking	Y / 0.644	Y / 0.378
Braking into rear	Y / -0.959	Y / -0.564
Cornering	X / -3.476	X / -6.082
Vertical bump front	Z / -2.826	Z / -1.617
Vertical bump rear	Z / -3.852	Z / -2.231
Bending front axle	Z / 9.287	Z / 5.458
Bending rear axle	Z / 51.350	Z / 29.490
Static crash front	Y / -1.000	Y / -0.594
Static crash rear	Y / 1.150	Y / 0.691
Static crash side	Y / 15.130	Y / 8.698
Wall thickness of rectangular cross-sections: steel – 2 mm, aluminum – 4 mm; Various dimensions of rectangular cross-sections for selected profiles		

The geometric solution derivation is based on the rod-like and plate-like geometric elements that form the bionic shapes of a new structure. Fig. 17 illustrates the geometry interpretation in the OSSmooth® software (Fig. 17a) as well as the rough design of a new structure – space frame (Fig. 17b).

We achieved the final design in CAD software by following the main lines of the load paths and using the industrial rectangular hollow profiles [39] and [40]. These profiles of the cross-sections had four different dimensions: 25 mm × 25 mm, 35 mm × 35 mm, 40 mm × 40 and 50 mm × 50 mm for both steel and material types.

The goal of the quasi-static FEA was to establish how much lightweight potential the first rough design of a new structure has. For this reason, we conducted the FEA for all 13 load cases and two material types: steel and aluminum. Table 5 shows the FEA results for the 1D FE model. The displacements calculated are comparable to or lower (Tables 3 and 5) than the rough results from the TO runs and affirm the conceptual design phase. Consequently, the derived simple space-frame has great lightweight potential.

As a summary of the ICDDP's design advantages, Fig. 18 affirms the great mass reductions while applying the ICDDP to the new structure design.

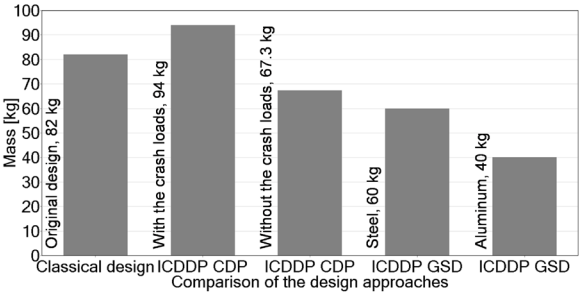

Fig. 18. *Comparison of the design approaches*

Compared to the design approach (original design), the conceptual design phase of the ICDDP (Fig. 18, ICDDP CDP) delivers significantly lighter solutions (in the case without the crash loads). The original design of the eQuad structure neglected the crash loads, whereas the new design of the eQuad structure, which also considers the crash loads, results from the first phase of the ICDDP with a higher mass (94 kg) than the original design (82 kg); yet, the geometric solution derivation step asserts that the first phase of the ICDDP provides the valuable design suggestions with its notable lightweight design (Fig. 18, ICDDP GSD for steel 60 kg and aluminum 40 kg). The ICDDP produces the efficient design concepts that meet the given sets of different requirements, including the crash loads.

4 CONCLUSIONS

Over the past decade, the mechanical engineering industry has been searching for an approach to the design process that integrates CAE tools and helps to develop innovative and competitive products. For this reason, we established the ICDDP as the design process that is driven by the optimization technology. Our definition of the ICDDP offers the stable and repeatable framework for engineers and designers that can create a new product in the various divisions of the mechanical engineering sector. More importantly, our description of the ICDDP ensures reductions in working time, user-friendly orientation and efficient resource management.

Consequently, we tested the conceptual design phase of the ICCDP for a real use case – a new eQuad structure. Since a body structure is fundamental to vehicle integrity, a new structure needs an accurate, innovative and lightweight design. On account of the fact that the new conceptual structure of the eQuad reveals these design properties, the conceptual design phase of the ICDDP fulfills the promises of a suitable, reliable and innovative tool.

Once the rough lightweight design of the new structure is obtained, this structure requires that additional design crystallization (the second phase of the ICDDP) take full advantage of weight reduction. The discussion of body-in-white structure types is a fundamental step for this phase. Such a discussion explores the 1D & 2D FE model (Fig. 17c), which is the improvement to the FE model from the geometric solution derivation step.

The design crystallization phase is under intensive ongoing scientific investigation that integrates the fundamental elements of a vehicle body design and different material types such as composites and sandwich composites. The first results of the design crystallization phase suggest utilizing these simple FE models for further design and structure determination.

5 ACKNOWLEDGEMENTS

This work was accomplished at the VIRTUAL VEHICLE Research Center in Graz, Austria. The authors would like to acknowledge the financial support of the COMET K2 - Competence Centers for Excellent Technologies Program of the Austrian Federal Ministry for Transport, Innovation and Technology (BMVIT), the Austrian Federal Ministry of Science, Research and Economy (BMWFW), the Austrian Research Promotion Agency (FFG), the Province of Styria and the Styrian Business Promotion Agency (SFG).

6 REFERENCES

[1] Sellgren, U. (1999). *Simulation-Driven Design - Motives, Means, and Opportunities*. PhD thesis. KTH, Stockholm.

[2] Sjödin, T. (2010). Optimization-driven design at Saab automobile AB. *ProOpt Workshop on Optimization Driven Design Proceedings*, Jönköping.

[3] Konzelmann, M., Krishnamoorthy, S., Chaudhari, S., Kopp, G., Friedrich, H.E. (2013). CAE-driven design methodology for semi-autonomous product development. *European Altair Technology Conference Proceedings*, Torino.

[4] Münster, M., Schäffer, M., Friedrich, H.E. (2015). Development of body structure concepts for electric vehicles using the topology optimization for global load pathfinding. *European Altair Technology Conference Proceedings*, Paris.

[5] Kramer, F. (1986). *Innovative Produktpolitik, Strategie – Planung – Entwicklung – Einführung*. Springer, Berlin, **DOI:10.1007/978-3-642-95504-4**. (in German)

[6] Vanja, S., Weber, C., Bley. H., Zeman, K., Hehenberger, P. (2009). *CAx für Ingenieure*. Springer, Berlin Heidelberg, **DOI:10.1007/978-3-540-36039-1**. (in German)

[7] Henkel, N., Treiber S. (2015). Cost-effective sizing of your HPC cluster for CAE simulations. *10th European LS-DYNA Conference Proceedings*, Würzburg.

[8] Gupta, S.K., Anand, D.K., Brough, J.E., Schwartz, M., Kavetsky, R.A. (2008). *Training in Virtual Environments. A Safe, Cost-Effective, and Engaging Approach to Training*. University of Maryland, Maryland.

[9] Leadley-Brown, M. (2011). Simulation driven design. *Deutsche SIMULIA-Konferenz Proceedings*, Bamberg.

[10] Von Dungern, O., Hoffmann, R. (2016). Using knowledge graphs for automotive safety requirements management. *9th Graz Symposium Virtuelles Fahrzeug Proceedings*, Graz.

[11] Kompas, K., Wang, L., Jung, O. (2016). Effectiveness assessment of future vehicle safety systems. *9th Graz Symposium Virtuelles Fahrzeug Proceedings*, Graz.

[12] Merklein, M., Geiger, M. (2002). New materials and production technologies for innovative lightweight constructions. *Journal of Materials Processing Technology*, vol. 125-126, p. 532-536, **DOI:10.1016/S0924-0136(02)00312-6**.

[13] Thomas, D., Block, H., Tröster, T. (2011). Production of load-adapted lightweight designs by partial hardening. *3rd International Conference on Steel in Cars and Trucks Proceedings*.

[14] Iljaž, J., Škerget, L., Štrakl, M., Marn, J., (2016). Optimization of SAE formula rear wing. *Strojniški vestnik - Journal of Mechanical Engineering*, vol. 62, no. 5, p. 263-272, **DOI:10.5545/sv-jme.2016.3240**.

[15] Cesnik, M., Slavic, J., Boltežar, M., (2016). Assessment of the fatigue parameters from random vibration testing: application to a rivet joint. *Strojniški vestnik - Journal of Mechanical Engineering*, vol. 62, no. 7-8, p. 471-482, **DOI:10.5545/sv-jme.2016.3774**.

[16] Harzheim, L. (2014). *Strukturoptimierung: Grundlagen und Anwendungen. 2 Auflage*. Europa-Lehrmittel, Haan-Gruiten. (in German)

[17] Hirz, M., Dietrich, W., Gfrerrer, A., Lang, J. (2013). *Integrated Computer-Aided Design in Automotive Development*. Springer-Verlag, Berlin-Heidelberg, **DOI:10.1007/978-3-642-11940-8**.

[18] Stanton, M. (2015). Exceeding customer expectations by left shifting with robust virtual engineering at jaguar land rover. *European Altair Technology Conference Proceedings*, Paris.

[19] Kang, B. (2015). CAE for digital development. *European Altair Technology Conference Proceedings*, Paris.

[20] The Association of German Engineers (VDI) (1997). *VDI 2221: Methodik zum Entwickeln und Konstruieren technischer Systeme und Produkte*. Verein Deutscher Ingenieure, Düsseldorf. (in German)

[21] The Association of German Engineers (VDI) (1997). *VDI 2222: Blatt 1 Methodisches Entwickeln von Lösungsprinzipien*. Verein Deutscher Ingenieure, Düsseldorf. (in German)

[22] The Association of German Engineers (VDI) (1997). *VDI 2223: Blatt 1 Methodisches Gestalten*. Verein Deutscher Ingenieure, Düsseldorf. (in German)

[23] Ehrlenspiel, K. (2003). *Integrierte Produktentwicklung. 2. Auflage.* Hanser, München. (in German)

[24] Warnecke, U., Rosenplaenter, S. (2016). The Journey to MBSE and PLM. *9th Graz Symposium Virtuelles Fahrzeug Proceedings*, Graz.

[25] C123. Altair Engineering, Inc, *from http://www.altair.com/newsdetail.aspx?news_id=11283*, accessed on 2016-11-10.

[26] Jedrzejczyk, R.P., Alb, M., Jost, T. (2015). Optimierung als wesentlicher Punkt in der Leichtbau-Konzeptentwicklung. *4a Technologietage 2015 Proceedings*, Schladming.

[27] Jedrzejczyk, R.P., Alb, M., Jost, T. (2015). Conceptual studies of the lightweight vehicle structure for the L7e vehicle class by the use of optimization process at OptiStruct environment. *European Altair Technology Conference Proceedings*, Paris.

[28] Jedrzejczyk, R.P., Alb, M., Jost, T. (2016). CAE-driven design process for modern lightweight structures. *9th Graz Symposium Virtuelles Fahrzeug Proceedings*, Graz.

[29] Altair Engineering Inc. (2015). *HyperWorks 14.0. OptiStruct Reference Guide*, Melbourne.

[30] Altair Engineering Inc. (2015). *HyperWorks 14.0. OptiStruct User's Guide*, Melbourne.

[31] Soden, P.D., Hinton, M.J., Kaddour, A.S. (1998). Lamina properties, lay-up configurations for a range of fibre-reinforced composite laminates. *Composites Science and Technology*, vol. 58, no. 7, p. 1011-1022, **DOI:10.1016/S0266-3538(98)00078-5**.

[32] Daniel, M.I., Ishai, O. (2006). *Engineering Mechanics of Composite Materials. 2nd Edition*. Oxford University Press, New York, Oxford.

[33] Norberg, E., Lövgren, S. (2011). *Topology Optimization of Vehicle Body Structure for Improved Ride & Handling*. MSc thesis. Linköping University, Linköping.

[34] eQuad. Virtual Vehicle Research Center, *from http://www.v2c2.at/en/research/ee-and-software/projects/equad/*, accessed on 2016-11-10.

[35] Edwards, M., Seidl, M., Carroll, J., Nathanson, A. (2014). *Provision of information and services to perform an initial assessment of additional functional safety and vehicle construction requirements for L7e-A heavy on-road quads.* Transport Research Laboratory. European Commission, Brussels.

[36] Krishnamoorthy, S.K., Beeh, E., Schöll, R., Friedrich, H.E. (2012). Methodik zur Karosserieentwicklung mittels Topologieoptimierung. *Tagung Faszination Karosserie und Fahrzeugkonzepte Proceedings*. Wolfsburg. (in German)

[37] Malen, D.E. (2011). Fundamentals of Automobile Body Structure Design. *SAE International*, Warrendale.

[38] Jedrzejczyk, R.P., Jost, T. (2015). The finite element assessment of structure properties for a L7e class vehicle under the bending, torsion static and crash loads. *ICoEV 2015 International Conference on Engineering Vibration Proceedings*, Ljubljana.

[39] Metric Rectangular Tube. Parker Steel Company, from *http://www.metricmetal.com/products/rec2395.htm*, accessed on 2016-11-10.

[40] Parker Steel Company. (2016). *Metric Size Metals. Metric Metals Reference Guide,* Toledo.

Strojniški vestnik - Journal of Mechanical Engineering 64(2018)1, 17-25

DOI:10.5545/sv-jme.2017.4671 Original Scientific Paper
Received for review: 2017-06-15
Received revised form: 2017-10-18
Accepted for publication: 2017-11-06

The Application of LCS and Information Entropy as a Novel Fusion Algorithm for Degradation Feature Extraction

Haotian Wang[1] – Jian Sun[2,*] – Xiusheng Duan[1] – Ganlin Shan[1] – Wen Yang[2]
[1] Mechanical Engineering College, China
[2] Luoyang Electronic Equipment Test Center of China, China

Feature extraction is significant for the prognostics and health management (PHM) of hydraulic pumps. In this paper, a novel fusion algorithm is proposed based on local characteristic-scale decomposition (LCD), composite spectrum (LCS). and information entropy. To make full use of feature information, the LCS is proposed based on the modification of traditional composite spectral algorithm. LCS high-order power entropy and high-order singular entropy, which are relatively defined in Shannon entropy (SE) and Tsallis entropy (TE), are extracted as initial features. Furthermore, the method of feature fusion is presented to modify the features' conciseness and to improve the performance. Results of the analysis in the experiment indicate that the proposed method is available, and the fused feature is effective in evaluating the pump degradation process.
Keywords: degradation feature extraction, information fusion, LCS, information entropy, hydraulic pump.

Highlights
- *A novel fusion algorithm based on LCS and information entropy for the degradation feature extraction of hydraulic pumps is proposed.*
- *The fusion method based on information entropy is proposed to make fusion of initial features.*
- *The LCS algorithm gains the ability to extract more sensitive features than usual algorithms and it is effective in evaluating the pump degradation process.*

0 INTRODUCTION

Conditional-based maintenance (CBM) is a modern maintenance concept [1]. As an effective method to realize CBM, prognostics and health management (PHM) has become the focus of the research [2]. One typical example is the application of PHM in joint strike fight (JSR) F-35 [3]. To establish the appropriate PHM of equipment, it is first necessary to conduct the research of degradation feature extraction for prognostics [4]. The degradation experiment requires a long time and the vibration signals during the degradation are very complex [5]. However, features extracted by traditional methods [6] are normally based on the single monitoring signal. Tran et al. extracted features by the analysis of the monitoring signal in the time domain [7]. Zhao used the empirical mode decomposition (EMD) in vibration signal analysis and extracted the approximate entropy as the degradation feature [8]. Dong et al. chose the non-extensive wavelet feature scale entropy to be the feature for degradation evaluation [9]. In this situation, some important fault information may be lost. For example, it is known that the loose slipper fault is the typical failure mode of hydraulic pumps [10]. It is caused by the wear between the head of the piston and the hat of the slipper [11]. Finally, the interaction could be monitored on the pump shell in the form of strikes. However, the strikes of the interaction are not always from only one direction [12]. Analysis based on a single vibration signal can hardly achieve the whole information needed for diagnosis and prognosis. As a result, multi-direction vibration signals are required for processing. Additionally, vibrations of hydraulic pumps caused by the striking from pistons are directly influenced by the coupling effect [13]. It seems to be extremely difficult to effectively extract obvious fault information. To solve this issue, a modified method is required to fuse multi-direction signals of the hydraulic pump to extract the degradation features more effectively.

The traditional fusion algorithms for multiple signals include the weighted fusion algorithm [14], the Kalman filtering algorithm [15] and the wavelet analysis fusion algorithm [16]. Based on the analysis of these methods [17], it is known that some important fault information may be lost due to the inherent disadvantages during signal processing [18]. As a novel fusion algorithm, composite spectrum (CS) can calculate the correlative relations between neighbouring signals for information fusion [19]. Considering the structural characters of hydraulic pumps, some modifications must be made to extract the sensitive features effectively [20]. First, the complex computation caused by the multiplication the CS algorithm must be reduced. On this basis,

*Corr. Author's Address: Luoyang Electronic Equipment Test Center of China, Luoyang 471003, China, hehetcs@163.com

an appropriate method is required for CS fusion to obtain detailed components from the original signals, which contain sensitive feature information. An LCD algorithm is an efficient nonlinear signal processing method [21]. The feature information in the original signal can be detailed into various intrinsic scale components (ISCs) [22]. The sensitive information is relatively easy to be achieved for CS fusion. Therefore, based upon the modification of the earlier CS, the LCD composite spectrum (LCS) algorithm is proposed for the fusion of various vibration signals to extract sensitive degradation features.

Features extracted by various methods can reveal fault information in different aspects to improve completeness. However, it may also increase information redundancy degree and even result in dimensional disaster [23]. Common methods to solve this problem include decreasing dimensions by simplifying signal features [24]. The typical algorithms are principal component analysis (PCA) and the locality-preserving projection (LPP). PCA performs better only with linear data. If the high-dimensional data needed processing is nonlinear, the PCA's ability for feature dimensionality reduction would be limited [25]. LPP is a widely used manifold learning algorithm. Based on the Laplace mapping, LPP can deal with the nonlinear data [26]. However, LPP always requires many samples [27]. Furthermore, these dimensionally reduction methods may delete parts of features directly, leading to the loss of sensitive information. As analysed, the basis for feature dimensionality reduction is to evaluate the correlations between various vectors [28]. Correlation coefficient is one traditional factor [29]. Because of the structural character of hydraulic pump, the data of the extracted feature are nonlinear to a large extent. In this situation, the correlation coefficient can hardly evaluate the correlations. Based on information entropy theory, the relative entropy can reveal the correlation between nonlinear data by the analysis of the complexity [30]. Therefore, the feature fusion algorithm is proposed to make full use of the extracted features' information and to improve features conciseness.

Consequently, the method for feature fusion using LCS and relative entropy is proposed. This article is organized as follows: In Section 0, the LCS algorithm is presented for multi-channel signal fusion; In Section 1, LCS high-order power entropy and the high-order singular entropy, which are relatively defined in SE and TE, are extracted as initial features; in Section 2, a feature fusion strategy based on relative entropy is put forward in detail and the originally extracted features are fused into the required new feature; in Section 3, the experiment is presented and the results are verified by the application of the proposed method; in Section 4, some conclusions are drawn.

1 THE PROPOSED LCS FUSION ALGORITHM

1.1 Signals Decomposed by LCD

Assuming that $x(t)$ denotes the original signal, the LCD algorithm is detailed as follows.

Step 1. Confirm the extremum point X_k of $x(t)$ and its correspondent time τ_k, $k=1,2,...,M$. M is the total number of all extremum points.

Step 2. Calculate A_{k+1} ($k=2,3,...,K-1$) and L_k:

$$A_{k+1} = X_k + \frac{\tau_{k+1}-\tau_k}{\tau_{k+2}-\tau_k}(X_{k+2}-X_k), \tag{1}$$

$$L_k = aA_k + (1-a)X_k, \quad k = 2,3,...,K-1. \tag{2}$$

Step 3. Fit $L_1 \sim L_k$ by the cubic spline function and acquire the baseline $BL_1(t)$. Separate the baseline.

$$h_1(t) = x(t) - BL_1(t), \tag{3}$$

if $h_1(t)$ meets the ISC condition [21], output $ISC_1 = h_1(t)$.

Step 4. Separate ISC_1 from the original data and get the new signal. Then repeat the steps until $u_n(t)$ is monotonous or a constant function. Get ISC_1, ISC_2, …, ISC_n and the trending component $u_n(t)$ $u_n(t)$.

1.2 Selection of ISCs

Normally, the correlation coefficient is applied for the reflection of the nonlinearity between variables, and the mutual information is used for the reflection of the linearity relations. In this paper, based on the SE, the mutual information I is defined:

$$\begin{cases} I(y_1,...,y_n) = \sum_{i=1}^{n} H(y_i) - H(y_1,...,y_n) \\ H(y_i) = -\int p(y_i)lgp(y_i)dy_i \end{cases}, \tag{4}$$

where, $H(y_i)$ is the entropy of y_i. $p(y_i)$ is the probability density function for p_i. For the solution of joint probability density function, the probability of the samples falling into multi-dimensional space can be used for approximate estimation.

In this paper, on the basis of the mutual information, the sensitive factor ε is defined as the ISCs selection index. Assume that the sampling parameters are the same, the sampled normal signal is y_{nor}, and the sampled fault signal is y_f. The fault

signal is further decomposed by LCD and the i^{th} ISC component is marked as ISC_i. The sensitive factor of ISC_i is ε_i, which is calculated by Eq. (5).

$$\varepsilon_i = I_{1i} - I_{2i}, \tag{5}$$

where, I_{1i} denotes the mutual information between ISC_i and y_f. I_{2i} denotes the mutual information between ISC_i and y_{nor}. Based upon the analysis above, ε_i can evaluate the sensitive information contained in ISC_i. The higher the ε_i is, the more obvious the difference between the mutual information I_{1i} and I_{1i} will be. This means that the sensitive fault information contained in the ISC_i is supposed to be more. Therefore, the ISC component with the highest ε_i will be selected from each vibration signal.

1.3 LCS Algorithm

Based on the n_s division of every ISC, the CS is defined as [19]:

$$S_{CS}(f_k) = \sum_{r=1}^{n_s} X_{CS}^{r}(f_k) X_{CS}^{r*}(f_k) / n_s, \tag{6}$$

where $X_{CS}^{r}(f_k)$ denotes the Fourier coefficient and $X_{CS}^{r*}(f_k)$ denotes its complex conjugate in the r^{th} segment in all B signals. $X_{CS}^{r}(f_k)$ is defined by Eq. (7).

$$X_{CS}^{r}(f_k) = \sqrt{(S_{x_1\gamma_{12}x_2}^{r}(f_k) S_{x_2\gamma_{23}x_3}^{r}(f_k) ... S_{x_{B-1}\gamma_{(B-1)B}x_B}^{r}(f_k))^{1/(B-1)}}, \tag{7}$$

where $\gamma_{12}, \gamma_{23}, ..., \gamma_{(B-1)B}$, denote the coherences. $S_{x_1\gamma_{12}x_2}^{r}(f_k), S_{x_2\gamma_{23}x_3}^{r}(f_k), ..., S_{x_{B-1}\gamma_{(B-1)B}x_B}^{r}(f_k)$ are defined by Eq. (8).

$$S_{x_1\gamma_{12}x_2}^{r}(f_k) = [X_1^{r}(f_k)\gamma_{12}X_2^{r*}(f_k)]. \tag{8}$$

The multiplication of the Fourier coefficient and the complex conjugate exists in CS. If Eq. (8) is combined with Eq. (7), terms like $X_2^{r*}(f_k)X_2^{r}(f_k), X_3^{r*}(f_k)X_3^{r}(f_k), ...$ are achieved, which can be merged together. This phenomenon leads to the increasing of the computation complexity. To solve this problem, Eq. (6) in LCS algorithm is redefined by Eq. (9).

$$S_{CS}(f_k) = (\sum_{r=1}^{n_s} X_1^{r}(f_k)\gamma_{12}^2 X_2^{r}(f_k)\gamma_{23}^2 X_3^{r}(f_k) ... \\ ... X_{B-1}^{r}(f_k)\gamma_{(B-1)B}^2 X_B^{r}(f_k))^{1/B} / n_s. \tag{9}$$

Compared with Eq. (1), the computation of LCS algorithm is only around half of the earlier CS algorithm. Furthermore, the high sensitivity information contained in the selected ISCs is introduced and further processed by LCS.

2 THE PROPOSED METHOD FOR DEGRADATION FEATURE EXTRACTION

2.1 Extraction of LCS high-Order Power Spectral Entropies

Information entropy is an effective factor to quantitatively reveal the uncertain information in the signal by putting up the contained characteristics. As indicated in our previous research in reference [31], the high order entropy is sensitive to non-symmetrical and nonlinear components and it could reveal the information which cannot be obtained by second-order statistical analysis. Therefore, the high-order entropy is used in this paper as the LCS spectrum analysis factor. It can describe the degradation trend. SE is a kind of information entropy that is defined in logarithmic form. For a system which contains Q microstates, the SE is defined by Eq. (10) [32].

$$SE = -Bolt \sum_{i=1}^{Q} p_i \ln(p_i), \tag{10}$$

where $Bolt$ is the Boltzmann constant, p_i means the occurrence probability of the i^{th} status. SE is usually used to reveal the property of the scope system and it can reflect the general trend. However, the factual system may be more or less correlated in time and space, and SE can hardly reveal all the inner characteristics of the system. Being the generalization of SE, TE is able to reveal the non-scope information which cannot be obtained by SE. TE is defined by Eq. (11) [32].

$$TE = -Bolt(1 - \sum_{i=1}^{Q} p_i^q) / (1-q), \tag{11}$$

where q is the non-scope parameter. The common settled value of q is 3. Compared with SE, the values of TE range only from 0 to 1. However, there may be the correlations in time and space or certain degradation stages. TE is required to be the supplement of SE. As a result, to reveal the performance degradation of hydraulic pumps effectively and sensitively, the Shannon LCS power spectral entropy (SLPE) and Tsallis LCS power spectral entropy (TLPE) are both selected to be the features.

Based on reference [31], taking the three-channel vibration signals as example, the procedures are detailed as follows.

① LCD is applied in each of the three vibration signals; after selection, three ISCs remained.

② Divide each ISC into N parts and then carry out Fourier transform on each part and obtain $X_i^j, i=1,2,3,\ j=1,...,N$.

③ Calculate the composite spectrum $S_{CF}(f_k)$:

$$S_{CS}(f_k)=(\sum_{j=1}^{N}X_1^j(f_k)\gamma_{12}^2X_2^j(f_k)\gamma_{23}^2X_3^j(f_k))^{1/3}/N. \quad (12)$$

④ Make standard procession on the obtained $S_{CF}(f_k)$ and the result is $\{u(t),\ t=1,2,\ldots,N\}$. Calculate the triple correlation of DCT coefficients.

$$b_i(\lambda_1,\lambda_2)=\frac{1}{\mu^2}\sum_{k_1=-s_1}^{s_1}\sum_{k_2=-s_2}^{s_2}Y^{(i)}(\lambda_1+k_1)Y^{(i)}...$$
$$...(\lambda_2+k_2)Y^{(i)}(\lambda_1+\lambda_2+k_1+k_2), \quad (13)$$

where $Y(i)$ is the DCT coefficient, $\mu=f_k/N$, s_1 and s_2 are the 3-order accumulation range, λ_1 and λ_2 are positive and the sum should not be more than half of the sampling frequency f_s.

⑤ Calculate the proportion of each coefficient:

$$p_k=|b_k(\lambda_1,\lambda_2)|^2/\sum_{l=1}^{N}|b_l(\lambda_1,\lambda_2)|^2, \quad (14)$$

where K means number of the frequency bands.

⑥ Calculate SLPE and TLPE:

$$SLPE=-Bolt(\sum_{k=1}^{K}p_k\ln p_k)/\ln K, \quad (15)$$

$$TLPE=-Bolt(1-\sum_{k=1}^{K}p_k^q)/(1-q). \quad (16)$$

Based on the analysis, it can be seen that LCS high-order power spectral entropies (SLPE and TLPE) are sensitive to the total energy changes theoretically.

2.2 Extraction of LCS High-Order Singular Spectral Entropies

As another effective spectrum parameter, singular spectral entropy is able to reveal complexity of signal components. Compared with power spectral entropy, it tends to be more sensitive to response energy changing [33]. The first four calculation steps of LCS high order singular entropy are the same as LCS high-order power spectral entropy, and the following steps are:

⑤ Calculate the DCT high order estimation matrix B.

$$B(\lambda_1,\lambda_2)=\sum_{i=1}^{N}b_i(\lambda_1,\lambda_2)/N. \quad (17)$$

⑥ Make singular values decomposition on U and calculate the proportion of each:

$$\mathrm{U}=\mathrm{EDW}, \quad (18)$$

where $\mathbf{E}$ is $V\times O$ matrix, $\mathbf{D}$ is $O\times O$ matrix and $\mathbf{D}=\mathrm{diag}(x_1,x_2,\ldots,x_O)$. $\mathbf{W}$ is $O\times T$ matrix, and O is the order of U.

$$p_u=x_u/\sum_{o=1}^{O}x_o. \quad (19)$$

⑦ Calculate LCS high-order singular entropies respectively defined in SE and TE, which is marked as *SLSE* and *TLSE*:

$$SLSE=-Bolt\sum_{u=1}^{O}p_u\ln p_u, \quad (20)$$

$$TLSE=-Bolt(1-\sum_{u=1}^{O}p_u^q)/(1-q). \quad (21)$$

LCS high-order singular entropies (SLSE and TLSE) are able to reveal distributions of various mode components in composite spectrum sensitively. If the degradation degree is lighter, distributions of different mode components are in balance and the signal complexity will be higher and, consequently, the entropies will be higher.

2.3 The Proposed Features Fusion Algorithm

The main purpose of features' fusion is to improve the completeness and conciseness. As a typical evaluating factor, the traditional definition for relative entropy is shown in Eq. (22) [34]:

$$I(y_1,...,y_n)=\sum_{i=1}^{n}H(y_i)-H(y_1,...,y_n), \quad (22)$$

where I represents for the relative entropy of vector $y_1,\ldots,y_n$, $H(y_i)$ is the SE of each vector.

Assume that the features data collection extracted from various degradation stages after normalization is $\mathbf{X}=[\mathbf{X}_1,...,\mathbf{X}_n,...,X_N]$, where N is the number of features. X_n is the vector of the n^{th} feature, and $\mathbf{X}_n=[s_1^n,...,s_m^n]^T$, where s_m^n is the n^{th} element of the m^{th} sample.

Step 1. For the extracted N features, calculate $I(\mathbf{X}_{n1},\mathbf{X}_{n2})$ between two arbitrary feature vectors:

$$I(\mathbf{X}_{n1},\mathbf{X}_{n2})=H(\mathbf{X}_{n1})+H(\mathbf{X}_{n2})-H(\mathbf{X}_{n1n2}), \quad (23)$$

where, $\mathbf{X}_{n1n2}$ is the new reconstructed feature by the fusion of $\mathbf{X}_{n1}$ and $\mathbf{X}_{n2}$. s_m^{n1n2} is the element of $\mathbf{X}_{n1n2}$, which is defined as:

$$s_m^{n1n2}=p_m^{n1}s_m^{n1}/(p_m^{n1}+p_m^{n2})+p_m^{n2}s_m^{n2}/(p_m^{n1}+p_m^{n2}). \quad (24)$$

Step 2. Choose $\mathbf{X}_{nx}$ and $\mathbf{X}_{ny}$ with the maximum I_{nxny} and delete these two feature vectors. Then add the new fused feature $\mathbf{X}_{nxny}$ into $\mathbf{X}$ instead. Then the dimension of $\mathbf{X}$ reduces to N–1.

Step 3. Repeat the steps above until dimension X becomes 2.

Step 4. Carry out the final fusion of the only two features in X. The final achieved feature is the fused one needed for use.

Based on the gradual fusion strategy, all extracted features are finally fused into only one new feature, effectively improving the concision of computation.

3 EXPERIMENTAL VALIDATION

3.1 Experimental Rig

To verify the proposed method, an experiment was conducted on the test-bed shown in Fig. 1. Three-channel vibration signals were sampled.

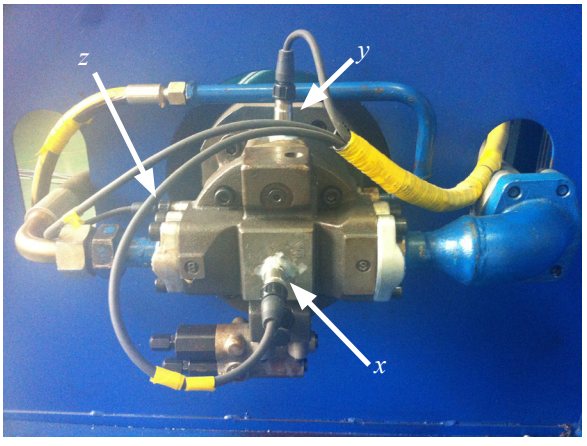

Fig. 1. *Installation of the vibration sensors*

According to the technical documentation from the pump manufacturer, the volumetric efficiency (VE) is applied to evaluate the degradation performance. When VE is less than 80 %, the pump is confirmed to be failed. In this experiment, VE was less than 80 % when the total time was 582 h 15 min 17 s. After disassembly, the piston was verified to occur the loose slipper failure, as seen in Fig. 2.

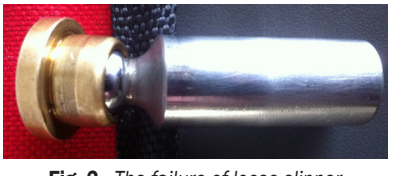

Fig. 2. *The failure of loose slipper*

3.2 Results and Analysis

The whole degradation processes are roughly divided, as shown in Table 1.

Table 1. *Various degradation stages*

VE	Operating time	Degradation state	Mark
95 % to 100 %	0 to 532 h 55 min 11 s	normal	
94 % to 95 %	532 h 55 min 12 s to 549 h 54 min 46 s	initial failure	F1
92.5 % to 94 %	549 h 54 min 47 s to 562 h 0 min 25 s	slow development	F2
90 % to 92.5 %	562 h 0 min 26 s to 572 h 49 min 33 s	weak failure	F3
85 % to 90 %	572 h 49 min 34 s to 579 h 26 min 52 s	accelerated degradation	F4
80 % to 85 %	579 h 26 min 53 s to 582 h 15 min 17 s	loose slipper formation	F5

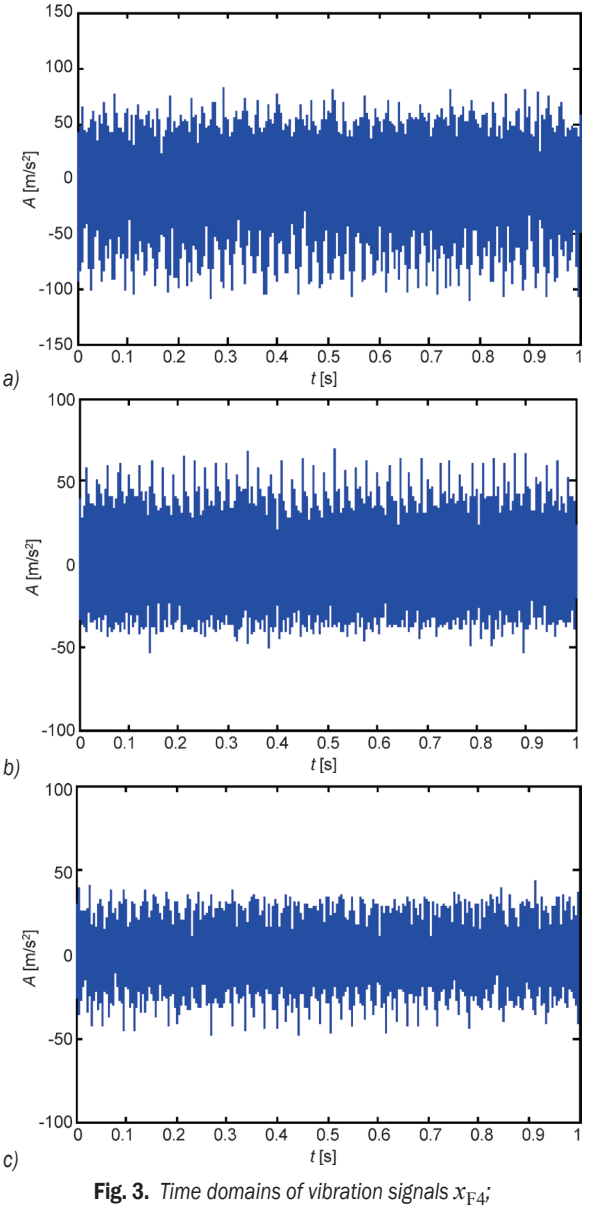

Fig. 3. *Time domains of vibration signals* x_{F4}*; a)* $x_{F4\text{-}X}$*, b)* $x_{F4\text{-}Y}$*, and c)* $x_{F4\text{-}Z}$

One sample of the F1 to F5 period is taken. $\{x_{F1}, x_{F2}, \ldots, x_{F5}\}$ is used to denote the five samples. To simplify the data processing, the initial 1 s of the 10 s sampled data are used for analysis. Every signal contains 5200 points. x_{F4} is applied as a detailed example for analysis. The time domain is shown in Fig. 3.

In Fig. 3, we can see that these original signals can hardly provide enough complete feature information and the influences by noises and other disturbances are obvious. Based on the LCD algorithm, each signal has been decomposed and 10ISCs remained. After selection, the 6th ISC of $x_{F4\text{-}X}$, the 7th ISC of $x_{F4\text{-}Y}$ and the 4th ISC of $x_{F4\text{-}Z}$ remained. These are equally divided into segments. After Fourier transform, the coefficients X_i^j are achieved. Furthermore, $S_{CS}(f_k)$ can be calculated by Eq. (12).

3.2.1 DCS Power Spectral Entropy

Based on the procedures presented, the following result can be obtained: $SLPE = 3.863$ and $TLPE = 0.725$. Similarly, SLPE and TLPE of the remaining four stages can also be obtained. Data are considered to be one group of results. Then, SLPE and TLPE of the other nine samples in F1 to F5 are calculated. Results are shown in Figs. 4 and 5.

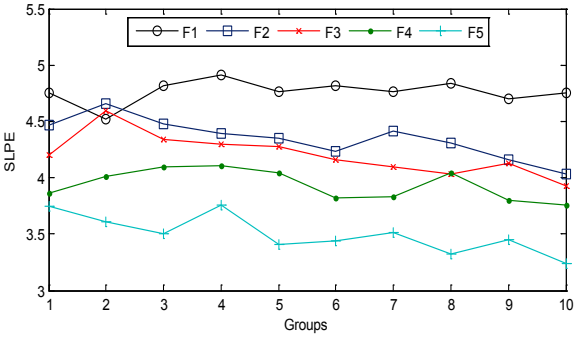

Fig. 4. *SLPE in F1 to F5 degradation stages*

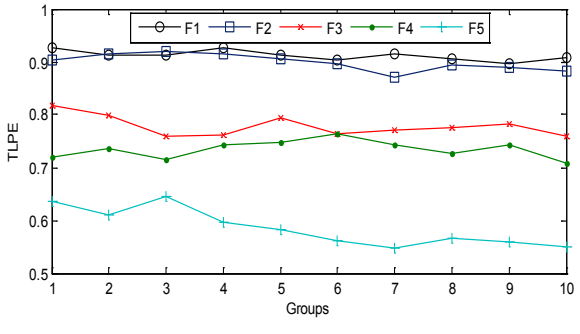

Fig. 5. *TLPE in F1 to F5 degradation stages*

Fig. 4 shows SLPE in various degradation stages. With the aggravation, SLPE tends to be reduced. This reveals the tracking ability of degradation changing. However, crossovers exist in neighbouring curves obviously, meaning that the distinguish ability of SLPE still needs to be improved. Fig. 5 shows the TLPE in various degradation stages. The crossover and overlapping of neighbouring curves become less, which reveals the complementary of TE to SE.

3.2.2 LCS High-Order Singular Spectral Entropy

Based on the procedures presented, the result can be obtained that: $SLSE = 3.227$ and $TLSE = 0.521$. Finally, totally 10 groups of results are achieved, which are shown in Figs. 6 and 7.

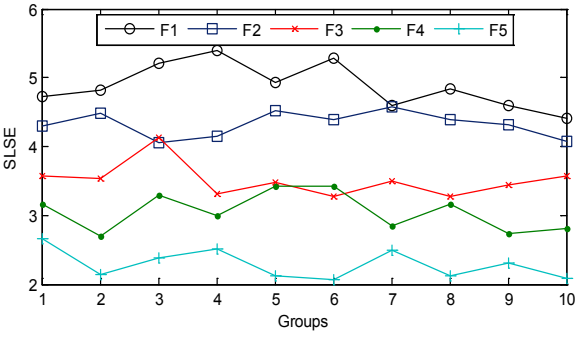

Fig. 6. *SLSE in F1 to F5 degradation stages*

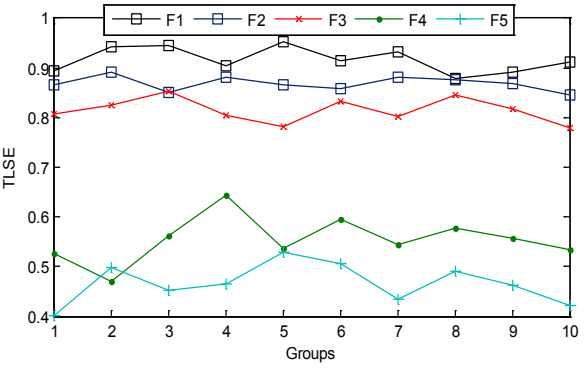

Fig. 7. *TLSE in F1 to F5 degradation stages*

Compared with LCS high-order power spectral entropies, crossover and overlapping in neighbouring curves of SLSE and SLTE are obviously reduced. This phenomenon means these two entropies possess better distinguishing ability than others. However, in detail, fluctuations in curves of SSE and STE are slightly more obvious, which shows the disadvantages in the stability of singular entropy.

3.2.3 Fusion of Features

The fusion of the ten groups of SLPE, TLPE, SLSE, TLSE in F1 to F5 are carried out, and the results are shown in Fig. 8.

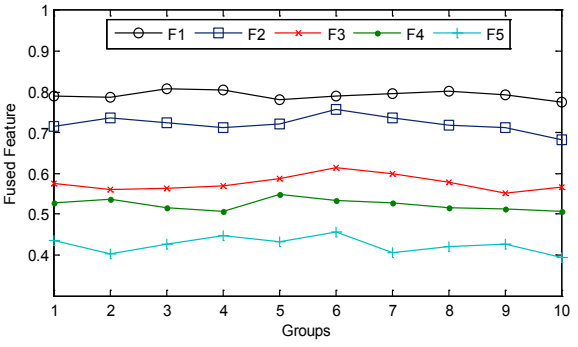

Fig. 8. *Fusion feature in F1 to F5 degradation stages*

3.2.4 Analysis and Comparison of Experimental Results

The double sample Z test **[35]** is applied for quantitative evaluation. Its computation is explained by:

$$Z = \left|\bar{X}_1 - \bar{X}_2\right| \Big/ (\mu_{X_1}^2 / n_1 + \mu_{X_2}^2 / n_2), \qquad (25)$$

where X_1 and X_2 denote sample sets of degradation feature X in various degradation stages. $\bar{X}$ and μ_X^2 respectively mean the average and variance of X. n is the number of samples. In comparison, the wavelet algorithm is used to process the three-channel signals. The amplitude and power of the characteristic frequencies of the constructed signal are extracted as the traditional features, which are marked as TF-1 and TF-2. Sensitivity is calculated. and results are shown in Table 2.

In Table 2, it can be seen that the traditional features TF-1 and TF-2, based on the wavelet fusion algorithm, could roughly describe the degradation. However, limited by the disadvantages of wavelet transform, the sensitivity of TF-1 and TF-2 are the lowest. Compared with TF-1 and TF-2, the performances of four features extracted by the proposed LCS fusion algorithm are improved. According to the sensitivity of various double samples, the extracted features are complementary to each other. However, some obviously redundant information still remains. Compared with the initial four features, the fused feature keeps the better performances of original features. Sensitivity to each double sample and the mean sensitivity of the fused feature are all the highest. Furthermore, there is only one feature after fusion, so that the conciseness would be greatly improved. This feature's fusion can effectively avoid contradiction disturbances by overloading the feature's information during the prognostic policy-decision stage.

Furthermore, the support vector machine (SVM) is applied for verifying the identification performance of the features. The four extracted features, the fused feature based on LPP algorithm **[26]** and the fused feature based on the proposed algorithm are made comparison. 30 samples of each stages of F1 to F5 have been used. There are a total of 150 values for each feature. The SVM identification results are shown in Table 3.

Table 2. *Sensitivity of various features*

Double Samples	Sensitivity						
	SLPE	TLPE	SLSE	TLSE	TF-1	TF-2	Fused feature
(F1, F2)	10.17	6.38	14.28	12.35	6.38	8.26	17.32
(F2, F3)	12.94	20.58	11.87	15.21	10.94	12.37	24.26
(F3, F4)	8.28	13.15	10.94	24.19	11.27	12.02	25.33
(F4, F5)	19.56	26.31	22.42	19.07	18.95	17.59	28.59
Mean sensitivity	12.74	16.61	14.88	17.70	11.89	12.56	23.88

Table 3. *Degradation stages identification accuracy of various features*

	F1 [%]	F2 [%]	F3 [%]	F4 [%]	F5 [%]	Total accuracy
SLPE	76.7	86.7	73.3	76.7	70	76.7
TLPE	73.3	90	76.7	70	83.3	78.7
SLSE	93.3	86.7	70	66.7	80	79.3
TLSE	76.7	83.3	80	80	83.3	80.6
Fused feature (LPP)	86.7	86.7	83.3	80	86.7	84.6
Fused feature (relative entropy)	93.3	93.3	90	86.7	86.7	90

Table 3 shows the result of the degradation stage identification with various features. As analysed previously, the sensitivity of SLPE to degradation is not very high. Therefore, the identification accuracy of SLPE to various degradation stages is the lowest. The accuracy of TLSE is the best of the four extracted features. However, the total accuracy of SLPE, TLPE, SLSE, and TLSE are close, ranging from 76 % to 80 %. Based on the LPP algorithm, the accuracy of the fused feature is improved to 84.6 %. Limited by the disadvantages, the identification of some stages has not changed so much before or after fusion. The proposed relative entropy fusion algorithm can make full use of the extracted feature information. Consequently, the identification accuracy of the fused feature to each stage and the total accuracy are all the highest. This means that the fused feature can evaluate various degradation stages of hydraulic pumps.

Above all, the comparison results show that the presented LCS algorithm gains the ability to extract more sensitive features. Meanwhile, unlike the traditional feature dimension reduction method, the relative entropy algorithm can make full use of each feature's information, so that the performance and concision of the fused feature will be both improved.

4 CONCLUSIONS

A novel fusion algorithm for extracting degradation feature is proposed here. Following the application in the degradation experiment, major conclusions are drawn, as follows:

1. LCS method for vibration signals fusion is presented to take advantages of fault information. LCS high-order power spectral entropy and high-order singular entropy defined in SE and TE are extracted as initial features.
2. The fusion method based on information entropy is proposed to make fusion of the initial features. The concision and performance are both effectively improved.
3. Experimental results showsthat the fused feature performances much better describe the degradation of hydraulic pump effectively.

5 ACKNOWLEDGEMENTS

This project is supported by National Natural Science Foundation of China (Grant No. 51305454). We are grateful to the Luoyang electronic equipment test centre of China for their support to our experiment. Furthermore, sincere appreciation is expressed to all anonymous contributors.

8 REFERENCES

[1] Ahmad, R., Kamaruddin, S. (2012). An overview of time-based and condition-based maintenance in industrial application. *Computers & Industrial Engineering*, vol. 63, no. 1, p. 135-149, **DOI:10.1016/j.cie.2012.02.002**.

[2] Coraddu, A., Oneto, L., Ghio, A., Savio, S., Figari, M., Anguita, D. (2015). Machine learning for wear forecasting of naval assets for condition-based maintenance applications. *International Conference on Electrical Systems for Aircraft, Railway, Ship Propulsion and Road Vehicles*, p. 1-5, **DOI:10.1109/ESARS.2015.7101499**.

[3] Lee, J., Wu, F., Zhao, W., Ghaffari, M., Liao, L., Siegel, D. (2014). Prognostics and health management design for rotary machinery systems-reviews, methodology and applications. *Mechanical Systems and Signal Processing*, vol. 45, no. 1-2, p. 314-334, **DOI: 10.1016/j.ymssp.2013.06.004**.

[4] Dong, S.J., Luo. T.H. (2013). Bearing degradation process prediction based on the PCA and optimized LS-SVM model, *Measurement*, vol. 46, no. 9, p. 3143-3152, **DOI:10.1016/j.measurement.2013.06.038**.

[5] Zhu, X. Zhang, Y., Zhu, Y. (2013). Bearing performance degradation assessment based on the rough support vector data description. *Mechanical Systems and Signal Processing*, vol. 34, no. 1, p. 203-207, **DOI:10.1016/j.ymssp.2012.08.008**.

[6] Wang, Y., Kang, S., Jiang, Y., Yang, G., Song, L., Mikulovich, V.I. (2012). Classification of fault location and the degree of performance degradation of a rolling bearing based on an improved hyper-sphere-structured multi-class support vector machine. *Mechanical Systems and Signal Processing*, vol. 29, p. 404-414, **DOI:10.1016/j.ymssp.2011.11.015**.

[7] Tran, V.T., Pham, H.T., Bo-Suk Yang, B.-S., Nguyen, T.T. (2012). Machine performance degradation assessment and remaining useful life prediction using proportional hazard model and support vector machine. *Mechanical Systems and Signal Processing*, vol. 32, p. 320-330, **DOI:10.1016/j.ymssp.2012.02.015**.

[8] Zhao, S.F., Liang, L., Xu, G.H., Wang, J., Zhang, W.M. (2013). Quantitative diagnosis of a spall-like fault of a rolling element bearing by empirical mode decomposition and the approximate entropy method. *Mechanical Systems and Signal Processing*, vol. 40, no. 1, p. 154-177, **DOI:10.1016/j.ymssp.2013.04.006**.

[9] Dong, S.J., Tang, B.P., Chen, R.X. (2013). Bearing running state recognition based on non-extensive wavelet feature scale entropy and support vector machine. *Measurement*, vol. 46, no. 10, p. 4189-4199, **DOI:10.1016/j.measurement.2013.07.011**.

[10] Sun, J., Li, H., Xu, B. (2016). Degradation feature extraction of the hydraulic pump based on high-frequency harmonic local characteristic-scale decomposition sub-signal separation and discrete cosine transform high-order singular entropy. *Advances in Mechanical Engineering*, vol. 8, no. 7, p. 1-12, **DOI:10.1177/1687814016659601**.

[11] Wang, J.P., Hu, H.T. (2006). Vibration-based fault diagnosis of pump using fuzzy technique. *Measurement*, vol. 39, no. 2, p. 176-185, **DOI:10.1016/j.measurement.2005.07.015**.

[12] Sun, J., Li, H.R., Xu, B.H. (2016). The morphological undecimated wavelet decomposition - discrete cosine

transform composite spectrum fusion algorithm and its application on hydraulic pumps. *Measurement*, vol. 94, p. 794-805, **DOI:10.1016/j.measurement.2016.09.024**.

[13] Du, J., Wang, S.P., Zhang, H.Y. (2013). Layered clustering multi-fault diagnosis for hydraulic piston pump. *Mechanical Systems and Signal Processing*, vol. 36, no. 2, p. 487-504, **DOI:10.1016/j.ymssp.2012.10.020**.

[14] Angelov, P., Yager, R. (2013). Density-based averaging - A new operator for data fusion. *Information Science*, vol. 222, p. 163-174, **DOI:10.1016/j.ins.2012.08.006**.

[15] Rodger, J.A. (2012). Toward reducing failure risk in an integrated vehicle health maintenance system: A fuzzy multi-sensor data fusion Kalman filter approach for IVHMS. *Expert Systems with Applications*, vol. 39, no. 10, p. 9821-9836, **DOI:10.1016/j.eswa.2012.02.171**.

[16] Geng, H., Liang, Y., Liu, Y.R., Alsaadi, F.E. (2018). Bias estimation for asynchronous multi-rate multi-sensor fusion with unknown inputs. *Information Fusion*, vol. 39, no. 1, p. 139-153, **DOI:10.1016/j.inffus.2017.03.002**.

[17] Wei, C.M., Blum, R.S. (2010). Theoretical analysis of correlation-based quality measures for weighted averaging image fusion. *Information Fusion*, vol. 11, no. 4, p. 301-309, **DOI:10.1016/j.inffus.2009.10.006**.

[18] Yang, W.B., Li, S.Y. (2014). A switch-mode information fusion filter based on ISRUKF for autonomous navigation of spacecraft. *Information Fusion*, vol. 18, no. 1, p. 33-42, **DOI:10.1016/j.inffus.2013.04.012**.

[19] Elbhbah, K., Sinha, J.K. (2013). Vibration-based condition monitoring of rotating machines using a machine composite spectrum. *Journal of Sound and Vibration*, vol. 332, no. 11, p. 2831-2845, **DOI:10.1016/j.jsv.2012.12.024**.

[20] Yunusa-Kaltungo, A., Sinha, J.K., Elbhbah, K. (2014). An improved data fusion technique for faults diagnosis in rotating machines. *Measurement*, vol. 58, no. 1, p. 27-32, **DOI:10.1016/j.measurement.2014.08.017**.

[21] Jinde, Z., Junsheng, C., Yu, Y. (2013). A rolling bearing fault diagnosis approach based on LCD and fuzzy entropy. *Mechanism and Machine Theory*, vol. 70, no. 1, p. 441-453, **DOI:10.1016/j.mechmachtheory.2013.08.014**.

[22] Junsheng, C., Yi, Y., Yu, Y. (2012). Local characteristic-scale decomposition method and its application to gear fault diagnosis. *Journal of Mechanical Engineering*, vol. 48, no. 9, p. 45-49, **DOI:10.3901/JME.2012.09.064**.

[23] Zhu, K.H., Song, X.G., Xue, D.X. (2014). A roller bearing fault diagnosis method based on hierarchical entropy and support vector machine with particle swarm optimization algorithm. *Measurement*, vol. 47, p. 669-675, **DOI:10.1016/j.measurement.2013.09.019**.

[24] Li, H.J., Xie, X.P. (2015). Gear fault pattern recognition based on kernel feature fuzzy clustering and fuzzy association entropy. *Chinese Journal of Scientific Instrument*, vol. 36, no. 4, p. 849-854.

[25] Gharavian, M.H. Almas Ganj, F., Ohadi, A.R., Heidari Bafroui, H. (2013). Comparison of FDA-based and PCA based features in fault diagnosis of automobile gearboxes. *Neurocomputing*, vol. 121, no. 1, p. 150-159, **DOI:10.1016/j.neucom.2013.04.033**.

[26] Deng, X.G., Tian, X.M. (2013). Sparse kernel locality preserving projection and its application in nonlinear process fault detection. *Chinese Journal of Chemical Engineering*, vol. 21, no. 2, p. 163-170, **DOI:10.1016/S1004-9541(13)60454-1**.

[27] Dornaika, F., Assoum, A. (2013). Enhanced and parameterless locality preserving projections for face recognition. *Neurocomputing*, vol. 99, no. 1, p. 448-457, **DOI:10.1016/j.neucom.2012.07.016**.

[28] Krawczak, M., Szkatula, G. (2014). An approach to dimensionality reduction in time series. *Information Sciences*, vol. 260, no. 1, p. 15-36, **DOI:10.1016/j.ins.2013.10.037**.

[29] Kristoufek, L. (2014). Measuring correlations between non-stationary series with DCCA coefficient. *Physica A: Statistical Mechanics and its Applications*, vol. 402, p. 291-298, **DOI:10.1016/j.physa.2014.01.058**.

[30] Zarinbal, M., Fazel Zarandi, M.H., Turksen, I.B. (2014). Relative entropy fuzzy c-means clustering. *Information Sciences*, vol. 260, p. 74-97, **DOI:10.1016/j.ins.2013.11.004**.

[31] Sun, J., Li, H.R., Xu, B.H. (2016). Degradation feature extraction of the hydraulic pump based on high-frequency harmonic local characteristic-scale decomposition sub-signal separation and discrete cosine transform high-order singular entropy. *Advances in Mechanical Engineering*, vol. 8, no. 7, p. 1-12, **DOI:10.1177/1687814016659601**.

[32] Rufeil Fiori, E., Plastino, A. (2013). A Shannon-Tsallis transformation. *Physica A: Statistical Mechanics and its Applications*, vol. 392, no. 8, p. 1742-1749, **DOI:10.1016/j.physa.2012.12.037**.

[33] Caraiani, P. (2014). The predictive power of singular value decomposition entropy for stock market dynamics. *Physica A: Statistical Mechanics and its Application*, vol. 393, p. 571-578, **DOI:10.1016/j.physa.2013.08.071**.

[34] Zarinbal, M., Fazel Zarandi, M.H., Turksen, I.B. (2014). Relative entropy fuzzy c-means clustering. *Information Science*, vol. 260, no. 1, p. 74-97, **DOI:10.1016/j.ins.2013.11.004**.

[35] Zhe, C. (2011). *Theory and Method on Damage Modeling and Prognostics for Planetary Gear Set of Helicopter Transmission System*. PhD Thesis, National University of Defense Technology, Changsha.

Strojniški vestnik - Journal of Mechanical Engineering 64(2018)1, 26-36
DOI:10.5545/sv-jme.2017.4989
Original Scientific Paper
Received for review: 2017-10-14
Received revised form: 2017-11-27
Accepted for publication: 2017-11-29

Numerical Study of Heat Transfer Enhancement for Low-Pressure Flows in a Square Cavity with Two Fins Attached to the Hot Wall Using Al_2O_3-Air Nanofluid

Wael Al-Kouz[1,*] – Suhil Kiwan[2] – Ammar Alkhalidi[3] – Ma'en Sari[4] – Aiman Alshare[1]

[1] German Jordanian University, Mechatronics Engineering Department, Jordan
[2] Jordan University of Science and Technology, Mechanical Engineering Department, Jordan
[3] German Jordanian University, Energy Engineering Department, Jordan
[4] German Jordanian University, Mechanical and Maintenance Engineering Department, Jordan

The gaseous low-pressure nanofluid flow of a steady-state two-dimensional laminar natural convection heat transfer in a square cavity of length L with two attached solid fins to the hot wall is numerically investigated. Such flows are found in many engineering applications, such as nuclear reactors and electronic cooling equipment. Physical parameter ranges in this study are as follows: $0 \le Kn \le 0.1$, $10^3 \le Ra \le 10^6$, $0 \le \phi \le 0.2$, L_F/L takes the value of 0.5, H_F takes the values of 0.25 to 0.75. Simulation results show that Nusselt number depends directly on the Rayleigh number and inversely on the Knudsen number. In addition, it is found that heat transfer will be enhanced by dispersing the nanoparticles of Al_2O_3 in the base low-pressure gaseous flow. Moreover, it is found that the Nusselt number of such flows increases as the nano-particle volume fraction increases for the investigated range of volume fractions considered in this study. In addition, a correlation of the Nusselt number among all the investigated parameters in this study is proposed as $Nu = 0.2196\, Ra^{0.0829}\, Kn^{-0.511}\, \phi^{0.104}$.

Keywords: natural convection, heat transfer, low pressure, cavity

Highlights

- *This research aims to study numerically laminar steady natural convection flow in a cavity in which two solid fins are attached to the hot side wall.*
- *The cavity was filled with air-Al_2O_3 nanofluid.*
- *The effects of the Knudsen number, the Rayleigh number and the volume fraction of the nanoparticles were investigated.*
- *It was found that the heat transfer rate is enhanced by increasing the volume fraction of the nanoparticles, increasing the Rayleigh number and decreasing the Knudsen number.*

0 INTRODUCTION

Natural convection in enclosed cavities can be found in many engineering applications, such as those found in nuclear reactor cooling, energy transfer in buildings, and electronic equipment cooling. The goal of this study is to investigate the effect of adding Al_2O_3 nanoparticles on the flow and heat characteristics of the low-pressure slip gaseous airflow in a square cavity in which the hot wall is attached to two fins. Moreover, the effect of the Knudsen number (Kn), the Rayleigh number (Ra) and volume fraction of the nanoparticles on these characteristics will be addressed and discussed thoroughly.

A low-pressure flow is classified based on (Kn). Referring to Schaaf and Chambre **[1]**; Cercignani and Lampis **[2]**, four different flow regimes are identified: continuum regime, slip regime, transitional regime, and free molecular regime. For slip flows, both slip velocity and temperature jump boundary conditions are applied at the surfaces.

Due to the importance of natural convection in cavities, extensive studies have been conducted, both experimentally and numerically. For instance, Bilgen **[3]** studied the natural convection heat transfer in differentially heated cavities numerically. In his study, streamlines and isotherms are produced, and effects of the Rayleigh number and the relative conductivity ratio on the flow characteristics is carried out. The results show that the Nusselt number increases as the Rayleigh number increases and the Nusselt number decreases as the relative conductivity ratio increases. Alkhalidi et al. **[4]** investigated the buoyancy-driven heat transfer in rarefied gas inside a conjugate cavity. The governing equations along with the slip flow and temperature jump boundary conditions are solved using a finite-volume technique. Simulations are carried out for different conductivity ratios, Rayleigh numbers, and cavity tilt angles. Moreover, a correlation among the Nusselt number and those parameters is proposed. In their study, Benseghir and Rahal **[5]** carried out a numerical simulation of heat transfer in a square cavity with two fins attached to

*Corr. Author's Address: 1German Jordanian University, Mechatronics Engineering Department, Jordan, wael.alkouz@gju.edu.jo

the hot wall. A parametric study is presented for the Rayleigh number equalling 10^5 and different dimensionless positions of the fin. They determined that there is an optimum position of the fins to achieve the maximum heat transfer. In their work, Al-Kouz et al. [6] numerically investigated low-pressure flow and heat transfer characteristics in an inclined enclosed cavity in which the hot wall is attached to two fins, the effects of the Knudsen number, the Rayleigh number, porosity of the fins, location of the fins, length of the fins, tilt angle and the conductivity ratio are presented. In addition, a correlation of the Nusselt number among these parameters is proposed. In the reviewed work conducted by Öztop et al. [7], two- and three-dimensional numerical investigations along with experimental techniques are used to investigate the effects of the type and location of the heat source on the flow and heat characteristics of the flow inside enclosed cavities. Furthermore, the effects of different boundary conditions and different configurations on the flow and heat characteristics inside enclosed cavities are identified and reported.

Enhancement of heat transfer by utilizing nanofluid has attracted great attention and motivated the investigation of such flows in recent decades. This is mainly due to their relevance to many engineering applications, such as those found in automotive cooling industry. Due to the increasing need for ultrahigh performance cooling systems, nanofluids have been recently investigated as next-generation coolants for car radiators as stated by Bigdeli et al. [8]. Furthermore, nanofluids can be found in the electronic cooling industry and many others.

Akbari et al. [9] studied forced the turbulent convection of Al_2O_3-water and Cu-water inside horizontal tubes. They showed that dispersing the nanosolid particles in the flow improves thermophysical and thus enhances heat transfer. However, some penalties are paid due to the increase in pressure drop. Balandin et al. [10] reported that by adding graphene to the base fluid, the resulting thermal conductivity will enhance heat transfer.

Experimental and numerical works have revealed many different types of nanoparticles that have been used to enhance the heat transfer; these include but are not limited to metals and oxide metals. In this research, we will consider adding Al_2O_3 to the base fluid (low-pressure air) in a square cavity in which the hot wall is attached to two fins.

The type and concentration of the nanoparticles affect the thermal behaviour of the resulting nanofluid. Many research studies, both numerical and experimental have tackled this issue such as Akbari et al. [9], Balandin et al. [10], Kalteh et al. [11], and Hussein et al. [12].

Excellent reviews of the heat transfer characteristics of nanofluid in forced and free convection flows can be found in the studies of Wang and Mujumdar [13], Yu et al. [14], Sarkar et al. [15], Saidur et al. [16], Suresh et al. [17] and Hussien et al. [12].

A state-of-the-art review of the viscosity of nanofluid is given in Murshed and Estellé [18], in which different models available in the literature along with their application range are reported. Also, effects of temperature and the concentration of the nanoparticles on the heat transfer characteristics have been identified and explicitly reviewed.

Dispersing Al_2O_3 in the base fluid is a common practice in many thermal applications. Adding these particles will enhance the thermal conductivity of the resulting fluid.

Labib et al. [19] computationally investigated the effect of base fluid on convective heat transfer utilizing Al_2O_3 nanoparticles. Their results show that ethylene-glycol-base fluid will give better heat transfer enhancement than that of water.

Experimental investigation of convective heat transfer of Al_2O_3 water nanofluid in circular tubes has been studied by Heris et al. [20], Nusselt numbers of nanofluids were obtained for different nanoparticle concentrations as well as for different Reynold and Peclet numbers. Experimental results show that mixing the base fluid with nanoparticles is superior to the single base fluid as far as the heat transfer enhancement is concerned. In the work presented by Moghadassi et al. [21], CFD modelling of a horizontal circular tube was utilized to study the effect of nanofluids on laminar forced convective heat transfer. In their study, water-based Al_2O_3 and Al_2O_3-Cu hybrid nanofluids were considered. The results show that the hybrid nanofluid resulted in a higher convective heat transfer coefficient. Experimental results illustrated by Noie et al. [22] show that suspended nanoparticles (Al_2O_3) in water nanofluid enhanced the heat transfer in a two-phase closed thermosyphon; different volume fractions were taken into consideration. In their work, results show that the efficiency of the two-phase closed thermosyphon increases up to (14.7 %) when adding Al_2O_3 nanoparticles to the base fluid.

Salman et al. [23] solved numerically laminar convective heat transfer in a two-dimensional microtube with constant heat flux. They considered different types of nanofluids with different nanoparticle sizes and different volume fractions. They found that the Nusselt number increases

with the volume fraction and decreases with the nanoparticle size. Moreover, the Nusselt number increases with the Reynolds Number. Williams et al. [24] investigated the turbulent convective heat transfer and pressure loss of aluminium water nanofluid in horizontal tubes; different particle concentrations were considered. They compared their results with the available traditional single-phase correlations for fully developed flow; no abnormal heat transfer enhancement was observed in the study. Steady laminar mixed convection flow in a lid-driven square cavity filled with Al_2O_3 water nanofluid was investigated computationally by Taamneh and Bataineh [25]. Different volume fractions of the nanoparticles as well as different Richardson numbers were considered. Simulation results show that adding nanoparticles to the base fluid will increase the heat transfer rate. In addition, increasing the Richardson number increases the average Nusselt number.

Although there are many research studies that deal with the heat transfer characteristics, there is a lack of studies that consider the heat transfer characteristics of low-pressure gaseous nanofluids. In this paper, further insight on adding nanoparticles to the low-pressure gaseous flow and heat transfer characteristics in the square cavity of length L in which two solid fins are attached to the hot wall is provided. In the present study, $0 \leq \phi \leq 0.2$, $0 \leq Kn \leq 0.1$ to cover both continuum and slip flow regimes. $10^3 \leq Ra \leq 10^6$ to study the effect of both conduction dominant versus convection dominant modes of heat transfer. L_F/L is set to 0.5 m; H_F takes the value of 0.25 to 0.75. A finite volume numerical computational fluid dynamics (CFD) solution utilizing the Boussinesq approximation is used to obtain the solution for such flows. The Prandtl number (Pr) is taken to be constant and is equal to 0.7. The Knudsen number was varied by controlling the pressure inside the cavity. The effects of Kn, Ra, and the nanoparticles' volume fraction on the flow and heat transfer characteristics are investigated.

1 MATHEMATICAL FORMULATION

1.1 Governing Equations

In this study, two-dimensional laminar and steady-state natural convection flow is investigated. The Boussinesq approximation is utilized to account for the buoyancy force, and all other fluid properties are considered constant. Fig. 1 represents flow in the geometry under investigation, which is a square cavity of length L in which two fins are attached to the hot wall. In this study, continuum and slip flow regimes are considered.

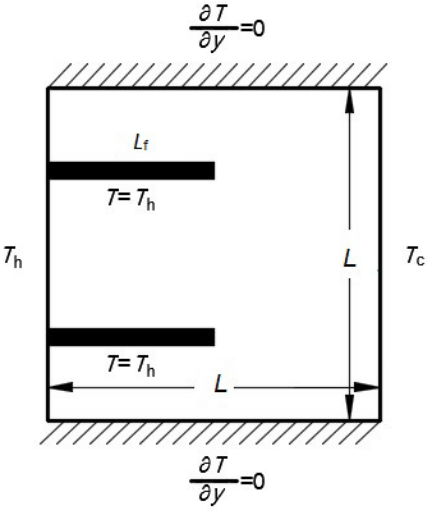

Fig. 1. *The geometry used for the computational domain*

Adding nanoparticles to the base fluid will change the thermophysical properties of the resulting nanofluid. It is assumed that the suspension of the nanoparticles is homogeneous with well-dispersed nanoparticles (i.e. no particle aggregation). Following Hussien et al. [12] and Cardellini et al. [26], the properties of the nanofluid can be calculated based on the following equations:

Viscosity:

We adapted the Brinkman model [27] for viscosity since the range of the volume fraction of the nanosolid particles investigated is below 0.2. It is also important to mention here that we had examined the results from another viscosity model, of Hatschek [28] for $\phi = 0.2$ and the difference between the Brinkman model and Hatcheck model is less than 1% for $\phi = 0.2$.

The Brinkman model for viscosity is as follows:

$$\mu_{nf} = \frac{\mu_f}{(1-\varphi)^{2.5}}. \tag{1}$$

Density:

$$\rho_{nf} = (1-\varphi)\rho_f + \varphi\rho_s. \tag{2}$$

Heat capacitance:

$$Cp_{nf} = (1-\varphi)(Cp)_f + \varphi(Cp)_s. \tag{3}$$

Thermal expansion coefficient:

$$\beta_{nf} = \beta_f \left[\frac{1}{1+\frac{(1-\varphi)\rho_f}{\varphi\rho_s}\frac{\beta s}{\beta_f}} + \frac{1}{1+\frac{\varphi\rho_s}{1-\varphi\rho_f}} \right]. \quad (4)$$

Thermal conductivity:

Following the Maxwell-Garnett (MG) **[29]** model and based on the assumption that the suspension is homogeneous with well-dispersed nanoparticles, then:

$$k_{nf} = k_f \frac{k_s + 2k_f - 2\varphi(k_f - k_s)}{k_s + 2k_f + \varphi(k_f - k_s)}. \quad (5)$$

Table 1 summarizes the thermophysical properties used to obtain the resulting properties of the Al_2O_3-air nanofluid.

Table 1. *Thermophysical properties for air and Al_2O_3*

Physical properties	Air	Al_2O_3
C_p [J/(kg K)]	1006.43	765
ρ [kg/m^3]	1	3970
k [W/m^{2}K]	0.025	40
β [1/K]	0.00333	0.0000085
α [m^2/s]	0.000019	0.00001317

To calculate the resulting properties of the nanofluid, user-defined functions (UDFs) were used in Fluent 18. The governing equations that describe the problem under investigation are summarized below:

Continuity:

$$\frac{\partial u}{\partial x} + \frac{\partial v}{\partial y} = 0. \quad (6)$$

x- momentum:

$$\rho_{nf}\left(u\frac{\partial u}{\partial x} + v\frac{\partial u}{\partial y} \right) = -\frac{\partial P}{\partial x} + \mu_{nf}\left[\frac{\partial^2 u}{\partial x^2} + \frac{\partial^2 u}{\partial y^2} \right]. \quad (7)$$

y- momentum:

$$\rho_{nf}\left(u\frac{\partial v}{\partial x} + v\frac{\partial v}{\partial y} \right) = -\frac{\partial P}{\partial y} - \rho_{nf} g + \mu_{nf}\left[\frac{\partial^2 v}{\partial x^2} + \frac{\partial^2 v}{\partial y^2} \right]. \quad (8)$$

Energy:

$$\rho_{nf} C_{pnf}\left(u\frac{\partial T}{\partial x} + v\frac{\partial T}{\partial y} \right) = k_{nf}\left[\frac{\partial^2 T}{\partial x^2} + \frac{\partial^2 T}{\partial y^2} \right]. \quad (9)$$

The boundary conditions applied for the slip flow regime are the temperature jump and slip velocity at the hot and cold walls of the cavity; reported by Karniadakis et al. **[30]**, Lockerby et al. **[31]** and Kandlikar et al. **[32]** as follows:

$$u_w - u_g = \left(\frac{2-\sigma_v}{\sigma_v} \right) \lambda \frac{\partial u}{\partial n} \approx \left(\frac{2-\sigma_v}{\sigma_v} \right) Kn\left(u_g - u_c \right), \quad (10)$$

$$v_g = 0, \quad (11)$$

$$T_w - T_g = \left(\frac{2-\sigma_T}{\sigma_T} \right) \frac{2\gamma}{\gamma+1} \frac{k}{\mu c_v} \lambda \frac{\partial T}{\partial n} \approx$$

$$\approx \left(\frac{2-\sigma_T}{\sigma_T} \right) \frac{2\gamma}{\gamma+1} \frac{k}{\mu c_v} K_n\left(T_g - T_c \right), \quad (12)$$

where σ_v and σ_T represent the momentum and thermal accommodation coefficients.

The corresponding Knudsen number is defined as follows:

$$Kn = \frac{\lambda}{L}, \quad (13)$$

where λ is the mean free path, and L is the length of the square cavity.

Thermal boundary conditions are imposed at $x=0$ and L such that:

At $(x = 0, y)$, $T = T_h$, (14)

At $(x = L, y)$, $T = T_c$, (15)

where T_h is the hot surface temperature, and T_c is the cold surface temperature, the fins' temperature is set to T_h.

The local heat flux is calculated as follows:

$$q''_F = -k\frac{\partial T}{\partial n}\Big|_F, \quad (16)$$

$$q''_h = -k\frac{\partial T}{\partial n}\Big|_h, q''_c = -k\frac{\partial T}{\partial n}\Big|_c. \quad (17)$$

Heat transfer from the hot to the cold wall is calculated by integrating the local heat flux along the wall of the hot wall and the fins as follows:

$$Q = \sum \left(\int_{A_h} q''_h dA_h + \int_{A_F} q''_F dA_F \right) = \int_{A_c} q''_c dA_c. \quad (18)$$

Then, the average heat transfer coefficient along the wall of the hot surface and the fin or along the wall of the cold surface is calculated by combining Eqs. (16) to (18).

$$\bar{h} = \frac{Q}{(T_i - T_\circ)A_T} = \frac{Q}{(T_i - T_\circ)A_c}. \quad (19)$$

From Eq. (19), the average Nusselt number can be calculated as follows based on the unit length of the cavity:

$$Nu = \frac{\bar{h}L}{k_{nf}} = \frac{\bar{h}}{k_{nf}}. \quad (20)$$

2 NUMERICAL SOLUTION

In this study, a finite volume analysis is used to serve as a method of solution for the problem under investigation. Initially, a mesh of 40×40 elements is tested. The SIMPLE algorithm, reported by Versteeg and Malalasekera **[33]** and Patankar and Spalding **[34]**, is used. In addition, the PRESTO algorithm is utilized to calculate the pressure field. To differentiate the convective terms, a hybrid second order accuracy scheme of central and upwind difference is used. All momentum and thermal accommodation coefficients are assumed to be unified for all simulations. It is worth mentioning here that the effect of the momentum and thermal accommodation coefficients on the Nusselt number has been examined; it was found that the Nusselt number is insensitive to these coefficients in comparison to the rest of the parameters considered in this study. Table 2 illustrates the effects of momentum and thermal accommodation coefficients on the Nusselt number for the case in which $Ra = 10^6$, $\phi = 0.02$ and $Kn = 0.05$, the table shows that these coefficients have almost negligible effects on the Nusselt number. The solution is considered to be converged when the maximum of the normalized absolute residual across all nodes is less than 10^{-6}.

Table 2. *Effects of the momentum and thermal accommodation coefficients on the Nusselt number for the case in which Ra = 10⁶, ϕ = 0.02 and Kn = 0.05*

σ_v	σ_T	Nu
0	0	1.9582
0.05	0.05	1.9586
1	1	1.9588

3 GRID INDEPENDENCE

The grid that was used in all simulations is illustrated in Fig. 2. It consists of a two-dimensional mesh. As a starting mesh, the grid step sizes are increasing in the x and y directions with expansion factors of 1.06 and 1.15, respectively; these values were chosen in order to capture the gradients' near solid-fluid interface. Then the mesh was adapted in which velocity gradients near the solid surfaces are calculated. More cells were added to reduce the gradients below a certain value. It was observed that any further change in these parameters would not affect the results. A grid sensitivity analysis test is carried out by monitoring the average Nusselt number at the cold wall, and solutions were obtained for different numbers of grid nodes. It was obvious that adding more cells beyond a certain value will not change the value of the average Nusselt number at the cold surface of the square cavity.

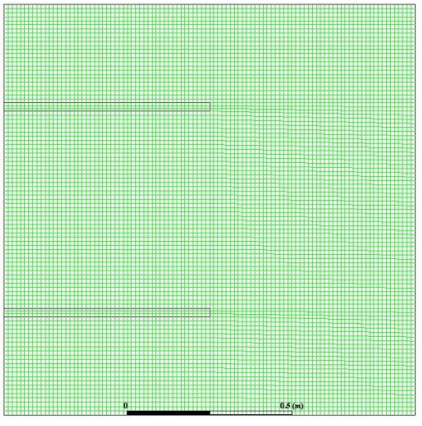

Fig. 2. *Adaptive grid system technique used in the simulations*

Fig. 3 demonstrates that the solution is mesh-independent for a grid of 100×100 nodes. This grid size is used for all simulations conducted in this research.

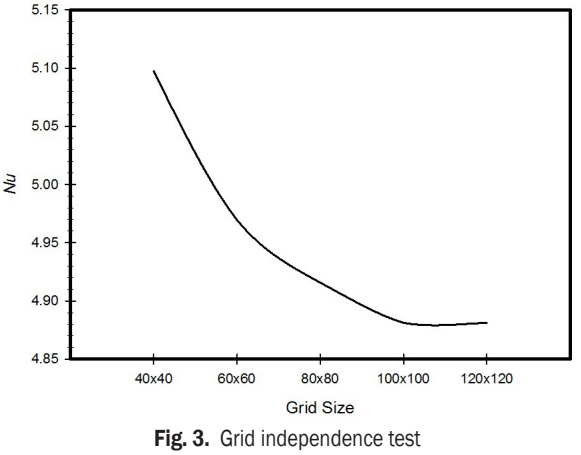

Fig. 3. Grid independence test

4 CODE VERIFICATION

To verify the numerical code, the results of the current code are compared with the results obtained by De Vahl Davis and Jones **[35]**, De Vahl Davis **[36]**

and Sarkar et al. [37] for the case of gaseous airflow inside a square cavity with no fins attached to the hot wall. Table 3 shows a comparison between the mean Nusselt number at the cold surface obtained by the current code and that obtained by [35] to [37] at Ra = 10^4, 10^5 and 10^6. Comparisons show excellent agreement with an error of less than 1 %. In addition, Fig. 4 shows results from the current code compared to the results obtained by Taamneh and Bataineh [25] at ϕ = 0.01 and different Richardson numbers (Ri) for the case of mixed convection heat transfer in a square-lid-driven cavity filled with water/Al_2O_3 nanofluid. The figure illustrates that there is a maximum error of 3 %.

Table 3. *Comparison between results obtained from present study and those obtained by* [35] *to* [37]

Ra	10^4	10^5	10^6
[35], [36]	2.243	4.519	8.800
[37]	2.24	4.51	8.82
Present study	2.241	4.52	8.83

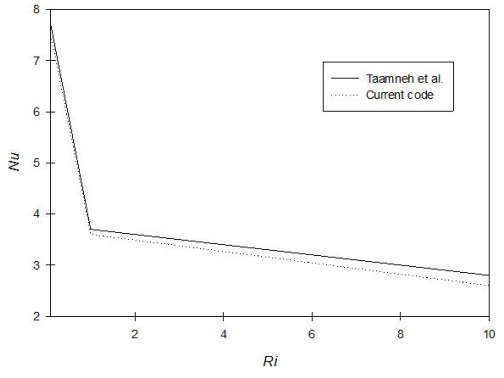

Fig. 4. *Comparison between results obtained from the current code to results obtained by Taamneh and Bataineh* [25]

5 RESULTS AND DISCUSSION

Fig. 5 shows the velocity stream function contours inside the square cavities with a fin position of H_F = 0.25 to 0.75 and fin lengths of 0.5 m for the cases with Knudsen number values of zero, 0.01, 0.05 and 0.1 to cover the continuum and slip flow regimes. Moreover, two different values of the nanoparticles volume fraction of ϕ=0.01 and 0.2 are also considered. The streamlines are plotted for cases where Ra=10^5. By inspecting the streamlines, it is obvious from the graphs that a large clockwise rotating cell is formed. By increasing the Knudsen number by the same volume fraction, less circulation is observed inside the cavity in the regions between the two fins, between the upper fin and the upper wall, and between the lower fin and the lower wall. This decrease in circulation and distortion of the streamlines will affect the heat transfer characteristics as will be shown later. The hot fluid near the hot wall (left wall) is rising and replacing the cold fluid near the cold wall (right wall) that is falling. For the cases of ϕ=0.2 and different Knudsen numbers, it is clear that more changes to the flow are observed (more recirculating regions) in comparison to ϕ=0.01. Greater recirculation in the flow and distorted streamlines will lead to better heat transfer enhancement.

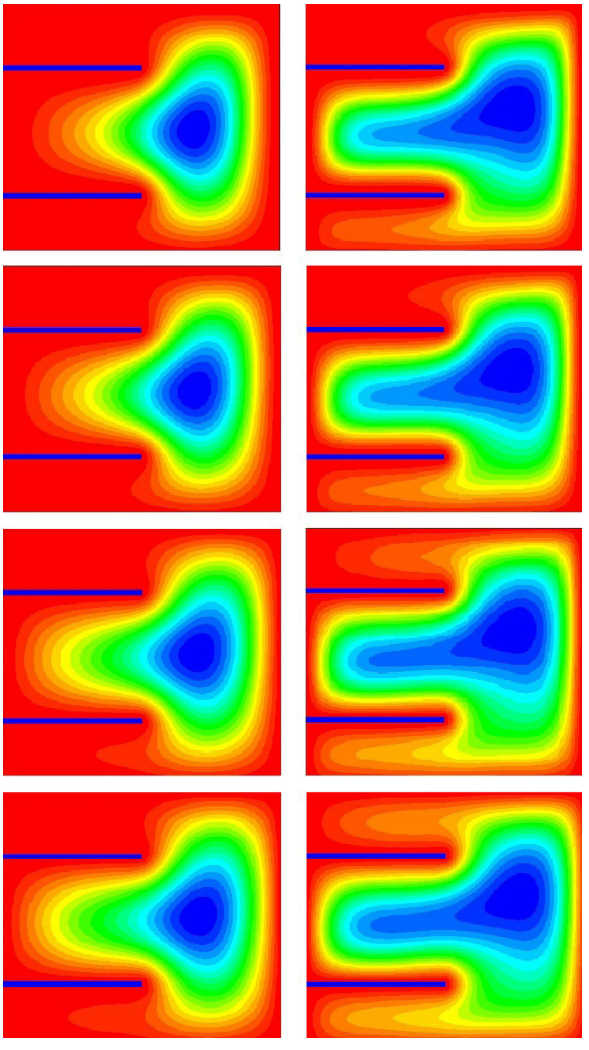

Fig. 5. Streamlines, Kn = 0, 0.01, 0.05, 0.1 at two different nanoparticle volume fractions (ϕ=0.01 and 0.2)

Fig. 6 shows the isothermal contours inside the square cavities for the same cases and parameter values considered in Fig. 4. By observing the contours for the case of ϕ=0.01 and different Knudsen numbers. It is

found that for the case of higher Knudsen numbers, mostly the area near the fins are affected while the rest of the cavity is almost unaffected; for the case of the Knudsen number equalling zero, more area inside the cavity is affected and more distortion of the contours occurred. For the case of $\phi = 0.2$, remarkable distortion and recirculation in the flow are happening compared to the cases of $\phi = 0.01$. It is also obvious that by increasing the Knudsen number, less distortion, mixing and recirculation of the flow are happening. This will affect the heat transfer characteristics.

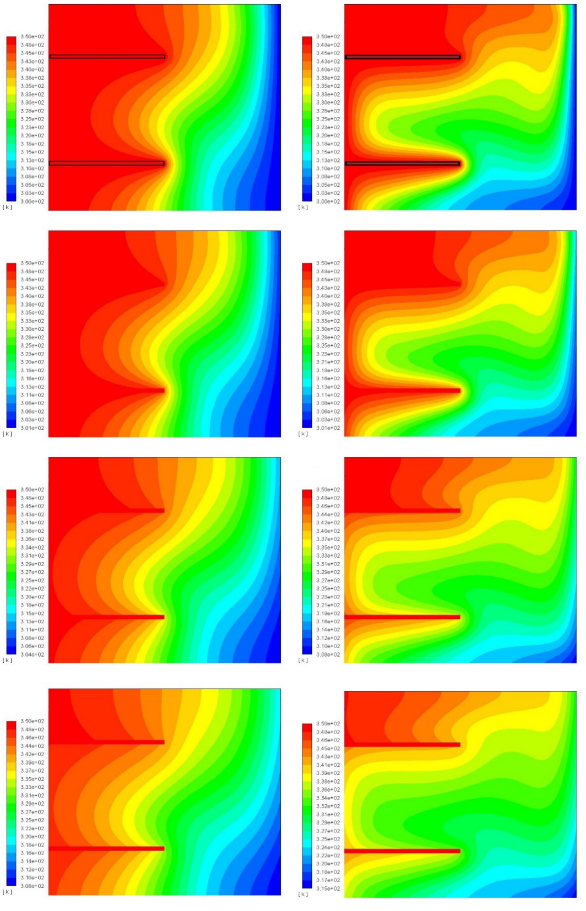

Fig. 6. *Isotherms, Kn = 0, 0.01, 0.05, 0.1 at two different nanoparticle volume fractions ($\phi = 0.01$ and 0.2)*

Fig. 7 illustrates the variation in the vertical velocity V_y along the horizontal centreline of the cavity with the length of the cavity (L), in which the Knudsen number takes the value of 0.05 and different values of Rayleigh numbers. The graph shows that as that Rayleigh number increases the vertical velocity near the walls will increase; this will enhance the heat transfer. It is worth mentioning here that in the region away from the walls; the vertical velocity is almost constant, which means that the dominant mode of heat transfer in this region is conduction, while at the walls it is convection. For low values of Rayleigh number, the figure indicates that there is no variation of the vertical velocity, and the dominant mode of heat transfer is condution.

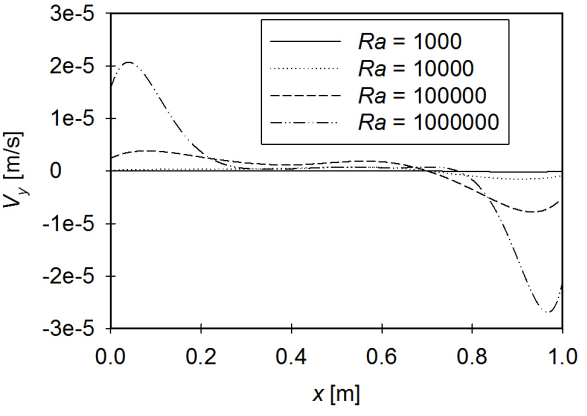

Fig. 7. *Variation of the vertical velocity (V_y) with the length of the cavity (L) for different Rayleigh numbers, Kn = 0.05*

In Fig. 8, the temperature distributions T along the horizontal centreline of the cavity are plotted against the length of the cavity (L) for different Rayleigh numbers at a fixed value of the Knudsen number of 0.05. The graph shows that as the Rayleigh number increases, the convection heat transfer becomes the dominant mode of heat transfer, this is very clear from the variation of the temperature at the wall boundaries for higher Rayleigh numbers. For the cases of lower values of Rayleigh numbers, the conduction mode of heat transfer dominates.

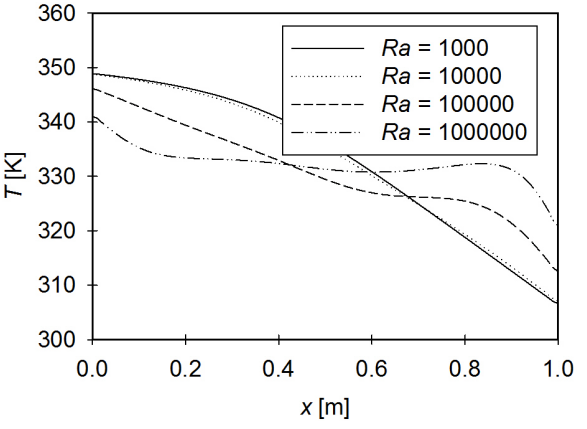

Fig. 8. *Variation of the temperature (T) with the length of the cavity (L) for different Rayleigh numbers, Kn = 0.05*

Vertical velocity (V_y) variations along the centreline of the cavity at constant Rayleigh number

of 10^6 and different Knudsen numbers that cover the continuum and slip regimes are plotted in Fig. 9. The graph shows that as the Knudsen number increases then the slip velocity at the boundaries will increase; this will result in less heat transfer and, consequently, a lower Nusselt number.

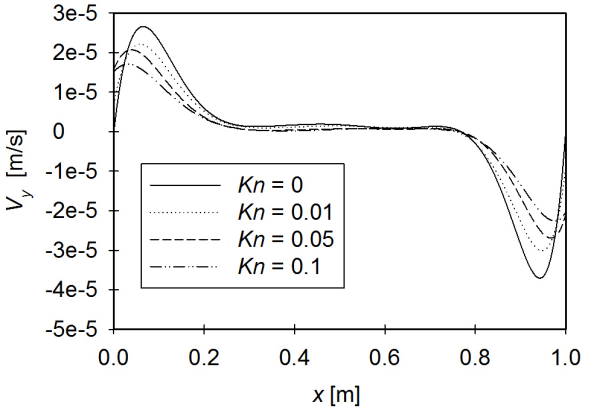

Fig. 9. *Variation of the vertical velocity (V_y) with the length of the cavity (L) for different Knudsen numbers, Ra = 10^5*

Fig. 10 demonstrates the temperature variations along the centreline of the cavity at $Ra = 10^6$ and different values of Knudsen numbers that cover the continuum and slip flow regimes. The graph shows that as the Knudsen number increases, the temperature jump at the hot wall increases.

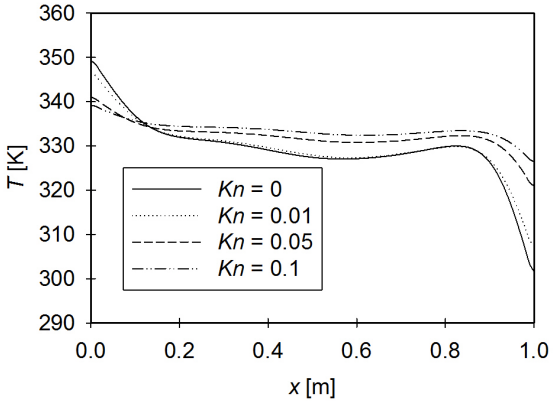

Fig. 10. *Variation of the temperature (T) with the length of the cavity (L) for different Knudsen numbers, Ra = 10^5*

Variations of the Nusselt number with Rayleigh number at different volume fractions and $Kn = 0.1$ are plotted in Fig. 11. The graph shows that the Nusselt number increases as the Rayleigh number increases for all values of the volume fractions considered in this study. Moreover, the graph shows that the Nusselt number increases as the volume fraction increases for the same value of the Rayleigh number. The graph also shows that when the Rayleigh number is below 10^4, the dominant mode of heat transfer is conduction. In addition, when $10^4 < Ra < 10^5$ then there is a combination of conduction and convection modes of heat transfer happening inside the cavity while for the range where Ra is greater than 10^5, the dominant mode of heat transfer is mainly convection.

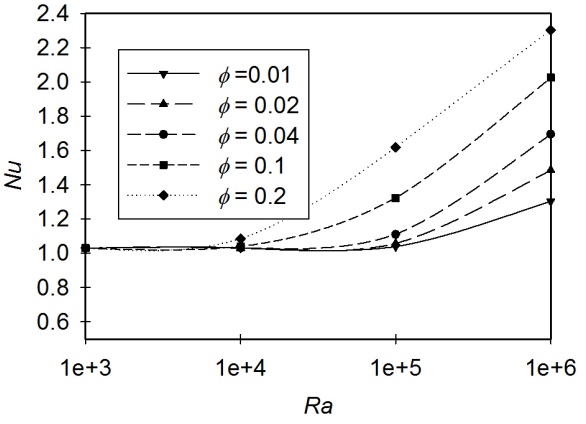

Fig. 11. *Variation of Nusselt number (Nu) with the Rayleigh number (Ra) at different ϕ, Kn = 0.1*

In Fig. 12, variations of the Nusselt number with the solid nanoparticles volume fraction (ϕ) for different values of the Knudsen number and $Ra = 10^6$ are plotted. The graph shows that as ϕ increases the Nusselt number increases for all values of the Knudsen number. For instance, and at $Kn = 0.05$, the graph shows that there is a percentage increase of 53 % in the Nusselt number for the case when $\phi = 0.2$ compared to $\phi = 0.01$. Moreover, the graph shows that as the Knudsen number increases the Nusselt number decreases. This can be justified due to the rarefaction effects.

Finally, a correlation for the Nusselt number among all the parameters taken into consideration in this study in the slip flow regime and $\phi \neq 0$ is proposed in the following equation with $R^2 = 0.87$:

$$Nu = 0.2196 Ra^{0.0829} Kn^{-0.511} \varphi^{0.104}. \quad (21)$$

It should be noted that the range of Rayleigh numbers used in the simulation is the reason for the weak dependency of Nusselt numbers on Rayleigh numbers. Rayleigh number range is from the conduction dominant heat transfer all the way to the transitional regime between the conduction and convection heat transfer.

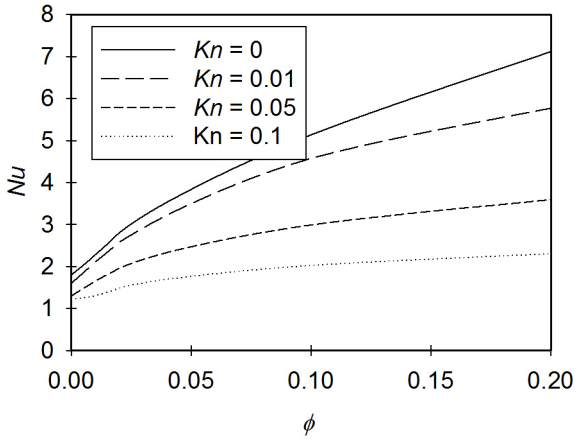

Fig. 12. *Variation of Nusselt number (Nu) with the volume fraction (ϕ) at different Kn*

Based on Eq. (21), one can plot many master curves to show the effects of the investigated parameters on the Nusselt number. For instance, Fig. 13 shows one master curve in which *Ra* is fixed to 10^6, and the Knudsen number and the nanoparticles volume fraction were varied. Many other similar curves can also be generated.

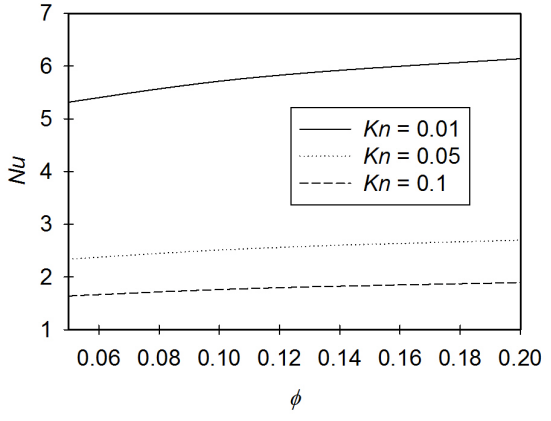

Fig. 13. *Variation of Nusselt number (Nu) with the volume fraction (ϕ) at different Kn for the case where Ra = 10^6 and based on Eq. (21)*

6 CONCLUSIONS

A steady, two-dimensional analysis of low-pressure gaseous laminar nanofluid flow inside a square cavity in which the hot surface is attached to two solid fins is carried out. This type of flow serves in many engineering applications such as those in nuclear reactors and electronic equipment cooling. Rarefaction, Rayleigh numbers, and the volume fraction of the nanoparticles effects on both flow and heat characteristics of such flows are investigated. Results show that as the Knudsen number increases, the slip velocity and the temperature jump at the boundaries will increase and the average Nusselt number decreases. Moreover, it is found that as the Rayleigh number increases, the Nusselt number increases. In addition, it is found for the investigated range of the nanoparticles volume fraction that as this fraction increases then the average Nusselt number increases. Finally, a correlation among the Nusselt number and the parameters investigated in this study is proposed.

7 NOMENCLATURE

A_c Cold wall area, [m^2]
A_h Hot wall area, [m^2]
A_F Fin area, [m^2]
A_T Area of the fin and the hot wall $A_T=A_h+A_F$, [m^2]
C_p Specific heat, [J kg^{-1} K^{-1}]
g Gravity acceleration in the x direction, [m·s^{-2}]
Gr Grashof number, [-]
h_1 Fin 1 Position, [m]
h_2 Fin 2 Position, [m]
h Convection heat transfer coefficient, [W m^{-2} K^{-1}]
k Thermal conductivity, [W m^{-1} K^{-1}]
Kn Knudsen number, [-]
k_f Fluid thermal conductivity, [W m^{-1} K^{-1}]
k_{nf} Nanofluid thermal conductivity, [W m^{-1} K^{-1}]
k_s Nano particles thermal conductivity, [W m^{-1} K^{-1}]
L Length of the square cavity, [m]
L_F Fin length, [m]
Nu Nusselt number, [-]
P Pressure, [Pa]
Q Heat transfer, [W]
q''_c Local heat flux at the wall of the cold surface, [W·m^{-2}]
q''_h Local heat flux at the wall of the hot surface, [W·m^{-2}]
q''_F Local heat flux at the fin, [W·m^{-2}]
R Universal gas constant, [J·mol^{-1}·K^{-1}]
Ra Rayleigh number, [-]
Re Reynolds number, [-]
Ri Richardson number (Gr/Re^2)
T Temperature, [°C]
T_c Temperature of the first cell from the wall, [°C]
T_i Hot surface temperature, [°C]
T_o Cold surface temperature, [°C]
u Velocity in x-direction, [m·s^{-1}]
u_c Tangential velocity of the first cell from the wall, [m·s^{-1}]
v Velocity in y-direction, [m·s^{-1}]
x, y Cartesian coordinates, [m]

Greek symbols

α Thermal diffusivity [$m^2 \cdot s^{-1}$]
β Thermal expansion coefficient, [K^{-1}]
γ Specific weight, [$N \cdot m^{-3}$]
λ Molecular mean free path, [m]
μ Dynamic viscosity, [kg m^{-1} s^{-1}]
v Kinematic viscosity, [$m^2 \cdot s^{-1}$]
ϕ Nano particles volume fraction, [%]
P Density of air, given by ideal gas equation (P/RT), [$kg \cdot m^{-3}$]
σ_T Thermal accommodation coefficient
σ_v Momentum accommodation coefficient

Subscripts

eff Effective
f Fluid
F Fin
g Gas flow
i Hot wall
n Normal
nf Nanofluid
o Cold wall
r Ratio
w wall

8 REFERENCES

[1] Chambre, A.P., Schaaf, S.A., (1961). *Flow of Rarefied Gases*, Princeton University Press Princeton, **DOI:10.1515/9781400885800**.

[2] Cercignani, C., Lampis, M. (1974). Half space models for gas-surface interaction. *Rarefied Gas Dynamics*, Academic Press, New York, p. 361-368, **DOI:10.1016/B978-0-12-398150-9.50040-7.**

[3] Bilgen, E. (2005). Natural convection in cavities with a thin fin on the hot wall. *International Journal of Heat and Mass Transfer*, vol. 48, no. 17, p. 3493-3505, **DOI:10.1016/j.ijheatmasstransfer.2005.03.016**.

[4] Alkhalidi, A., Kiwan, S., Al-Kouz, W., Alshare, A. (2016). Conjugate heat transfer in rarefied gas in enclosed cavities. *Vacuum*, vol. 130, p. 137-145, **DOI:10.1016/j.vacuum.2016.05.013**.

[5] Chahrazed, B., Samir, R. (2012). Simulation of heat transfer in a square cavity with two fins attached to the hot wall. *Energy Procedia*, vol. 18, p. 1299-1306, **DOI:10.1016/j.egypro.2012.05.147**.

[6] Al-Kouz, W., Kiwan, S., Alshare, A., Alkhalidi, A., Al-Muhtady, A., Saadeh, H. (2017). Two dimensional analysis of low-pressure flows in an inclined square cavity with two fins attached to the hot wall, in press, *International Journal of Thermal Sciences.*

[7] Öztop, H.F., Estellé, P., Yan, WM.., Al-Salem, K., Orfi, J., Mahian, O. (2015). A brief review of natural convection in enclosures under localized heating with and without nanofluids. *International Communications in Heat and Mass Transfer*, vol. 60, p. 37-44, **DOI:10.1016/j.icheatmasstransfer.2014.11.001**.

[8] Bigdeli, M.B., Fasano, M., Cardellini, A., Chiavazzo, E., Asinari, P. (2016). A review on the heat and mass transfer phenomena in nanofluid coolants with special focus on automotive applications. *Renewable and Sustainable Energy Reviews*, vol. 60, no. 1615-1633, **DOI:10.1016/j.rser.2016.03.027**.

[9] Akbari, M., Galanis, N., Behzadmehr, A. (2012). Comparative assessment of single and two-phase models for numerical studies of nanofluid turbulent forced convection. *International Journal of Heat and Fluid Flow*, vol. 37, p. 136-146, **DOI:10.1016/j.ijheatfluidflow.2012.05.005**.

[10] Balandin, A.A., Ghosh, S., Bao, W., Calizo, I., Teweldebrhan, D., Miao, F., Lau,C.N. (2008). Superior thermal conductivity of single-layer graphene. *Nano Letters*, vol. 8, no. 3, 902-907, **DOI:10.1021/nl0731872**.

[11] Kalteh, M., Abbassi, A., Saffar-Avval, M., Frijns, A., Darhuber, A., Harting, J. (2012). Experimental and numerical investigation of nanofluid forced convection inside a wide microchannel heat sink. *Applied Thermal Engineering*, vol. 36, p. 260-268, **DOI:10.1016/j.applthermaleng.2011.10.023**.

[12] Hussien, A.A., Abdullah, M.Z., Al-Nimr, M.A. (2016). Single-phase heat transfer enhancement in micro/minichannels using nanofluids: Theory and applications. *Applied Energy*, vol. 164, p. 733-755, **DOI:10.1016/j.apenergy.2015.11.099**.

[13] Wang, X.-Q., Mujumdar, A.S. (2007). Heat transfer characteristics of nanofluids: a review. *International Journal of Thermal Sciences*, vol. 46, no. 1, p. 1-19, **DOI:10.1016/j.ijthermalsci.2006.06.010.**

[14] Yu, W., France, D.M., Routbort, J.L., Choi, S.U.S. (2008). Review and comparison of nanofluid thermal conductivity and heat transfer enhancements. *Heat Transfer Engineering*, vol. 29, no. 5, p. 432-460, **DOI:10.1080/01457630701850851**.

[15] Sarkar, J., Ghosh, P., Adil, A. (2015). A review on hybrid nanofluids: Recent research, development and applications. *Renewable and Sustainable Energy Reviews*, vol. 43, p. 164-177, **DOI:10.1016/j.rser.2014.11.023**.

[16] Saidur, R., Leong, K.Y., Mohammad, H.A. (2011). A review on applications and challenges of nanofluids. *Renewable and Sustainable Energy Reviews*, vol. 15, no. 3, p. 1646-1668, **DOI:10.1016/j.rser.2010.11.035**.

[17] Suresh, S., Venkitaraj, K.P., Selvakumar, P., Chandrasekar, M. (2012). Effect of Al203–Cu/water hybrid nanofluid in heat transfer. *Experimental Thermal and Fluid Science*, vol. 38, p. 54-60, **DOI:10.1016/j.expthermflusci.2011.11.007**.

[18] Murshed, S.M.S., Estellé, P. (2017). A state of the art review on viscosity of nanofluids. *Renewable and Sustainable Energy Reviews*, vol. 76, p. 1134-1152, **DOI:10.1016/j.rser.2017.03.113**.

[19] Labib, M.N., Nine, Md.J., Afrianto, H., Chung, H., Jeong, H. (2013). Numerical investigation on effect of base fluids and hybrid nanofluid in forced convective heat transfer. *International Journal of Thermal Sciences*, vol. 71, p. 163-171, **DOI:10.1016/j.ijthermalsci.2013.04.003**.

[20] Heris, S.Z., Esfahany, M.N., Etemad, S.Gh. (2007). Experimental investigation of convective heat transfer of Al203/water nanofluid in circular tube. *International Journal of Heat and Fluid Flow*, vol. 28, no. 2, p. 203-210, **DOI:10.1016/j.ijheatfluidflow.2006.05.001**.

[21] Moghadassi, A., Ghomi, E., Parvizian, F. (2015). A numerical study of water based Al2O3 and Al2O3–Cu hybrid nanofluid effect on forced convective heat transfer. *International Journal of Thermal Sciences*, vol. 92, p. 50-57, **DOI:10.1016/j.ijthermalsci.2015.01.025**.

[22] Noie, S.H., Heris, S.Z., Kahani, M., Nowee, S.M. (2009). Heat transfer enhancement using Al2O3/water nanofluid in a two-phase closed thermosiphon. *International Journal of Heat and Fluid Flow*, vol. 30, no. 4, p. 700-705, **DOI:10.1016/j.ijheatfluidflow.2009.03.001**.

[23] Salman, B.H., Mohammed, H.A., Kherbeet, A.Sh. (2012). Heat transfer enhancement of nanofluids flow in microtube with constant heat flux. *International Communications in Heat and Mass Transfer*, vol. 39, no. 8, p. 1195-1204, **DOI:10.1016/j.icheatmasstransfer.2012.07.005**.

[24] Williams, W., Buongiorno, J., Hu, L.-W. (2008). Experimental investigation of turbulent convective heat transfer and pressure loss of alumina/water and zirconia/water nanoparticle colloids (nanofluids) in horizontal tubes. *Journal of Heat Transfer*, vol. 130, no. 4, p. 042214, **DOI:10.1115/1.2818775**.

[25] Taamneh, Y., Bataineh, K. (2017). Mixed convection heat transfer in a square lid-driven cavity filled with Al2O3-water nanofluid. *Strojniški vestnik - Journal of Mechanical Engineering*, vol. 63, no. 6, 383-393, **DOI:10.5545/sv-jme.2017.4449**.

[26] Cardellini, A., Fasano, M., Bigdeli, M.B., Chiavazzo, E., Asinari, P. (2016). Thermal transport phenomena in nanoparticle suspensions. *Journal of Physics: Condensed Matter*, vol. 28, no 48, p. 1-17, **DOI:10.1088/0953-8984/28/48/483003**.

[27] Brinkman, H.C. (1952). The viscosity of concentrated suspensions and solutions. *The Journal of Chemical Physics*, vol. 20, no. 4, p. 571-581, **DOI:10.1063/1.1700493**.

[28] Hatschek, E. (1913). The general theory of viscosity of two phase systems. *Transactions of the Faraday Society*, vol. 9, p. 80-92, **DOI:10.1039/TF9130900080**.

[29] Maxwell, J.C. (1873). *A Treatise on Electricity and Magnetism*, vol. 1. Clarendon Press, Oxford.

[30] Karniadakis, G., Beskok A., Aluru, N. (2005). *Microflows and Nanoflows*, Springer, New York.

[31] Lockerby, D.A., Reese, J.M., Emerson, D.R., Barber, R.W. (2004). Velocity boundary condition at solid wall in rarefied gas calculations. *Physical Review E*, vol. 70, no. 1, p. 017303, **DOI:10.1103/PhysRevE.70.017303**.

[32] Kandlikar, S., Garimella, S., Li, D., Colin, S., King, M. R. (2006). *Heat Transfer and Fluid Flow in Minichannels and microchannels: Single-Phase Gas Flow in Microchannels*, Elsevier Ltd.

[33] Versteeg, H.K., Malalasekera, W. (1995). *An Introduction to Computational Fluid Dynamics: The Finite Volume Method*, Prentice-Hall, Essex.

[34] Patankar, S.V., Spalding, D.B. (1972). A calculation procedure for heat, mass and momentum transfer in three-dimensional parabolic flows. *International Journal of Heat and Mass Transfer*, vo. 15, no. 10, p. 1787-1806, **DOI:10.1016/0017-9310(72)90054-3**.

[35] De Vahl Davis, G. , Jones, I.P. (1983). Natural convection in a square cavity: A comparison exercise. *International Journal of Numerical Methods in Fluids*, vol. 3, no. 3, p. 227-248, **DOI:10.1002/fld.1650030304**.

[36] De Vahl Davis, G. (1983). Natural convection of air in a square cavity: A bench mark numerical solution. *International Journal of Numerical Methods in Fluids*, vol. 3, no. 3, p. 249-264, **DOI:10.1002/fld.1650030305**.

[37] Sarkar, A., Nag, A., Sastri, V.M.K. (1993). Natural convection in a differentially heated square cavity with a horizontal partition plate on the hot wall. *Computer Methods in Applied Mechanics and Engineering*, vol. 110, no. 1-2, p. 143-156, **DOI:10.1016/0045-7825(93)90025-S**.

Strojniški vestnik - Journal of Mechanical Engineering 64(2018)1, 37-46

DOI:10.5545/sv-jme.2017.4790 Original Scientific Paper
Received for review: 2017-08-01
Received revised form: 2017-11-24
Accepted for publication: 2017-12-11

Analysis of the Bulk Coal Transport State of a Scraper Conveyor Using the Discrete Element Method

Xuewen Wang* – Bo Li – Zhaojian Yang
Taiyuan University of Technology, College of Mechanical Engineering,
Shanxi Key Laboratory of Fully Mechanized Coal Mining Equipment, China

A scraper conveyor is the main transport equipment in a coal mine, and its condition considerably influences the production capacity and profitability of the enterprise. In this study, the discrete element method (DEM) was used to study the interaction between the scraper conveyor and bulk coal. The particle size and velocity distributions of bulk coal were analysed at different transport velocities, transport angles, feed velocities and mining heights by changing the transport conditions of the conveyor. The influence of the transport velocity, coefficient of static friction between particles and mass flow rate were also studied. The results showed that the particle size distribution of bulk coal is mostly unrelated to the transport state parameters in the stable transport stage. Large particles gather at higher positions, whereas small particles gather at lower positions. The speed of bulk coal in the front area of the scraper was equal to the velocity of the scraper, whereas the coal in other locations had a lower speed. The mass flow rate of the bulk coal increased with increasing transport velocity and reached its peak when the coefficient of static friction between particles was 0.4.

Keywords: scraper conveyor, bulk coal, discrete element method, mass flow rate

Highlights

- *The discrete element model developed can simulate bulk coal- scraper conveyor interactions.*
- *The bulk coal size distribution had little relation with the transport state parameters at smooth transport stage.*
- *Big particles gathered at the upper position while the small ones at the lower position on the scraper conveyor.*
- *Bulk coal mass flow rate increased as the transport velocity increased.*
- *Bulk coal mass flow rate reached the peak when the static friction coefficient between particles was 0.4.*

0 INTRODUCTION

As the main transport equipment for fully mechanized coal caving, a scraper conveyor is not only the coal transport machine but also the moving pivot of the hydraulic support and the orbit of the shearers. The rationale behind the design of the scraper conveyor and its reliability directly affect the production efficiency of a fully mechanized coal mining system [1] and [2]. Current research on scraper conveyors mainly focuses on how to improve their power, capacity, life, safety and applicability in various working conditions. Significant attention has been paid to the structure and function of the scraper conveyor itself [3] to [6]. Few studies have focused on the material characteristics during the transport stage and the interaction between bulk coal and the scraper conveyor, and even fewer studies have provided a precise relationship between the transport of bulk coal and the running conditions of the scraper conveyor. This lack of research inevitably leads to deviations in safety, reliability and transport efficiency that affect the entire material transport process.

Three-dimensional optimization, simulation and dynamic design have become important techniques in modern mechanical design with the rapid development of computer technology and modern design methods [7] to [9]. Previous studies have mainly used finite element methods (FEMs) for the design and analysis of scraper conveyors. The bulk coal in the chute is represented using either a continuum model or directly added force on the chute, and then, the mechanics are established using the FEM. Optimization methods are applied after simulation and analysis using FEM [10] to [13]. A systems analysis, including mechanical analysis of the shearer and chute, was conducted by Chen et al. [14] to study the stress conditions of the chute; the maximum stress was obtained using ANSYS, a software package based on an FEM. Ren and Chen [15] studied the rack rail of a scraper conveyor using ANSYS, and their conclusions provided a theoretical basis for the optimal structural design of the rack rail.

Particles of granular matter interact with themselves and with the machine [16]; thus, it is difficult to obtain meaningful results using traditional continuum mechanics methods, such as FEM. Therefore, the discrete element method (DEM) was introduced to better study the internal and external interaction mechanics of materials and to obtain reliable results. The DEM is a numerical method that was proposed by Cundall and Strack [17] and Cundall [18] and is based on the principles of molecular dynamics. The method was first used

*Corr. Author's Address: Taiyuan University of Technology, College of Mechanical Engineering, Taiyuan, China, wxuew@163.com

to study complex problems, such as rock mechanics. A DEM is a collection of rigid elements, which is more in accordance with the properties of granular material than continuum theory. The method has been successfully applied in coal mining, geotechnical engineering, the chemical industry, agriculture and other fields [19] to [23]. There are many applications in bulk solids transportation. Lim et al. [24] simulated vertical and horizontal solid particle transport in a pneumatic conveyance using the DEM and computational fluid dynamics. The simulated and experimental results corresponded well with those reported previously. Zuo et al. [25] studied the dynamic characteristics of bulk materials (e.g., agricultural products) during the process of sudden braking using the DEM. The dynamic forces acting on the front wall of a truck by the bulk material under different conditions were studied, which provided new ideas for truck design. Katterfeld and Gröger [26] studied the loading and unloading process of a bucket elevator and scraper conveyor using the same method. Additionaly, Katterfeld et al. [27] developed an auxiliary design for a high-flow transfer station using the DEM and provided qualitative and quantitative verification of the numerical simulation. Simsek and Wirtz [28] studied the mixing process of a thin layer of particles on a vibrating conveyor and investigated the phenomena of particle flow and dispersion using the DEM. Hastie and Wypych [29] compared different methods, such as the continuous medium method, DEM and test experiments, to predict the particle flow phenomenon in the chute. Derakhshani et al. [30] used the DEM to study the mechanical behaviour between particles and the interaction between the belt conveyor and particles. The particle flow field was simulated using computational fluid dynamics, and the entrainment phenomenon was studied to help optimize the dust control system. The above research applied the DEM to the study of bulk materials; however, few studies have focused on the scraper conveyor.

The objectives of this study were as follows: (1) establish an interaction model between bulk coal and the scraper conveyor using the software EDEM; (2) study the particle size distribution and velocity of coal under different conditions, such as differences in transport velocity, transport angle, feed velocity and mining height; and (3) study the influences of the transport velocity and coefficient of static friction on the mass flow rate.

1 METHODOLOGY

1.1 Model Scraper Conveyor

The scraper conveyor mainly consists of a head, spill plate, chute, scraper, chain and tail (Fig. 1). The scraper conveyor model used in this study was a production model. Its design length was 200 m, the rated transport capacity was 416.7 kg/s, the speed of the scraper chain was 1.1 m/s and the scraper spacing was 1,008 mm.

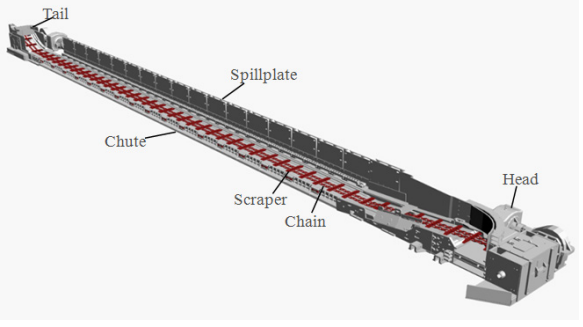

Fig. 1. *Structure of a scraper conveyor*

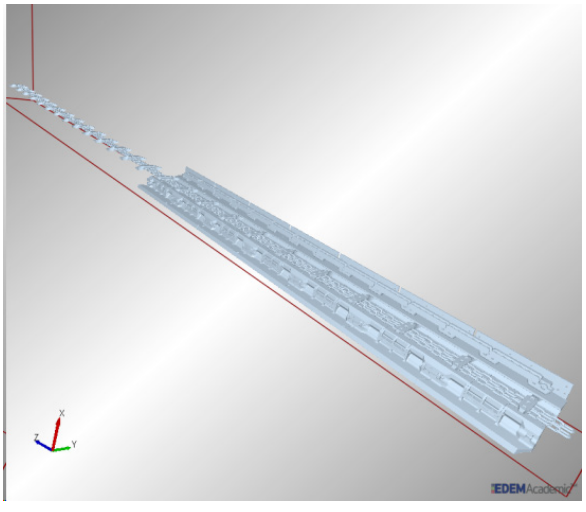

Fig. 2. *Model of the chute*

Table 1. *Material parameters of the chute* [31]

Material parameters	High manganese steel
Poisson's ratio	0.3
Shear modulus [Pa]	7×1010
Density [kg/m³]	7800

The modelling function of EDEM is relatively simple. Thus, it is difficult to satisfy the modelling requirements of a complex geometry, such as that of a scraper conveyor. Therefore, the three-dimensional

model was first established in NX7.5 UG software (Siemens PLM Software, Munich, Germany) and then imported into EDEM to perform the simulation. Because this study focused mainly on the transport state and related properties of the bulk coal, the scraper conveyor model was simplified by removing the head and tail, retaining only the chute; this also improved the speed of the calculations. The scraper chain and scraper were extended to ensure that a sufficient number of scrapers were in motion on the chute during the simulation.

Different file formats can be imported into EDEM. Here, the STEP format was chosen to ensure the integrity of the data, the model, the product life cycle and other aspects due to the complex geometry of the scraper conveyor. The established model and the material parameters of the chute are shown in Fig. 2 and Table 1, respectively.

1.2 Model Bulk Coal

Two main types of contact were applied in this model, namely, the contact between coal particles and the contact between coal and the chute. Coal particle breakage and deformation occurs under actual conditions, and numerous particle collisions will occur simultaneously. A soft ball model was selected as the mechanical model in this study to accurately reflect these actual conditions.

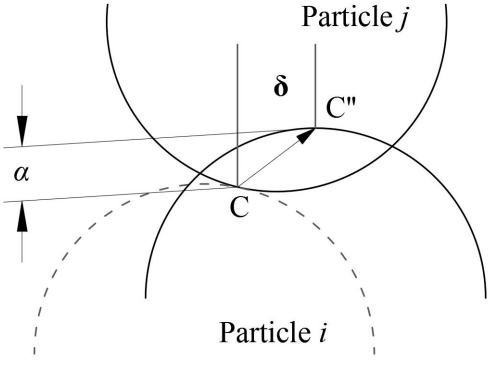

Fig. 3. *Model of two contact soft balls*

As shown in Fig. 3, particle *i* comes into contact with particle *j* at point C under external forces or inertia. The dotted line indicates the original position of particle *i*. With the relative motion of the two particles, the surfaces of the particles gradually deform and the contact force increases. However, details of the deformation were not considered in the soft sphere model, and the contact force was obtained based on the normal overlap α and tangential displacement $\boldsymbol{\delta}$.

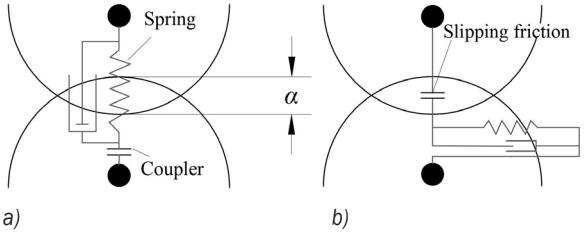

Fig. 4. *Simplified model of contact force between particles: a) normal force, and b) tangential force*

The soft ball model consisted of a spring, damper, slider and coupler between two particles. A coupler was used to determine the particle pairing relationship of two particles in contact. If the tangential force exceeds the yield value, the two particles will slide under the effects of the normal force and friction in the tangential direction. The elastic coefficient *k*, the damping coefficient *c* and other parameters were introduced to quantify the effect of the spring, damper and slider (Fig. 4).

The normal force $\mathbf{F}_{nij}$ was the resultant of the elastic and damping forces acting on particle *i*, as shown in Figs. 3 and 4. According to Hertz contact theory, $\mathbf{F}_{nij}$ is expressed as follows:

$$\mathbf{F}_{nij} = \left(-k_n \alpha^{2/3} - c_n \mathbf{v}_{ij} \cdot \mathbf{n}\right)\mathbf{n}. \tag{1}$$

The tangential force F_{tij} is expressed as:

$$\mathbf{F}_{tij} = -k_t \boldsymbol{\delta} - c_t \mathbf{v}_{ct}, \tag{2}$$

where k_t is the tangential elastic coefficient, c_t is the tangential damping coefficient, $\mathbf{v}_{ct}$ is the slip velocity at the contact point, and $\boldsymbol{\delta}$ is the tangential displacement at the contact point.

Particle generation is critical in the simulation process and greatly affects the simulation results. Bulk coal differs from other bulk materials that have rather homogenous particle shapes, such as chemical fertilizers or grains, because of the uncertainty in the shapes cut by the shearer. It is difficult to define the true shape of coal particles in 3D modelling software, and there is no representative shape. Therefore, to simplify the calculation and represent the actual situation as closely as possible, a multiple round surface filling method was used in EDEM to build the bulk coal model. A model of a standard coal particle was constructed using four combined spheres (Fig. 5); the model was 95.11 mm long, 85.59 mm wide and 80.05 mm high. Particles with three different diameters were used to study the size distribution of bulk coal; the dimensions were 0.5, 1 and 1.3 times that of the standard particle size. Particles with different sizes were generated randomly by a particle

factory to ensure that the bulk coal fell into the chute in a mixing state. The properties of bulk coal are provided in Table 2 [31].

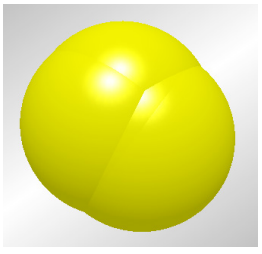

Fig. 5. *Bulk coal model*

The weight of the standard coal particle that was modelled was 0.56 kg, the volume was 3.53×10^{-4} m^3 and the moment of inertia relative to X, Y, and Z axes was 4.01×10^{-4} kgm^2, 4.48×10^{-4} kgm^2 and 4.65×10^{-4} kgm^2, respectively

Table 2. *Property of bulk coal* [32]

Particle material properties	coal
Poisson's ratio	0.25
Shear modulus [Pa]	1×107
Density [kg/m^3]	1600

1.3 Contact and Transport Model

Based on analysis of the mechanical model and actual working conditions, the Hertz-Mindlin no slip contact model was used in this study; the contact parameters of this model are provided in Table 3 [32].

Table 3. *Contact parameters* [32]

Elastic restitution coefficient between bulk coal particles	0.5
Static friction coefficient between bulk coal particles	0.6
Dynamic friction coefficient between bulk coal particles	0.05
Elastic restitution coefficient between bulk coal and the chute	0.5
Static friction coefficient between bulk coal and the chute	0.4
Dynamic friction coefficient between bulk coal and the chute	0.05

This study focused on the motion characteristics of bulk coal in the chute; thus, the simulation included the cutting of bulk coal by the shearer, coal falling into the chute and transport of the coal by the scraper conveyor. Based on actual production, the particle factory was set at the original position in the upper part of the scraper and parallel to the bottom of the chute. The process of the shearer cutting coal was simulated by the particle factory producing bulk coal; the mining height was 2.6 m, 5 m, or 5.5 m based on the position of the actual shearer. The particle factory was rectangular in shape, with a length of 2.5 m along the chute and a width of 0.755 m.

1.4 Simulation Parameters

The stable state was established as the reference state, and the parameters were changed when studying the scraper conveyor under different working conditions. The main simulation parameters in this study were the transport angle, transport velocity, feed velocity and mining height. The main parameters of the stable state are provided in Table 4.

Table 4. *Main parameters of the stable state*

Transport state parameters	Stable
Transport angle [°]	0
Transport velocity [m/s]	1.1
Feed velocity [m/s]	3.44
Mining height [m]	5.5

The parameters of the stable state were based on the relevant parameters of an actual scraper conveyor and shearer (Table 5). The transport velocity was the rated speed of the scraper conveyor, and the feed velocity was converted from the rated rotational speed of the shearer. The initial velocity of the bulk coal was set based on the rated rotational speed of the shearer.

Table 5. *Related parameters of the electric haulage shearer*

Mining height range [m]	2.6 to 5.5
Drum diameter [mm]	2,500
Drum rotation speed [m/s]	3.44

In this study, the fixed time step in EDEM was set as 8.59×10^{-5} s, which was 10 % of the Rayleigh time step, and the total simulation time was 15 s. The grid size in the simulation area was adjusted according to the related preprocessing parameters. To obtain accurate results while retaining a high simulation efficiency, the number of grid units was set close to but less than 1×10^5. Therefore, the grid size was set to 6.89 times of the particles' minimum radius, and the simulation area was divided into 92,565 grid units.

Bulk coal was generated dynamically from t = 0 s to t = 15 s with a fixed particle size. Aside from gravity, an initial velocity was added to coal particles to simulate the initial speed of coal brought about by the rotating shearer. The direction of the initial particle velocity was set at a 45° downward slope. Particle factories simulated the generation of coal

cut by the shearers. To ensure that the same number of particles were created for the three different sizes, the speed at which particles were generated by the three factories was calculated based on the ratios of the dimensions of the different particles. The speed at which the particle factories generated particles was set according to the rated transport capacity of an actual scraper conveyor, which was 416.7 kg/s in this study. The particle generation speeds of the three particle factories are provided in Table 6.

Table 6. *Particle generation speed of each particle factory*

Particle factory	Generation speed [kg/s]
0.5 times the standard particle size	15.65
1 times the standard particle size	125.23
1.3 times the standard particle size	275.12

1.5 Working State Simulation

The stable state is the normal and stable working condition of a scraper conveyor when transporting bulk coal. For a given type of coal, the controllable factors affecting the transport state include the transport angle, transport velocity, feed velocity and mining height. There are fewer uncontrollable factors in the stable state, and different transport states were simulated. The simulated results were then compared with those in the stable state to study the transport state under different working conditions.

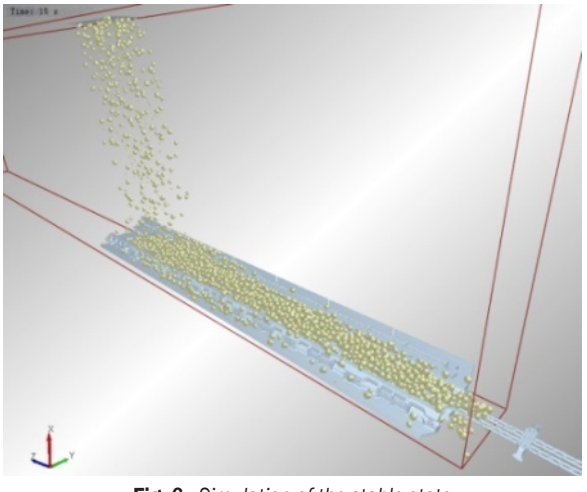

Fig. 6. *Simulation of the stable state*

The simulation begins with the particle factory generating particles. Then, the bulk coal falls into the chute and is transported from one side of the scraper to the other (Fig. 6). The interaction model was established based on the model of the chute (Fig. 2) and the bulk coal (Fig. 5). The entire simulation lasted for 15 s.

When studying the transport state under different velocities, the running direction of the scraper and the chain was constrained to be parallel to the bottom of the chute. In the actual situation, the velocity of the chain was changed in a micro wave because of rotation of the sprocket. For the limitation of the software and the purpose of simplifying the simulation, the scraper and scraper chain were set in the uniform linear motion during the entire simulation. Then, the bulk coal was pushed to move by the scraper. The transport velocities are shown in Table 7.

Table 7. *Transport velocities*

Stable state [m/s]	1.1
Speed 1 [m/s]	0.8
Speed 2 [m/s]	0.5

To study the transport state with different transport angles, the angle was adjusted by changing the direction of gravity because the angle of the scraper conveyor could not be adjusted directly. The gravitational direction was set by adjusting the values of its components in the X, Y, and Z directions.

In the stable state, the direction of gravity was perpendicular to the chute. The other two angles were set at the limiting angles of the scraper conveyor: inclined upward 25° and inclined downward 20°. The direction of gravity is shown in Table 8.

Table 8. *Parameters of gravity under different transport angle conditions*

Transport angle	Direction vector
0°	(-9.809, 0, -0.13987)
Inclined upward 25°	(-8.9491, 0, 4.0187)
Inclined downward 20°	(-9.1696, 0, -3.4863)

Table 9. *Different feed velocities*

Velocity [m/s]	Coordinate
3.44	(-2.435, 0, -2.435)
2.12	(-1.5, 0, -1.5)
1.41	(-1, 0, -1)

To study the influence of feed velocity on the transport state, the magnitude of the initial particle velocity was changed while leaving its direction of motion unchanged. The components of the initial velocity in the X, Y, and Z directions are provided in Table 9. The three particle factories maintained the same initial particle velocity. The initial velocity of

the stable state was 3.44 m/s and was set to 2.12 m/s and 1.41 m/s in the other two states.

In the study of different mining heights, the position of the particle factory needed to be adjusted. The mining height was 5.5 m in the stable state and 5 m and 2.6 m in the other two states (Table 10).

Table 10. *Different mining heights*

Stable state [m]	5.5
Height 1 [m]	5
Height 2 [m]	2.6

1.6 Factors Influencing the Mass Flow Rate

Transport capacity is an important parameter in the design of a scraper conveyor and directly determines the quality of the scraper conveyor. Although the mass flow rate refers to the mass flow per unit time, the value can directly reflect the transport capacity of the scraper conveyor as well. Thus, research on the mass flow rate is critical for improving the transportation capacity of a scraper conveyor, optimizing its structure and reducing unnecessary energy dissipation. The model for calculating the transport capacity in actual production is shown in Fig. 7, which was screenshot of the scraper conveyor during transportation. Assuming that the coal on the scraper conveyor will not spill out, the cross section of the coal can be divided into several sections. The percentages shown in Fig. 7 are the ratios of coal transport speed to the chain speed. The coal speed is closer to the chain speed as the coal getting closer to the chain.

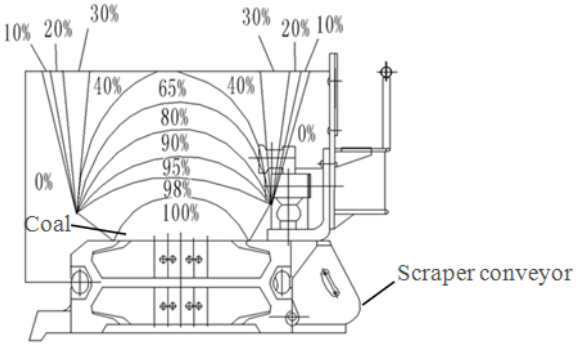

Fig. 7. *Model for calculating capacity*

The equation for computing the transport capacity is given by:

$$Q = 3.6 \times 10^6 \times \left(\sum A_n i_n \right) v_n \rho, \tag{3}$$

where Q is the transport capacity of the scraper conveyor per hour [kg/h], A_n is the cross-sectional area of cargo [m²], i_n is the relative velocity of the cargo section, v_n is the running velocity of the scraper chain [m/s], and ρ is the bulk coal density [kg/m³].

The mass flow rate through a specified section during the simulation is detected by a sensor in EDEM. Single-factor analysis was applied to study the influence of velocity and the coefficient of static friction on the mass flow rate. When studying the influence of transport velocity on the mass flow rate, the scraper conveyor was confirmed to be working in the stable state. The coefficient of static friction was maintained at 0.6, and the scraper conveyor was adjusted to work under transport velocities of (0.2, 0.5, 0.8, 1.1, 1.4 and 1.7) m/s. The mass flow rate was always detected at the same position.

In analysing the influence of the coefficient of static friction between particles on the mass flow rate, the velocity was kept constant, and the coefficient was set at 0, 0.2, 0.4, 0.6 and 0.8. Then, the mass flow rate was determined.

2 RESULTS AND DISCUSSION

2.1 Analysis of the Particle Size Distribution

Bulk coal particles with three diameters were generated to analyse the effects of the particle size distribution. In the simulation, the particles were coloured blue, green and red in order of increasing size (Fig. 8).

The four groups (a, b, c and d) in Fig. 8 correspond to the particle size distributions with different transport velocities, transport angles, feed velocities, and mining heights. The bulk coal was more stable when the scraper conveyor had a lower velocity (Fig. 8a). However, lower velocities affected the production efficiency. The bulk coal becomes unstable as the chute angle is decreased from being inclined upward 25° to being inclined downward 20° (Fig. 8b). The feed velocity did not have a considerable effect on the fluctuation of particles in the chute (Fig. 8c). The bulk coal was more stable when the mining height was low (Fig. 8d). Large particles (red) were concentrated on top, whereas small particles (blue) spread out on the bottom. Middle-sized particles were located in the middle section. Therefore, the bulk coal size distribution with large particles on top and small particles at the bottom was not related to the transport velocity, transport angle, feed velocity, or mining height.

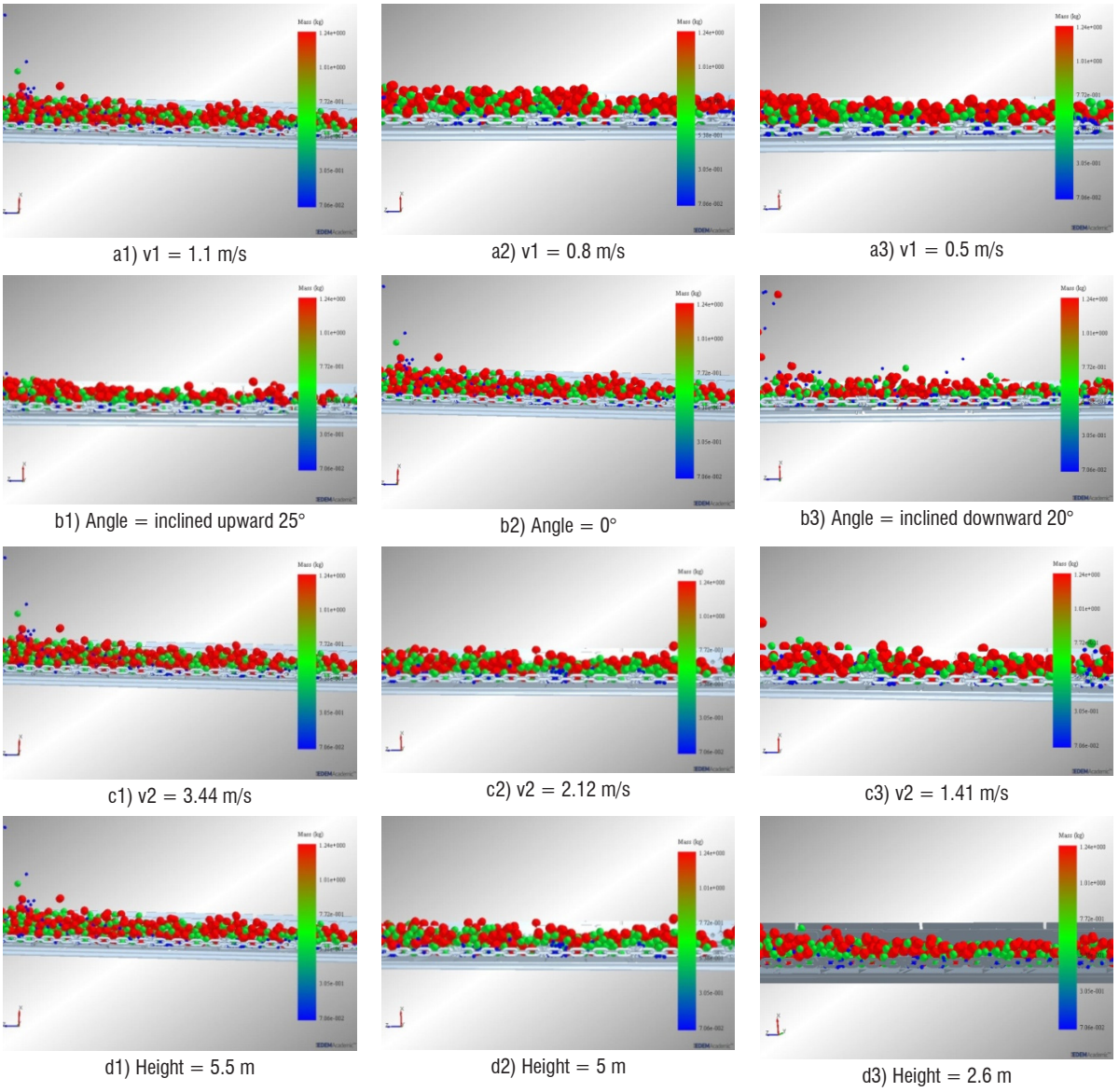

Fig. 8. *Sections showing the particle size distribution under different conditions; a) a1 to a3 different transport velocities; b) different transport angles, c) different feed velocities, and d) different mining heights*

2.2 Velocity Distribution Analysis

The bulk coal can be displayed in different colours according to the velocity of particles in EDEM. Particles were coloured in order of blue, green and red with increasing velocity (Fig. 9).

The particles in the chute had a lower velocity than particles falling down from the particle factory (Fig. 5). All particles in the chute were blue, within which it was difficult to distinguish the velocity distribution. Thus, the colours of particles in the chute had to be redefined.

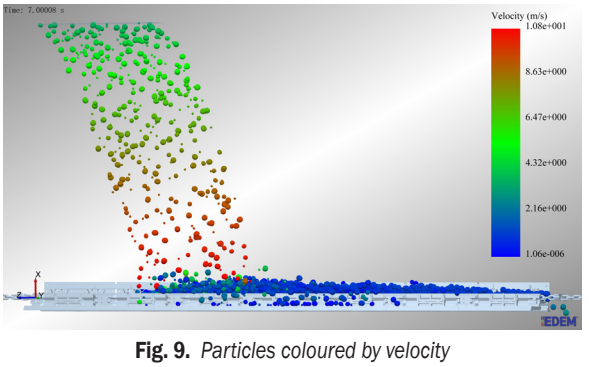

Fig. 9. *Particles coloured by velocity (colouring range divided automatically)*

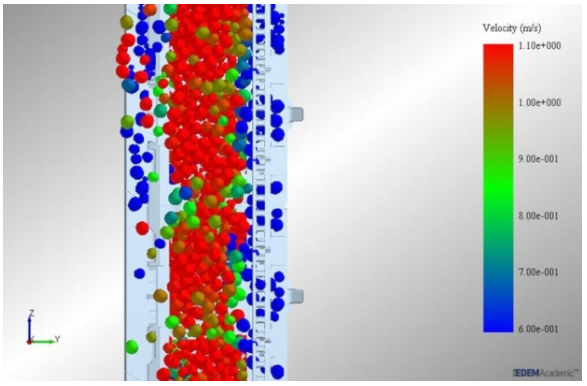

Fig. 10. *Distribution of particle velocities (colouring range: 0 m/s to 1.1 m/s)*

Under the attribute colouring label, the minimum and maximum values were set as 0 m/s and 1.1 m/s, respectively. Then, the colouring range was 0 m/s to 1.1 m/s. The particle velocity distribution within the chute is shown in Fig. 10.

The majority of the bulk coal in the middle of the chute had a high velocity, whereas lower velocity particles were distributed on both sides of the chute (Fig. 7).

The range over which velocities were coloured was large, and nearly all of the particles in the chute were red. Thus, it was still difficult to identify the particle velocity distribution. The range of colours was adjusted such that the minimum and maximum values were set at 1.09 m/s and 1.1 m/s, respectively. Longitudinal sections of the particle velocity distribution along the chute were obtained at different positions.

There were differences near the bottom of the chute in that particles close to the scraper had higher velocities than particles farther from the scraper (Figs. 11a and 11b). Instead of a continuous distribution, the particle velocities exhibited regional concentrations (Fig. 11c). Particles in front of the scraper had the same velocity as the scraper, whereas particles in other locations had lower velocities.

2.3 Analysis of the Factors Influencing the Mass Flow Rate

2.3.1 Effect of Velocity on the Mass Flow Rate

The mass flow rate increased linearly with the transport velocity, with an R^2 value of 0.975, meaning that a higher velocity led to a greater capacity (Fig. 12). However, in actual production, the velocity cannot increase without bound. The power provided by the motor is limited, and equipment wear, energy consumption and noise greatly increase with increases in the transport velocity. Furthermore, the required amount of scraper conveyor material also increases. These factors would greatly increase production costs, which is not conducive to actual production. The speed of the chain typically ranges from 0.6 m/s to 1.4 m/s.

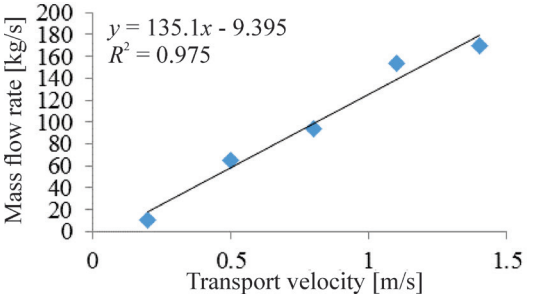

Fig. 12. *Mass flow rate under different transport velocities*

Therefore, a reasonable transport velocity that will improve the transport capacity and reduce costs as much as possible must be established to achieve the maximum economic benefit. The velocity is also affected by underground operating conditions, the capacity of the scraper conveyor, production requirements and many other conditions, which

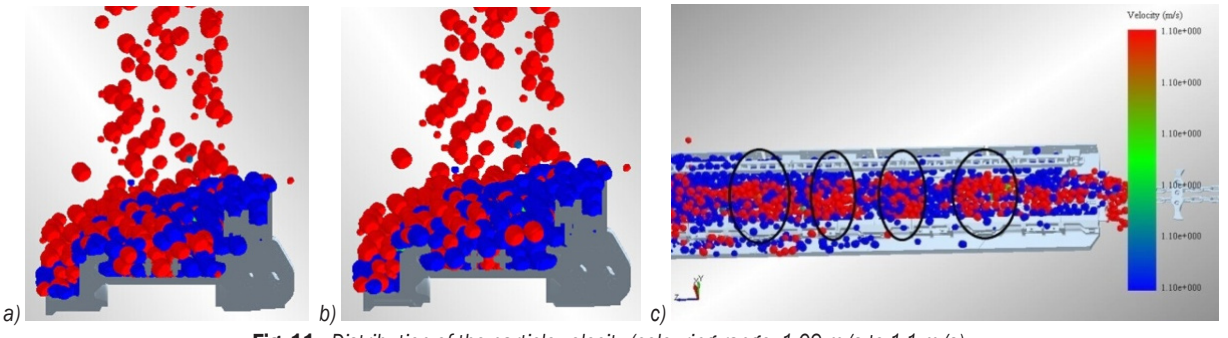

Fig. 11. *Distribution of the particle velocity (colouring range: 1.09 m/s to 1.1 m/s); a) longitudinal section close to the scraper, b) longitudinal section between two scrapers, and c) velocity concentration*

should be analysed based on the actual situation. Such an investigation may provide the relationship between the transport velocities and mass flow rate.

2.3.2 Effect of the Coefficient of Static Friction on the Mass Flow Rate

The relationship between the mass flow rate and the coefficient of static friction was fit using a quadratic function (Fig. 13). The mass flow rate increased to a peak (157.21 kg/s) as the coefficient of static friction between the particles increased from 0 to 0.4; then, the mass flow rate decreased as the coefficient of static friction increased to 0.8. The scraper conveyor achieved its maximum capacity when the coefficient of static friction between particles was 0.4. Coal particles in the middle and upper part were driven by the static friction from particles at the bottom. If the coefficient of static friction is too small, the static friction would be too small to drive all the particles in the upper part. That's the reason the mass flow rate would increase as the coefficient of static friction increased from 0 to 0.4. When the static friction is higher than 0.4, coal particles in the upper part would bear more resistance from coal particles around. The particles stayed at the middle and upper part would roll, which seemed moving backwards compared with the particles pushed by the scraper at the bottom. Therefore, the mass flow rate would decrease when the static friction is higher than 0.4.

In actual practice, static friction between particles, which is determined by the type of coal, cannot be controlled. However, research in this area could provide a basis for predicting coal output depending on the type of coal in a certain mine.

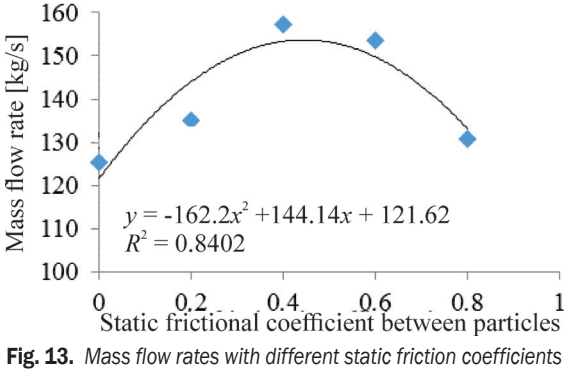

Fig. 13. *Mass flow rates with different static friction coefficients*

3 CONCLUSIONS

The DEM can overcome the deficiencies of the FEM in studying the motions and forces of particles such as bulk coal to provide a more reliable theoretical basis for the research and design of scraper conveyors. The following conclusions were drawn:

1) An interaction model that can simulate the working process of the scraper conveyor was built using EDEM. The operating parameters under different conditions were obtained, which are difficult to acquire experimentally.
2) The particle size distribution was not related to the transport velocity, transport angle, feed velocity, or mining height in the stable state. Large particles were distributed on the top of the scraper, and small particles were distributed at the bottom. With regard to the particle velocity distribution, particles close to the scraper had a high velocity at the bottom, whereas particles at other positions had a lower velocity. The particle velocity distribution in the chute exhibited regional variations, i.e., particles in front of the scraper had the same velocity as the scraper, whereas particles in other regions had lower velocities.
3) There was a quadratic relationship between the mass flow rate and the coefficient of static friction. The mass flow rate reached its peak when the coefficient of static friction was 0.4.

4 ACKNOWLEDGEMENTS

This project was supported by the merit funding for the returned overseas personnel sci-tech activities, Shanxi Province, China (2016), Program for the Outstanding Innovative Teams of Higher Learning Institutions of Shanxi (2014), the Basic Condition Platform Project of Shanxi (2014091016) and the Open Research Fund of Shanxi Key Laboratory of Fully Mechanized Coal Mining Equipment (2015-02).

5 REFERENCES

[1] Lodewijks, G. (2002). Two decades dynamics of belt conveyor systems. *Bulk Solids Handing*, vol. 22, p. 124-132.

[2] Li, G. (2003). Belt conveyor dynamic behavior and associated problems. *Bulk Solids Handing*, vol. 23, p. 322-327.

[3] Broadfoot, A.R., Betz, R.E. (1997). Prediction of power requirements for a long wall armored face conveyor. *IEEE Transaction on Industry Applications*, vol. 33, no. 1, p. 80-89, **DOI:10.1109/28.567081**.

[4] Morley, L.A., Kohler, J.L., Smolnikar, H.M. (1988). A model for prediction motor load for an armored face conveyor drive. *IEEE Transaction on Industry Applications*, vol. 24, no. 4, p. 649-659, **DOI:10.1109/28.6117**.

[5] Lodewijks, G. (2004). Strategies for automated maintenance of belt conveyor systems. *Bulk Solids Handling*, vol. 1, p. 16-22.

[6] Xi, P.-Y., Zhang, H.-T., Liu, J. (2005). Dynamics simulation of the belt conveyor possessing feedback loop during starting. *Journal of Coal Science & Engineering*, vol. 11, p. 83-85.

[7] Thomas, H., Zhou, M.,Schramm, U. (2002). Issues of commercial optimization software development. *Structural Multidisciplinary Optimization*, vol. 23, no. 2, p. 97-110, **DOI:10.1007/s00158-002-0170-x**.

[8] Feriani, A., Perotti, F., Simoncini, V. (2000). Iterative system solvers for the frequency analysis of linear mechanical systems. *Computer Methods in Applied Mechanics and Engineering*, vol. 190, no. 13-14, p. 1719-1739, **DOI:10.1016/S0045-7825(00)00187-0**.

[9] Xue, S.-S., Li, X.-C., Xu, X.-Y. (2016). Fault tree and Bayesian network based scraper conveyer fault diagnosis. *Proceedings of the 22nd International Conference on Industrial Engineering and Engineering Management*, p. 783-795, **DOI:10.2991/978-94-6239-180-2_74**.

[10] Korneev, S.V. (2003). Evaluation of efficiency of controlling the speed of face scraper conveyer. *Izvestiya Vysshikh Uchebnykh Zavedenii, Gornyi Zhurnal, (News of the Higher Institutions. Mining Journal)*, vol. 5, p. 66-71. (in Russian)

[11] Bulin, R., Hajzman, M. (2014). On the modelling of contact forces in the framework of rigid body dynamics. *Manufacturing Technology*, vol. 14, no. 2, p. 136-141.

[12] Slavković, R., Veg, A., Dučić, N., Slavković, N., Baralić, J., Milićević, I. (2015). Rigid body dynamics in optimization of the machine tool vibroisolation. *Tehnicki vjesnik – Technical Gazette*, vol. 22, no. 1, p. 87-94, **DOI:10.17559/TV-20130918225023**.

[13] Vasylieva, O.E., Kuzio, I.V. (2014). Optimization of structural elements of drive gearbox shafts of mine scraper conveyors. *Naukovyi Visnyk Natsionalnoho Hirnychoho Universytetu, (Scientific Bulletin of National Mining University)*, no. 3, p. 37-45. (in Russian)

[14] Chen, X. Z., Meng, Y., Liu, D.Y., Fan, X. (2012). Analysis on central trough of scraper conveyor by FEM. *Coal Mine Machinery*, vol. 33, p. 110-112. (in Chinese)

[15] Ren, Z.Q., Chen, J.L. (2013). FEA of scraper conveyer rack rail based on ANSYS. *Coal Mine Machinery*, vol. 34, p. 99-100. (in Chinese)

[16] Xiao, F.J., Guo, L.J., Li, D.B., Wang, Y.S. (2012). Discrete particle simulation of mixed sand transport. *Particuology*, vol. 10, no. 2, p. 221-228, **DOI:10.1016/j.partic.2011.10.004**.

[17] Cundall, P.A., Strack, O.D.L. (1979). A discrete numerical model for granular assemblies. *Géotechnique*, vol. 29, no. 1, p. 47-65, **DOI:10.1680/geot.1979.29.1.47**.

[18] Cundall, P.A. (1971). A computer model for simulating progressive large scale movements in blocky systems. *Proceedings of the Symposium of the International Society of Rock Mechanics*, vol. 2, no. 8.

[19] Landry, H., Laguë, C., Roberge, M. (2006). Discrete element modeling of machine-manure interactions. *Computers and Electronics in Agriculture*, vol. 52, no. 1-2, p. 90-106, **DOI:10.1016/j.compag.2006.02.002**.

[20] Marigo, M., Cairns, D.L., Davies, M., Ingram, A., Stitt, E.H. (2011). Developing mechanistic understanding of granular behaviour in complex moving geometry using the discrete element method: Part B: Investigation of flow and mixing in the turbula (R) mixer. *Powder Technology*, vol. 212, no. 1, p. 17-24, **DOI:10.1016/j.powtec.2011.04.009**.

[21] Morrison, R.D., Cleary, P.W., Sinnott, M.D. (2009). Using DEM to compare the energy efficiency of pilot scale ball and tower mills. *Minerals Engineering*, vol. 22, no. 7-8, p. 665-672, **DOI:10.1016/j.mineng.2009.01.016**.

[22] Hasan, A., Karrech, A., Chareyre, B. (2017). Evaluating force distributions within virtual uncemented mine backfill using discrete element method. *International Journal of Geomechanics*, vol. 17, no. 7, **DOI:10.1061/(ASCE)GM.1943-5622.0000850**.

[23] Nandanwar, M., Chen, Y. (2015). *Simulation of Triaxial Compression Test for Sandy Loam Soil Using PFC3D*, MSc. Thesis, University of Manitoba, Manitoba.

[24] Lim, E.W.C., Wang, C.H., Yu, A.B. (2006). Discrete element simulation for pneumatic conveying of granular material, *AIChE Journal*, vol. 52, no. 2, p. 496-509, **DOI:10.1002/aic.10645**.

[25] Zuo, S.C., Xu, Y., Yang, Q., Feng, Y.T. (2006). Discrete element simulation of the behavior of bulk granular material during truck braking. *Engineering Computations*, vol. 23, no. 1, p. 4-15, **DOI:10.1108/02644400610638943**.

[26] Katterfeld, A., Gröger, T. (2007). Application of the discrete element method - Part 4: Bucket elevators and scraper conveyors. *Bulk Solids Handling*, vol. 27, p. 228-234.

[27] Katterfeld, A., Gröger, T., Minkin, A. (2007). Discrete element simulation of transfer stations and their verification, *9th International Conference on Bulk Materials Storage, Handling and Transportation*, Newcastle, p. 379-385.

[28] Simsek, E., Wirtz, S., Scherer, V., Kruggel-Emden, H., Grochowski, R., Walzel, P. (2008). An experimental and numerical study of transversal dispersion of granular material on a vibrating conveyor. *Particulate Science and Technology*, vol. 26, no. 2, p. 177-196, **DOI:10.1080/02726350801903772**.

[29] Hastie, D.B., Wypych, P.W. (2010). Experimental validation of particle flow through conveyor transfer hoods via continuum and discrete element methods. *Mechanics of Materials*, vol. 42, no. 4, p. 383-394, **DOI:10.1016/j.mechmat.2009.11.007**.

[30] Derakhshani, S.M., Schott, D.L., Lodewijks, G. (2013). Modeling dust liberation at the belt conveyor transfer point with CFD and DEM coupling method. *11th International Conference on Bulk Materials Storage*, Handling and Transportation, Newcastle.

[31] Yuan, J.M., Yao, H.L., Hu, Z.H., Zhou, J. (2016). The new discharge hopper and EDEM simulation analysis for particles flat accumulation after free falling. *International Conference on Advanced Electronic Science and Technology*, p. 993-998, **DOI:10.2991/aest-16.2016.132**.

[32] Mei, L., Hu, J.Q., Yang, J.G., Yuan, J.M. (2016). Research on parameters of EDEM simulations based on the angle of repose experiment. *IEEE International Conference on Computer Supported Cooperative Work in Design*. p. 570-574, **DOI:10.1109/CSCWD.2016.7566053**.

Strojniški vestnik - Journal of Mechanical Engineering 64(2018)1, 47-55

DOI:10.5545/sv-jme.2017.4786
Original Scientific Paper
Received for review: 2017-08-03
Received revised form: 2017-11-20
Accepted for publication: 2017-11-22

Nonlinear Control of a Flexible Joint Robotic Manipulator with Experimental Validation

Waqar Alam[1] – Adeel Mehmood[1] – Khurram Ali[1] – Usman Javaid[1] – Soltan Alharbi[2] – Jamshed Iqbal[2,3,*]
[1] COMSATS Institute of Information Technology, Department of Electrical Engineering, Pakistan
[2] University of Jeddah, Electrical and Computer Engineering Department, Saudi Arabia
[3] FAST National University of Computer and Emerging Sciences, Department of Electrical Engineering, Pakistan

This article addresses the design and implementation of robust nonlinear control approaches to obtain the desired trajectory tracking of a flexible joint manipulator driven with a direct-current (DC) geared motor. The nonlinear control schemes have been designed and implemented such that they locally stabilize the closed loop system considering all the states as bounded. The system model has been derived using Euler-Lagrange approach. Two different approaches based on sliding mode control (SMC), i.e. the traditional SMC and integral SMC, have been considered in the present study. To experimentally validate the proposed control laws, an electrically-driven single-link flexible manipulator has been designed and fabricated. The designed control algorithms have been developed and experimentally validated on the custom-developed platform. The results obtained both from MATLAB/Simulink and the experimental platform verify the performance of the proposed control algorithms.

Keywords: flexible joint manipulator; modern control system; sliding mode control; integral sliding mode control

Highlights

- *This research presents two approaches to control joint flexibility of a manipulator by considering actuator dynamics.*
- *A mathematical model of the system is derived using Euler-Lagrange algorithm.*
- *Control laws based on SMC and ISMC have been designed to track the desired trajectory.*
- *Based on a custom-developed hardware platform, experimental results are obtained in LabVIEW using NI MyRio-1900.*
- *The obtained results validate the performance of the designed control laws.*

0 INTRODUCTION

The domain of robotics has recently drawn significant attention in the scientific community **[1]**. In industrial applications, trajectory tracking control **[2]** of flexible joint manipulators has received considerable attention in the last two decades. An accurate end effector's position through reliable control approaches is critical for high-performance robotic applications accomplishing dangerous and tedious jobs **[3]**. Thus, a robotic manipulator is designed so as to increase stiffness in order to reduce undesirable oscillations of the end effector to track desired positions. The stiffness can be achieved by using heavy materials, which may increase power consumption and decrease the speed of operation **[4]**. The basic approach to maximize operational speed and minimize power consumption is to use lightweight, flexible joint manipulators; however, this is subject to improving performance in endpoint tracking.

In **[5]**, it is emphasized, that joint flexibility and actuator dynamics should be considered while modelling as well as designing an appropriate control law so as to achieve high performance. The literature focused on the design of controllers for flexible joint manipulators is extensive. However, incorporating actuator dynamics in the modern control of the end effector's position of a flexible joint manipulator remains a challenging issue in the robotics community **[6]**. Some methodologies are reported to control the manipulator without taking into account the dynamics of the actuator. Examples include feedback linearization method **[7]**, the singular perturbation approach **[8]**, the integral manifold control **[9]**, the passivity approach **[10]**, the proportional derivative (PD) control approach **[7]** and the adaptive sliding mode technique **[11]**. The major limitation of the above-mentioned research works is that these schemes assumed torque to be an input to the rigid link. However, it is highlighted in **[4]** that the actuator dynamics are of great importance in electro-mechanical systems, especially in a case in which a system has to deal with varying loads. Ailon and Lozano **[12]** proposed an iterative control law to regulate the set-point of a flexible robotic system that is driven electrically and is subjected to model uncertainty. Another study reported **[13]** presents a controller based on adaptation law for a flexible joint robot to improve the trajectory tracking in the presence of time-variable uncertainty in the system's parameters. A traditional back-stepping approach has been applied successfully to solve the control problem of robots with flexible joints **[14]** to **[16]**. However, in these approaching, the torque is assumed

*Corr. Author's Address: Electrical and Computer Engineering Department, College of Engineering, University of Jeddah, Kingdom of Saudi Arabia, jmiqbal@uj.edu.sa

to be directly applied to the links of the robot. In [16], a robust control law based on a back-stepping technique for tracking trajectory of manipulators has been proposed, in which only armature current and link position are measured for feedback purposes. Despite these efforts [14] to [16], most of the reported back-stepping techniques suffer from two limitations; The first is that the systems under consideration did not have time-varying parametric uncertainties. The second limitation is related to the level of complexity resulting from iterative differentiations of nonlinear virtual functions and thus leading to a complex and computationally expensive algorithm.

In the present article, the problem of robust control law design for accurate trajectory tracking of a flexible joint manipulator is addressed by considering actuator dynamics, joint flexibility, and viscous friction. Owing to computational simplicity and ease of implementation, the nonlinear law has been realized on custom-developed hardware. The control input (i.e. output of the controller) is fed to the plant (i.e. the direct-current (DC) motor and the flexible joint).

1 MATHEMATICAL MODELLING

To derive the mathematical model of the system, the considered parameters and their values are listed in Table 1.

Table 1. *Description of system parameters*

S#	Parameter	Symbol	Value	Unit
1	Link mass	m	1	kg
2	Gears ratio	N	1	-
3	Armature resistance	R	1.6	Ω
4	Joint stiffness	k	14	N·m/rad
5	Motor torque constant	kt	0.2	N·m/A
6	Back EMF constant	B	0.001	N·m·s/rad
7	Link length	d	0.5	M
8	Gravitational acceleration	g	10	m/s²
9	Link moment of inertia	J1	1	kg·m²
10	Motor shaft inertia	J2	0.3	kg·m²
11	Armature inductance	L	0.01	H

The flexibility in joint is modelled as a linear torsional spring [16]. Using Euler Lagrange equation, the equations of motion for an electro-mechanical system can be derived. The total kinetic energy (PE) can be written as Eqs. (1) and (2):

$$KE = \frac{1}{2}J_1\dot{q}_1^2 + \frac{1}{2}J_2\dot{q}_2^2, \tag{1}$$

$$PE = mgd\left(1-\cos q_1\right) + \frac{1}{2}k\left(q_1 - q_2\right)^2, \tag{2}$$

where q_1 and q_2 are angular positions of the link and the motor shaft respectively, while J_1 and J_2 are coefficients corresponding to link and motor inertia respectively. The Lagrange equation is:

$$L = KE - PE. \tag{3}$$

Using Eqs. (1) and (2), Eq. (3) can be written as:

$$L = \frac{1}{2}J_1\dot{q}_1 + \frac{1}{2}J_2\dot{q}_2 - mgd\left(1-\cos q_1\right) + \frac{1}{2}k\left(q_1 - q_2\right)^2. \tag{4}$$

Lagrangian equations of motion with respect to motor and link angular position can be written as:

$$\frac{d}{dt}\frac{\partial L}{\partial \dot{q}_2} - \frac{\partial L}{\partial q_1} = 0, \tag{5}$$

$$\frac{d}{dt}\frac{\partial L}{\partial \dot{q}_2} - \frac{\partial L}{\partial q_2} = \tau - B\dot{q}_2, \tag{6}$$

while the torque produced is:

$$\tau = k_t I, \tag{7}$$

where is the armature current. Now taking derivatives of Eqs. (5) and (6):

$$\frac{\partial L}{\partial \dot{q}_1} = J_1\dot{q}_1, \quad \frac{\partial L}{\partial \dot{q}_2} = J_2\dot{q}_2, \tag{8}$$

$$\frac{d}{dt}\frac{\partial L}{\partial \dot{q}_1} = J_1\ddot{q}_1, \quad \frac{d}{dt}\frac{\partial L}{\partial \dot{q}_2} = J_2\ddot{q}_2. \tag{9}$$

$$\frac{\partial L}{\partial q_1} = -Mgd\left(1-\sin\left(q_1\right)\right) - k\left(q_1 - q_2\right),$$

$$\frac{\partial L}{\partial q_1} = k(q_1 - q_2). \tag{10}$$

Equations of motion for the mechanical subsystem are given as:

$$J_1\ddot{q}_1 + mgd\sin\left(q_1\right) + k\left(q_1 - q_2\right), \tag{11}$$

$$J_2\ddot{q}_2 - k\left(q_1 - q_2\right) = \tau - B\dot{q}_2 \tag{12}$$

The flexible joint manipulator consists of a DC gear motor whose equation is derived by applying Kirchhoff's voltage law (KVL):

$$V = V_R + V_L + e, \tag{13}$$

where V_R is the voltage across resistor, V_L is the voltage across inductor and e is back electro motive force (emf) given by:

$$e = K_b\dot{q}_2, \tag{14}$$

where K_b is back emf constant. In this system, the input voltage to the DC motor is the excitation input given as:

$$v = u = RI + L\frac{di}{dt} + K_b\dot{q}_2, \tag{15}$$

where u is the motor input voltage. The nonlinear dynamics of the system can be formulated as:

$$J_1\ddot{q}_1 + mgd\sin(q_1) + k(q_1 - q_2), \tag{16}$$

$$J_2\ddot{q}_2 - k(q_1 - q_2) + B\dot{q}_2 = k_t I. \tag{17}$$

Assumption 1: The parameters mentioned in Eq. (17) can be expressed as $R(.)=R_0+\Delta R(t)$, $L(.)=L_0+\Delta L(t)$, and $K_b(.)=K_{b0}+\Delta K_b(t)$.

Assumption 2: The parameters mentioned in Eq. (16) can be expressed as $J_2(.)=J_{20}+\Delta J_2(t)$, $B(.)=B_0+\Delta B(t)$, and $K_t(.)=K_{t0}+\Delta K_t(t)$.

Remarks: In these realistic assumptions, the system parameters are split into a known nominal value and the unknown part, which is considered to be uncertain. In practical control systems, parameters may not be unknown completely, their nominal values are precisely known to us; this is taken into consideration in this research.

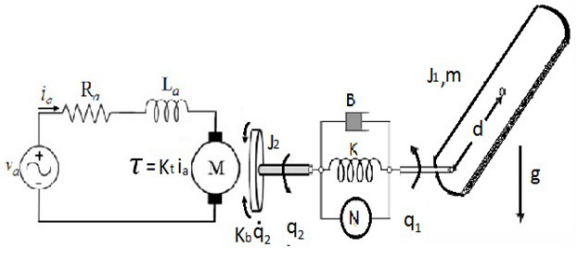

Fig. 1. *Schematic diagram of flexible joint manipulator*

The equations of the motion of an electrically driven flexible joint manipulator in state space form are represented below. The state vector contains an angular position and angular velocity of the link side, angular position and angular velocity on the motor side, and the motor armature current, i.e. $[x_1, x_2, x_3, x_4, x_5] = [q_1, \dot{q}_1, q_2, \dot{q}_2, I]$.

$$\dot{x} = f(x) + g(x)u, \quad x \in R^5, \tag{18}$$

$$\dot{x}_1 = x_2, \quad \dot{x}_2 = -a\sin(x_1) - b(x_1 - x_3),$$

$$\dot{x}_3 = x_4, \quad \dot{x}_4 = O(x_1 - x_3) - \frac{B}{J_2}x_4 + dx_5,$$

$$\dot{x}_5 = -\frac{R}{L}x_5 - \frac{k_b}{L}x_4 + \frac{1}{L}u, \tag{19}$$

where $O=(k/J_2)$, $b=(k/J_1)$, $a=(mgd/J_1)$ and $d=(k/J_2)$. Here, the angular position of the link is considered to be an output. The system equations are complex and exhibit highly nonlinear dynamics thereby highlighting the challenge involved in the controller design.

2 CONTROLLER DESIGN

The control objective is to accurately control the position of a flexible joint in finite time by control laws. The proposed control laws are based on two robust nonlinear control techniques: sliding mode control (SMC) and integral SMC.

2.1 Sliding Mode Control Technique

SMC is a robust nonlinear control scheme, with a powerful capability to reject disturbances and plant uncertainties. This control scheme works on the principle of continuously altering the configuration of the controller to keep the state variables on the sliding manifold. Due to this phenomenon, undesirable chattering occurs. In mechanical parts, this produces high wear, while in electric parts, it may cause high heat losses [17]. In SMC, the controller comprises two phases [18]; one is used to force the system trajectory to achieve a sliding manifold, while second one is used to drive the states on the sliding manifold toward desired equilibrium point. Consider a linear system given in Eq. (20).

$$\dot{\xi} = A\xi + Bu, \tag{20}$$

where A and B represent coefficients of the system and ξ is the state vector. The sliding manifold for this system can be selected as:

$$S = c^T\xi, \tag{21}$$

where c is the sliding mode control design parameters matrix. Differentiating Eq. (21), we obtain:

$$\dot{S} = c^T\xi = c^T(A\xi + Bu). \tag{22}$$

Since, $\dot{S} = 0$ during sliding mode:

$$\dot{S} = c^T(A\xi + Bu) = 0. \tag{23}$$

In SMC, the control law u is a combination of two types of control given by:

$$u = u_{eq} + u_{dis}, \tag{24}$$

where u_{eq} is the equivalent controller used to control the system states during the sliding phase. Eq. (22) is solved to obtain the equivalent control given by:

$$u_{eq} = (c^T B)^{-1}(c^T A\xi), \tag{25}$$

while u_{dis} represents the switching controller that ensures the system stability.

$$u_{dis} = -k_1 signS - k_2 S, \tag{26}$$

where $k_1 > 0$ and $k_2 > 0$ are the design parameters and:

$$sign(S) = \begin{cases} 1 \; for \; S > 0 \\ -1 \; for \; S < 0 \end{cases}.$$

Substituting Eqs. (25) and (26) in Eq. (24):

$$u = \left(-k_1 sign\, S - k_2 S - \left(c^T A\xi\right)\right)\left(c^T B\right)^{-1}. \tag{27}$$

This is the control law u which is required for driving the system's initial states to equilibrium point in a finite time. The proposed control method is now applied to a flexible joint manipulator. The sliding surface selected for the system is:

$$S = (\frac{d}{dt} + c)^{n-1} e, \tag{28}$$

where $e = x_1 - x_d$ is the error between the actual and desired outputs. n is the relative degree of the system, c is a constant known as design parameter, i.e. $c > 0$.

$$S = \left(\frac{d}{dt} + c\right)^2 \left(\frac{d}{dt} + c\right)^2 e. \tag{29}$$

After expanding Eq. (29):

$$S = \ddot{e} + 4\dddot{e}c + 6\ddot{e}c^2 + 4\dot{e}c^3 + \dot{e}c^4. \tag{30}$$

Taking derivative of error variables, we obtain:

$$e = x_1 - x_d, \quad \dot{e} = x_2 - \dot{x}_d, \quad \ddot{e} = \dot{x}_2 - \ddot{x}_d,$$
$$\ddot{e} = -acos(x_1)\dot{x}_2 + a(x_2)^2 sin(x_1) - bx_2 + b(\dot{O}(x_1 - x_3) - (B/J_2)x_4 + dx_5) + bf_1 + \dddot{x}_d.$$

For the sake of brevity, a symbol W is defined as:

$$W = c^4 x_2 + 4c^3 \dot{x}_2 + 6c^2 \ddot{x}_2 + 4c\left(-a\cos(x_1)\dot{x}_2 + ax_2^2 s\sin(x_1) + ab\sin(x_1) + b^2(x_1 - x_3) + bO(x_1 - x_3) - \frac{bB}{J_2}x_4 + bdx_5\right) - a\cos(x_1)\ddot{x}_2 + ax_2\dot{x}_2\sin(x_1) + 2ax_2\dot{x}_2\sin(x_1) + ax_2^3\cos(x_1) + abx_2\cos(x_1) + b^2(x_2 - x_4) + bO(x_2 - x_4) - \left(\frac{Bb}{J_2}\right)\left(O(x_1 - x_3)\right) - x_4\frac{B}{J_2} + dx_5) + bd\left(\left(\frac{-R}{L}\right)x_5 - \frac{k_b}{L}x_4\right) - c^4\dot{x}_d - 4c^3\ddot{x}_d + 6c^2\dddot{x}_d - 4c\ddddot{x}_d - \ddddot{x}_d.$$

Substituting and taking derivative of S,

$$\dot{S} = W + bd\frac{1}{\mathrm{L}}u. \tag{31}$$

The control law u thus obtained is:

$$u = \left(\frac{L}{bd}\right)\left(-W - k_1 sign(S) - k_2 S\right). \tag{32}$$

The designed control law, when subjected to a system for tracking purpose, resulted in undesirable chattering in the control input. For stability analysis, the Lyapunov function is defined as in Eq. (33) with its time derivative given in Eq. (34).

$$V = \frac{1}{2}s^2, \tag{33}$$

$$\dot{V} = s\dot{s}. \tag{34}$$

Substituting Eq. (31) in Eq. (34), we obtain:

$$\dot{V} = S\left\{W + bd(1/L)u\right\}. \tag{35}$$

Putting values in Eq. (35):

$$\dot{V} = -k_1|S| - k_2|S|^2. \tag{36}$$

Eq. (36) indicates that the derivative of the Lyapunov function is definite, which means that the system is asymptotically stable as long as both k_1 and $k_2 > 0$. The steady-state error can be calculated by taking Laplace transform of Eq. (30).

$$E(s) = \frac{s^3 + 4cs^2 + 6c^2 s + 4c^3}{s^4 + 4cs^3 + 6c^2 s^2 + 4sc^3 + c^4},$$

where the inverse Laplace transform is:

$$e(t) = e(0)\left\{e^{ct} + \frac{c^2 t^2 e^{-ct}}{2} + \frac{c^3 t^3 e^{-ct}}{6} + cte^{-ct}\right\}. \tag{37}$$

The designed control input drives the steady-state error $e(t)$ to the sliding surface $S = 0$ asymptotically i.e. $\lim_{t\to\infty} e(t) = 0$ with convergence rate given by Eq. (37) and remains there subject to positive gains of the controller [19].

2.2 Integral Sliding Mode Control Technique

To overcome the major drawbacks encountered in conventional SMC approach, the integral term can be included in SMC. The main idea behind ISMC is high-frequency switching gain, which is designed to force the state to achieve the integral sliding surface. Then, the integral action in the sliding manifold drives the states to the desired equilibrium point. It is an efficient control technique used to overcome several problems encountered in the SMC approach such as high-frequency chattering effect and its insensitivity property. It mitigates chattering and improves the robustness and accuracy of the control system while guaranteeing the nominal control performance. The

dynamics of a flexible joint manipulator is explained in Eq. (19). The sliding manifold selected for the system is:

$$s = \int e\left(c + \frac{d}{dt}\right)^n, \tag{38}$$

where $e = x_1 - x_d$ is the error between the actual and desired outputs. n is the relative degree of the system, c is a constant known as design parameter, i.e. $c > 0$. After expanding, we take,

$$s = \int ec^5 + 5c^4 e + 10c^3 \dot{e}. \tag{39}$$

Taking the derivative of error variables:

$$\begin{aligned} &e = x_1 - x_d, \quad \dot{e} = x_2 - \dot{x}_d, \quad \ddot{e} = \dot{x}_2 - \ddot{x}_d, \\ &\dddot{e} = -acos(x_1)\dot{x}_1 - b\dot{x}_1 + b\dot{x}_3 - \dddot{x}_d, \\ &\ddddot{e} = -acos(x_1)\dot{x}_2 + ax_2^2 \sin(x_1) - b\dot{x}_2 + \\ &\quad + b(O(x_1 - x_3) - (B/J_2)x_4 + dx_5) + bf_1 + \ddddot{x}_d. \end{aligned}$$

For the sake of brevity, defining a symbol Q, i.e.

$$\begin{aligned} Q = {} & c^5 e + 5c^4 \dot{e} + 10C^3 \left(\dot{x}_2 - \ddot{x}_d\right) + \\ & 10c^2 \left(-a\cos\left(x_1\right)x_2 - bx_2 + bx_4 - \dddot{x}_d\right) + \\ & 5c\left(-a\cos\left(x_1\right)\dot{x}_2 + ax_2^2 \sin\left(x_1\right) - b\dot{x}_2 + b\dot{x}_4 - \ddddot{x}_d\right) - \\ & a\cos\left(x_1\right)\ddot{x}_2 + ax_2\dot{x}_2 \sin\left(x_1\right) + 2ax_2\dot{x}_2 \sin\left(x_1\right) + \\ & ax_2^3 \cos\left(x_1\right) - b\ddot{x}_2 + bO\left(x_2 - x_4\right) - \\ & \frac{bB}{J_2}\left(O\left(x_1 - x_3\right) - \frac{B}{J_2}x_4 + dx_5\right) + \\ & bd\left(\frac{-R}{L}x_5 - \frac{k_b}{L}x_4\right) - \ddddot{x}_d \pi r^2. \end{aligned}$$

Putting the values and taking derivative of sliding surface, we obtain:

$$\dot{s} = Q + \frac{bd}{L}u. \tag{40}$$

The control law u thus obtained is:

$$u = \frac{L}{bd}\left(-Q - k_1 sign\left(s\right) - k_2 s\right). \tag{41}$$

For stability analysis, the Lyapunov function is given by:

$$V = \frac{1}{2}s^2. \tag{42}$$

Taking time derivative of Eq. (42),

$$\dot{V} = s\dot{s}. \tag{43}$$

Substituting Eq. (40),

$$\dot{V} = s\left\{Q + \frac{bd}{L}u\right\}. \tag{44}$$

After putting values,

$$\dot{V} = -k_1 |s| - k_2 s^2. \tag{45}$$

ISMC ensures asymptotic stability in finite time. The steady state-error between the desired and the actual trajectory is calculated by considering the integral sliding manifold as:

$$S = \int c^5 e + 5c^4 e + \dddot{e} + 5c\ddot{e} + 10c^2 \ddot{e} + 10c^3 \dot{e}.$$

Assuming the condition $S = 0$ and by taking the Laplace transform,

$$E(s) = \left\{\frac{10c^3 s + 10c^2 s^2 + 5cs^3 + s^4}{c^5 + 5c^4 s + 10c^3 s^2 + 10c^2 s^3 + 5cs^4 + s^5}\right\}.$$

Now taking inverse Laplace transform,

$$e(t) = e(0)e^{-ct}\left\{1 + \frac{c^2 t^2}{2} + \frac{c^3 t^3}{6} - \frac{c^4 t^4}{6} + ct\right\}\pi r^2. \tag{46}$$

Eq. (46) indicates the steady-state error with its convergence rate, which means that it approaches to zero in finite time, i.e. $\lim_{t \to \infty} e(t) = 0$.

3 SIMULATION AND EXPERIMENTAL RESULTS

The performance and effectiveness of the designed controllers for desired tracking performance of flexible joint manipulators are verified through results gathered from simulations carried out in MATLAB/Simulink and the custom-developed platform. The setup is a single-link flexible joint manipulator shown in Fig. 2.

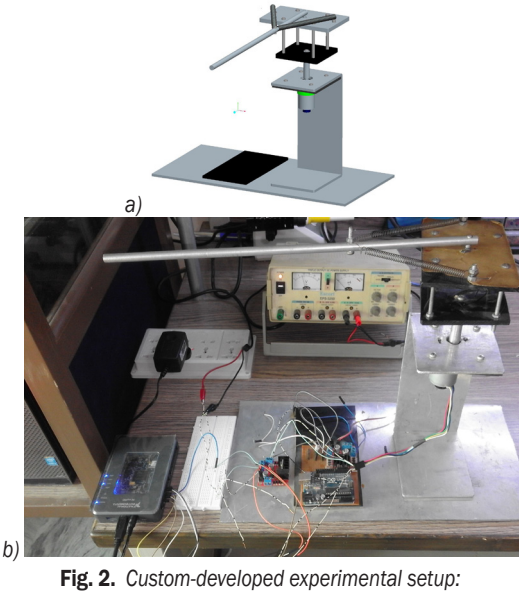

Fig. 2. *Custom-developed experimental setup: a) CAD model b) fabricated prototype*

The joint consists of an aluminium sheet tilted in such a way that a link is connected to a motor shaft through the sheet by two torsional springs. The actuator is a 24V DC gear motor, actuated with pulse width modulated (PWM) signal, which converts the control effort into an amplified voltage using an H-Bridge L298 and MyRio-1900 controller kit. The DC gear motor drives the aluminium plate directly. Two quadrature encoders provide feedback of the angular positions corresponding to the motor and the link. The rotary encoder is attached to the flexible joint so as to provide the joint position independently of the motor's position. Real-time control implementation is carried out in LabVIEW connected with external hardware using a MyRio-1900 data acquisition device. Two types of trajectories are tested for tracking purposes: step and sinusoidal. Simulation and experimental results corresponding to both types of input are presented and discussed below.

3.1 Step Tracking Using SMC and ISMC Laws

In this case, the desired trajectory is a constant value function. It has been observed that SMC produces undesirable chattering phenomena in control input, which can make the system unstable at any time. The designed control law, when subjected to the system for tracking purposes, practically affects system's mechanical and electric parts. This adverse phenomenon can be eliminated using ISMC.

Fig. 3 presents simulation results in which the designed control law is tracking a unit step function of 60° amplitude. The angular position shown in the figure is basically the position of the flexible joint. As evident from the results, the response of ISMC is better than SMC in terms of the steady-state error. However, the transient response of SMC shows good compliance with reference to the input.

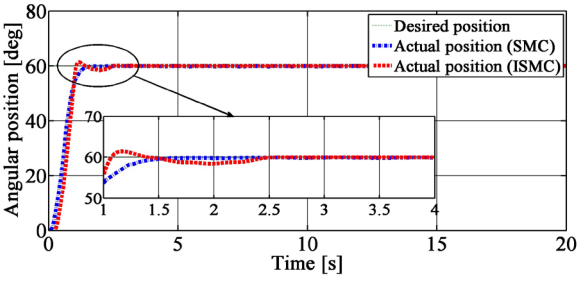

Fig. 3. *Responses of step tracking in simulation by control laws based on SMC and ISMC*

Fig. 4 shows the control input applied to the system in simulation. The results clearly show that the control input has undesirable chattering phenomenon in case of SMC, which can be harmful to the electrical and mechanical parts of the system.

Fig. 5 presents the results obtained from the experimental platform for tracking performance of the flexible joint manipulator using the SMC approach. The control input used for tracking purposes is also shown in the form of the percentage of the pulse-width modulation (PWM) signal applied to the motor. The results clearly show that with the SMC approach, a flexible joint manipulator can reasonably track the desired trajectory, however, at the expense of undesirable chattering in the control input.

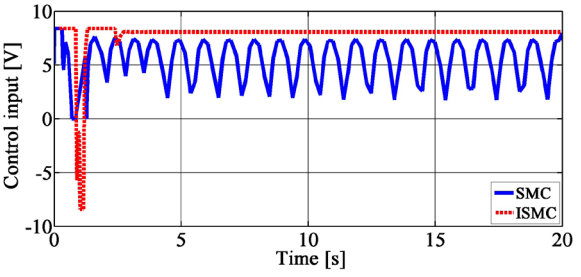

Fig. 4. *Simulation results for the control input applied to SMC and ISMC (Step references)*

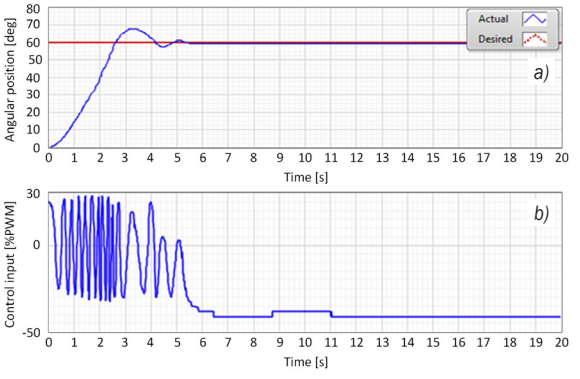

Fig. 5. *Experimental results of a) trajectory tracking and b) the control effort using SMC*

Fig. 6 shows the tracking error between actual trajectory and desired trajectory in case of SMC. The control law drives the steady-state error to zero within 5 seconds.

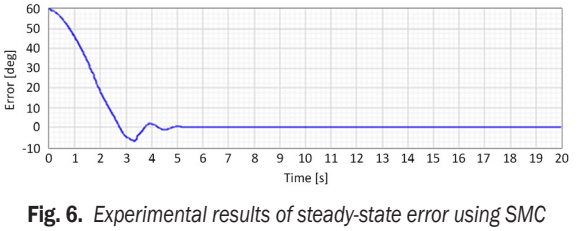

Fig. 6. *Experimental results of steady-state error using SMC*

Fig. 7 shows experimental results of the ISMC-based law in which the tracking performance of flexible joint manipulator and the control input are presented. The results clearly show that when using an ISMC approach, the manipulator tracked the desired trajectory with reasonable transient as well as steady state performance.

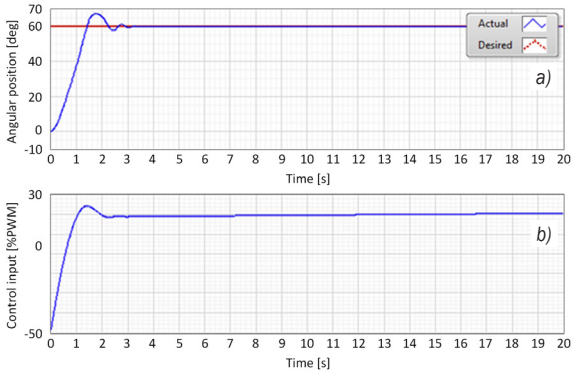

Fig. 7. *Experimental results of the a) trajectory tracking and b) the control effort using ISMC*

Fig. 8 shows trajectory tracking error between the actual and the desired positions, which is very small in comparison to SMC (see Fig. 6).

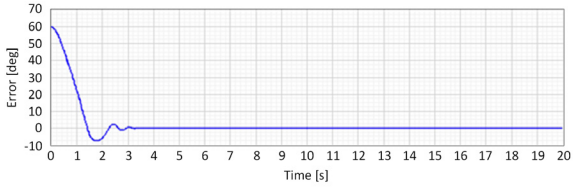

Fig. 8. *Experimental results of steady-state error using ISMC*

3.2 Sinusoidal Input Tracking using SMC and ISMC

In this case, the desired trajectory is a time-dependent sinusoidal function. The amplitude of the desired trajectory is taken as 60° with the frequency set to as low as 0.0048 Hz for smooth tracking. In case of ISMC, results collected both from the simulation and the experimental platform reflect that chattering is reduced due to the continuous control action while preserving the robustness and accuracy of the controller to a high degree. This observation is consistent with the theoretical advantage of ISMC over the traditional SMC approach.

Fig. 9 presents simulation results in which the sinusoidal signal representing the angular position of the flexible joint manipulator serves as the reference for trajectory tracking. The results demonstrate that both the control laws exhibit good settling time and zero steady-state error.

Fig. 10 shows the simulated control input used to drive the flexible joint manipulator in order to track the desired trajectory. As is evident from the figure, in the case of SMC, the control input has undesirable chattering phenomena, which is an inherent property of SMC.

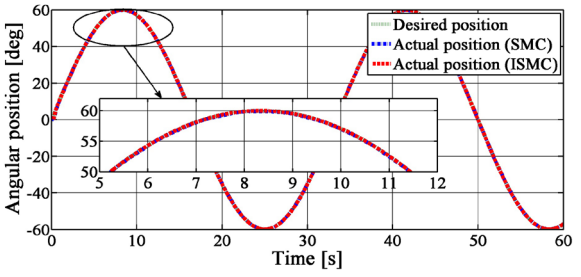

Fig. 9. *Simulation results of sinusoidal input tracking for SMC and ISMC*

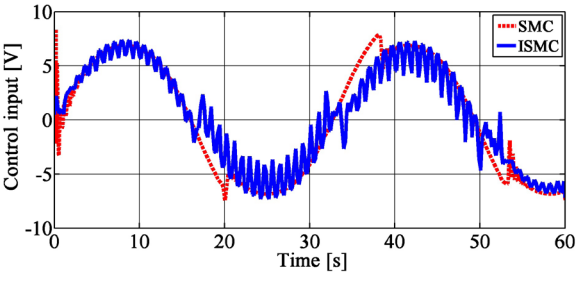

Fig. 10. *Simulation results for the control input applied to SMC and ISMC (Sine reference)*

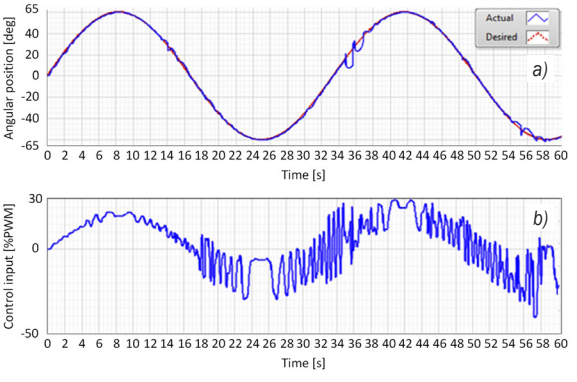

Fig. 11. *Experimental results of a) trajectory tracking and b) control effort using SMC*

Fig. 11 illustrates the desired trajectory tracking of a flexible joint manipulator obtained through experimental platform using SMC. This figure shows the tracking performance of the manipulator in real time along with control input, which was used for said purpose. These results confirm adequate tracking

performance at the expense of undesirable chattering in the control input as observed in the simulation (see Fig. 10).

Fig. 12 shows errors in tracking between the actual trajectory and the desired trajectory when the manipulator is subjected to the SMC approach in real time.

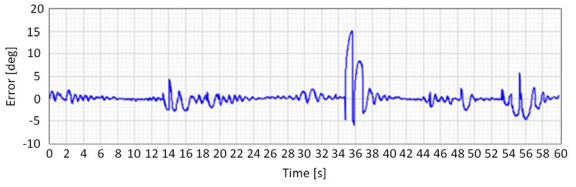

Fig. 12. *Experimental result of steady-state error using SMC*

Fig. 13 presents experimental results of the desired trajectory tracking of the manipulator based on the ISMC law. The control input used by the system for tracking purposes is also shown. Over performance of ISMC over SMC in terms of tracking performance is obvious while comparing Figs. 11 and 13. Furthermore, ISMC offers negligible steady-state error between the actual trajectory and the reference trajectory as depicted in Fig. 14.

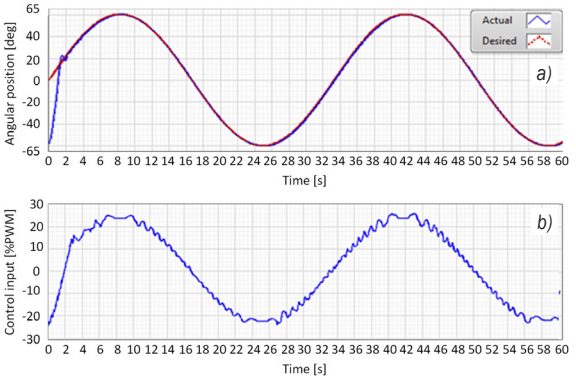

Fig. 13. *Experimental results of a) trajectory tracking and b) control effort using ISMC*

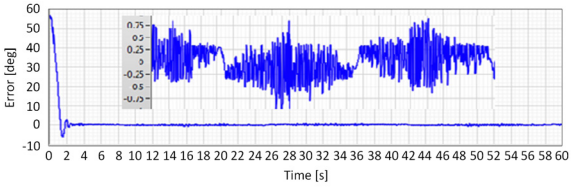

Fig. 14. *Experimental results of steady-state error using ISMC*

4 CONCLUSION

This research addresses the behaviour of a flexible joint manipulator including the actuator dynamic for nonlinear control approaches. The model of the manipulator has been derived using the Euler-Lagrange method, which is then used to study the effectiveness of the nonlinear control techniques for tracking performance. The nonlinear approaches under study include MSC and ISMC. A simulation has been conducted in MATLAB/Simulink while experimental validation of the designed control law has been carried out on a custom developed platform consisting of a single-link flexible joint manipulator. SMC approach resulted in chattering phenomena both in simulation and experimental results. This problem was eliminated by devising a control law based on ISMC, which also reduces steady-state error. Experimental results obtained in the present research can find enormous potential in application domains involving flexible robotic manipulators including but not limited to medical, space, and industrial automation.

5 REFERENCES

[1] Finžgar, M., Podržaj, P. (2017). Machine-vision-based human-oriented mobile robots: A review. *Strojniški vestnik-Journal of Mechanical Engineering*, vol. 63, no. 5, p. 331-348, **DOI:10.5545/sv-jme.2017.4324**.

[2] Iqbal, J., Ajwad, S.A., Syed, Z.A., Abdul, A.K, Islam, R.U. (2016). Automating industrial tasks through mechatronic systems – A review of robotics in industrial perspective. *Tehnički vjesnik - Technical Gazette*, vol. 23, no. 3, p. 917-924, **DOI:10.17559/TV-20140724220401**.

[3] Ajwad, S.A., Asim, N., Islam, R.U, Iqbal, J. (2017). Role and review of educational robotic platforms in preparing engineers for industry. *Maejo International Journal of Science and Technology*, vol. 11, no. 1, p. 17-34.

[4] Salmasi, H., Fotouhi, R., Nikiforuk, P.N. (2009). Tip trajectory tracking of flexible-joint manipulators driven by harmonic drives. *International Journal of Robotics & Automation*, vol. 24, no. 2, p. 147-157, **DOI:10.2316/Journal.206.2009.2.206-3283**.

[5] Dawson, D.M., Hu, J., Burg, T.C. (1998). *Nonlinear Control of Electric Machinery*, CRC Press, New York.

[6] Khan, O., Pervaiz, M., Ahmad, E., Iqbal, J. (2017). On the derivation of novel model and sophisticated control of flexible joint manipulator. *Revue Roumaine des Sciences Techniques-Serie Electrotechnique et Energetique*, vol. 62, no. 1, p. 103-108.

[7] Ajwad, S.A., Ullah, M., Khelifa, B., Iqbal, J. (2014). A comprehensive state-of-the-art on control of industrial articulated robots. *Journal of Balkan Tribological Association*, vol. 20, no. 4, p. 499-521.

[8] Lozano, R., Brogliato, B., Egeland, O., Maschke, B. (2013). *Dissipative Systems Analysis and Control: Theory and*

Applications. Springer Science & Business Media, Springer-Verlag London.

[9] Ullah, M.I., Ajwad, S.A., Irfan, M., Iqbal, J. (2016). Non-linear control law for articulated serial manipulators: Simulation augmented with hardware implementation. *Elektronika ir Elektrotechnika*, vol. 22, no. 1, p. 3-7, **DOI:10.5755/j01.eee.22.1.14094**.

[10] Ajwad, S.A., Iqbal, J., Ullah, M.I., Mehmood, A. (2015). A systematic review of current and emergent manipulator control approaches. *Frontiers of Mechanical Engineering*, vol. 10, no. 2, p. 198-210, **DOI:10.1007/s11465-015-0335-0**.

[11] Iqbal, J., Ullah, M., Khan, S.G., Khelifa, B., Ćuković, S. (2017). Nonlinear control systems-A brief overview of historical and recent advances. *Nonlinear Engineering*, vol. 6, no. 4, p. 301-312, **DOI:10.1515/nleng-2016-0077**.

[12] Ailon, A., Lozano, R., M.I. Gil' (2000). Iterative regulation of an electrically driven flexible-joint robot with model uncertainty. *IEEE Transactions on Robotics and Automation*, vol. 16, no. 6, p. 863-870, **DOI:10.1109/70.897798**.

[13] Chien, M.-C., Huang, A.-C. (2007). Adaptive control for flexible-joint electrically driven robot with time-varying uncertainties. *IEEE Transactions on Industrial Electronics*, vol. 54, no. 2, p. 1032-1038, **DOI:10.1109/TIE.2007.893054**.

[14] Bang, J.S., Shim, H., Park, S.K., Seo, J. H. (2010). Robust tracking and vibration suppression for a two-inertia system by combining backstepping approach with disturbance observer. *IEEE Transactions on Industrial Electronics*, vol. 57, no. 9, p. 3197-3206, **DOI:10.1109/TIE.2009.2038398**.

[15] Liu, C., Cheah, C.C., Slotine, J.-J.E. (2008). Adaptive task-space regulation of rigid-link flexible-joint robots with uncertain kinematics. *Automatica*, vol. 44, no. 7, p. 1806-1814, **DOI:10.1016/j.automatica.2007.10.039**.

[16] Chang, Y.-C., Yen, H.-M. (2012). Robust tracking control for a class of electrically driven flexible-joint robots without velocity measurements. *International Journal of Control*, vol. 85, no. 2, p. 194-212, **DOI:10.1080/00207179.2011.643241**.

[17] Iqbal, J., Ullah, M.I., Khan, A.A., Irfan, M. (2015). Towards sophisticated control of robotic manipulators: An experimental study on a pseudo-industrial arm. *Strojniški vestnik - Journal of Mechanical Engineering*, vol. 61, no. 7-8, p. 465-470, **DOI:10.5545/sv-jme.2015.2511**.

[18] Ajwad, S.A., Adeel, M., Ullah, M.I., Iqbal, J. (2016). Optimal v/s Robust control: A study and comparison for articulated manipulator. *Journal of the Balkan Tribological Association*, vol. 22, no. 3, p. 2460-2466.

[19] Ajwad, S.A., Iqbal, J., Khan, A.A., Mehmood, A. (2015). Disturbance-observer-based robust control of a serial-link robotic manipulator using SMC and PBC techniques. *Studies in Informatics and Control*, vol. 24, no. 4, p. 401-408, **DOI:10.24846/v24i4y201504**.

Strojniški vestnik - Journal of Mechanical Engineering 64(2018)1, 56-67
DOI:10.5545/sv-jme.2017.4695
Original Scientific Paper
Received for review: 2017-06-29
Received revised form: 2017-12-13
Accepted for publication: 2017-12-18

Studying the Fatigue Life of a Non-pneumatic Wheel by Using Finite-Life Design for Life Prediction

Zhen Xiao – You Qun Zhao* – Fen Lin – Ming Min Zhu – Yao Ji Deng
Nanjing University of Aeronautics and Astronautics, College of Energy and Power Engineering, Department of Automotive Engineering, China

To avoid pneumatic tire puncture, blow-out and other problems, a new type of non-pneumatic safety wheel called the mechanical elastic wheel (ME-Wheel) has been developed and investigated. The durability of the ME-Wheel is studied to improve its life; at the same time, the best preventive maintenance period can also be provided for the users, to ensure the safety and reliability of the ME-Wheel in operating conditions. The finite-life design method is proposed to predict the ME-Wheel life; the weakest component of ME-Wheel is ascertained by analysing its structure static strength, and the predicted model of pin for lifetime theory is established by using finite-life design method. Furthermore, the ME-Wheel durability is simulated using the finite element method (FEM) on the basis of the established virtual proving ground, and the enhancement coefficient is combined to calculate ME-Wheel lifespan. Finally, the results of theoretical calculation and simulation are verified using endurable road testing. The results show that the methods of theoretical calculation and simulation, which are applied in our paper to predict the lifespan of ME-Wheel, are highly congruent with the experimental results. Therefore, the proposed method is also entirely suitable for other mechanical structures in the durability research field.

Keywords: non-pneumatic wheel, durability, finite-life design, finite element analysis, life test

Highlights

- *A new type of non-pneumatic tire (ME-Wheel) has been developed to avoid problems with traditional tires, such as tire leaking or puncture.*
- *A mechanical model of the hinge unit and pin for ME-Wheels is established.*
- *The weakest key component of the ME-Wheel is determined.*
- *The theoretical calculation method and simulation method used in this paper to predict the life of the ME-Wheel was congruent with experimental results.*

0 INTRODUCTION

Wheels are one of the most essential parts of a vehicle; in particular, military vehicles need wheels with excellent rupture-proof ability in different extreme environments. Many tire companies and research institutes have studied non-pneumatic safety wheels [1] to [4] to protect the safety of passengers. Durability is one of the key performance indicators of the ME-Wheel; its lifespan has an important influence on economy and safety [5] and [6]. The concept of finite-life design requires that no fatigue damage occur during products life-cycle [7]. The finite-life design method is used to study lifetime and obtain the rated lifespan of ME-Wheels; vehicle wheels are not to be damaged, and passengers are to be protected throughout the lifecycle.

An analytical model of a non-pneumatic tire has been proposed by Gasmi et al. [8] and Gasmi and Joseph [9], which consists of a flexible ring belt and a spoke. The main parameters were analysed and verified by finite element method, and researchers studied the outflow field of non-pneumatic tires with contact surfaces and radial stiffness [10] to [12]. Wang et al. [13] and [14] presented a reduced-order compensation scheme for computing the static deformation response of a thick ring supported by a unilateral elastic foundation to an arbitrarily applied force. This scheme avoided solving a set of complex non-linear differential equations and gave an efficient tool for analysing and designing such systems. To satisfy the needs of the development of a modern national defence industry, this paper researched a new type of non-pneumatic wheel: the mechanical elastic wheel (ME-Wheel) [15]. The main components are flexible tire body, hinge unit and suspension hub. To improve the adaptability of military vehicles in complex environments, the ME-Wheel is designed with a statically indeterminate structure. Compared with the conventional pneumatic tire, it has no potential risk factors such as flat tire or leakage. Moreover, it provides excellent comfort with its double-buffered damping structure. Wang et al. [16] have studied the ME-Wheel's structure and ride comfort. Wang et al. [17] have analysed the relationship among the excitation frequency, radial deformation, the bending stiffness of combined elastic rings, and the laminated structure parameters of built-up elastic rings. Zang et al. [18] and [19] have analysed the radial stiffness and the influencing factors of the ME-Wheel. Li et al. [20]

*Corr. Author's Address: Nanjing University of Aeronautics and Astronautics, No.29 Yudao Street Qinhuai District, Nanjing 210016, China, yqzhao@nuaa.edu.cn

have studied the mechanical properties of ME-Wheels and obtained the relationship between the tangential deformation and bending angle of the combined elastic rings via the Laplace transform. Du et al. [21] and [22] established a non-linear three-dimensional finite element model of the wheel interacting with soil, and simulated the different rotational speeds.

Although many researchers have made in-depth studies of life estimation on other pneumatic tire and mechanical products [23], none have studied the ME-Wheel durability. Sokolov [24] and [25] predicted the fatigue life of the pneumatic tires by using the finite element FEM and developed the experimental fatigue curves for rubber-cord composites. In addition, a tensile test of the rubber cord was carried out, and the fatigue curve of the tire under stress and strain conditions was constructed. Topac et al. [26] studied the causes of the fatigue failure of commercial vehicle wheels near ventilation holes. The finite element model was established using ANSYS / Workbench, and the static stress was analysed. Then the wheel was predicted by S-N curve, based on the stress life method and finally, the wheel structure was improved. Rosa et al. [27] evaluated the damage of mechanical components with a stress-controlled rheological spring-slider model combined with finite element method. Ettefagh et al. [28] carried out fatigue life influenced by vibration performance of a friction stir-spot-welded specimen, verified by the finite method and related experiments during analysing four different welded methods. Dobado and Morales [29] studied the fatigue failure of the 7075-T6 aluminium alloy cantilever by using the multi-axis strain energy density and evaluated the potential application of light alloy mechanical parts in the automotive industry.

The ME-Wheel is subjected to complex alternating load during movement; therefore, it is very difficult to predict its lifetime. The prediction method proposed in this paper is to obtain the weakest part of the structure by static strength analysis and calculate the lifetime of the part; the rapid prediction of ME-Wheel life is then realized. The research method used in this paper is that the ME-Wheel finite element model is established, and its validity is verified using a static strength test. After that, the weakest part of ME-Wheel is obtained by finite element simulation. Moreover, the wheel lifetime prediction model is calculated by using the finite-life design method, and the analytical results of lifetime prediction are obtained. Finally, the virtual proving ground is established by the finite element method, and the durability of the ME-Wheel is simulated and compared with the endurance road testing results.

1 STRUCTURE AND STATIC STRENGTH ANALYSIS OF ME-WHEEL

The whole lifetime of the structure depends on the lifetime of parts in mechanical structures [30], and the life prediction of ME-Wheel can be achieved by calculating the life of the weakest parts.

1.1 ME-Wheel Structure

Fig. 1 shows the structure of ME-Wheel, which is composed of the flexible tire body, hinge unit, pin, clamping ring, combined elastic rings, and suspension hub components. The assembly relationship is as follows:

1) The five combined elastic rings locked by twelve sets of clamping rings are juxtaposed to form the ME-Wheel frame, as shown in Fig. 2.

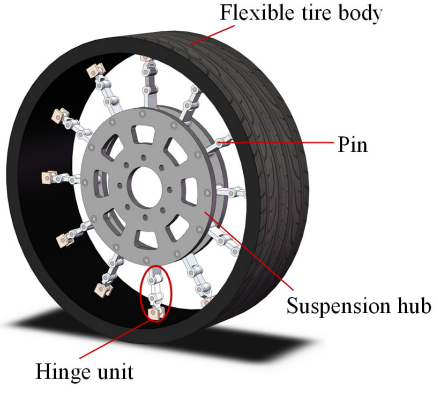

Fig. 1. *ME-Wheel configuration*

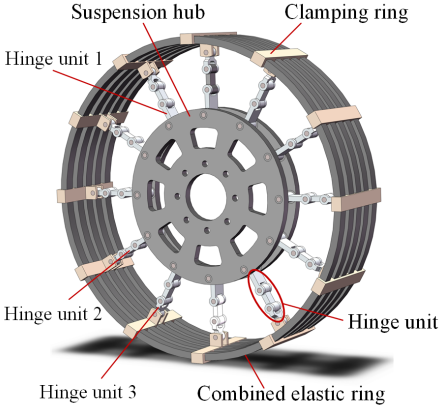

Fig. 2. *ME-Wheel frame*

2) The suspension hub is installed at the centre of the combined elastic rings, and the clamping ring and the suspension hub are connected by the hinge unit.

3) The combined elastic rings are embedded in the flexible tire body.

1.2 Static Strength Analysis of ME-Wheel

The static strength of the ME-Wheel 3D finite element model is calculated using COSMOS/WORKS finite element simulation software according to the bench test condition. The various components grid density of ME-Wheel was different to save computing resources as much as possible without affecting the simulation results. The finite element method (FEM) size is pin 6 mm, hinge group 8 mm, clamping ring 8 mm, combined elastic rings 10 mm, suspension hub 10 mm, flexible tire body 16 mm, pavement 200 mm. The number of nodes is 290,033, the number of mesh elements is 160,764, and the element types are tetrahedral mesh. The road model is applied a fixed constraint, and the centre of suspension hub is applied a vertical load to calculate the radial stiffness; the load settings are 5 kN, 10 kN, 15 kN, 20 kN, 25 kN, 30 kN, 35 kN. As shown in Fig. 3. The radial stiffness of the wheel is tested using the ME-Wheel radial mechanical test bench; the test bench is shown in Fig. 4. Fig. 5 is the contrast curves of radial stiffness between ME-Wheel simulation values and experimental values.

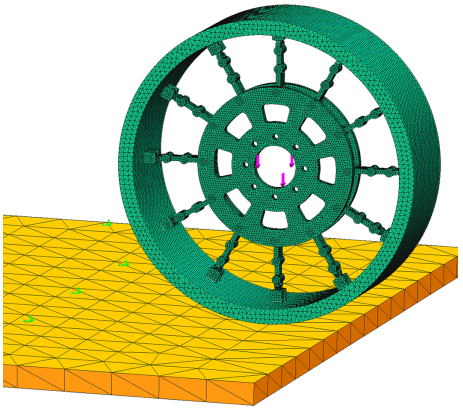

Fig. 3. *Define constraints and loads*

As seen in Fig. 5, the radial stiffness curve simulation values of ME-Wheel agree with the experimental data, and the correctness of the finite element model is verified. It shows that the finite element model of the ME-Wheel is satisfactory with the required simulation.

The static strength of the ME-Wheel is simulated, and the stress nephogram is shown in Fig. 6.

Seen from Fig. 6, when the ME-Wheel is applied to the radial load, the pin is subjected to the maximum stress, so the pin is the weakest component, and the lifetime of the ME-Wheel depends on the durability of the pin.

Fig. 4. *ME-Wheel bench test*

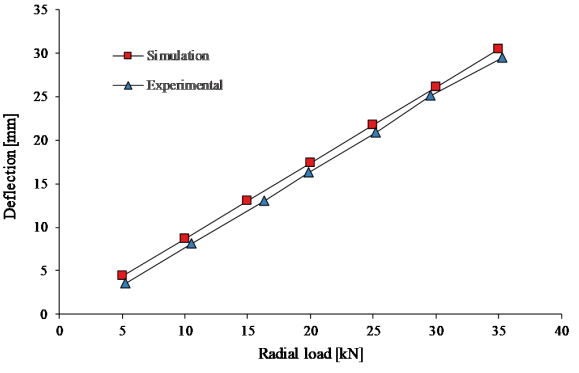

Fig. 5. *Radial stiffness comparison curves of ME-Wheel*

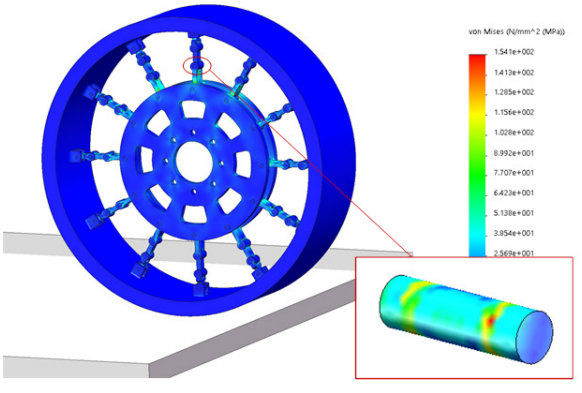

Fig. 6. *ME-Wheel radial loading stress nephogram*

Because the pin plays a crucial role in the ME-Wheel lifespan, a set of hinge units is extracted to perform uniaxial tensile tests to verify the

effectiveness of the pin-hinge unit model. Moreover, to ensure the validity of uniaxial tensile test, the experimental fixture is completely designed according to the internal condition of the hinge unit assembly. The tensile test is shown in Fig. 7. The contrast curves of tensile test results and simulation results are shown in Fig. 8.

Fig. 7. *Hinge unit tensile test*

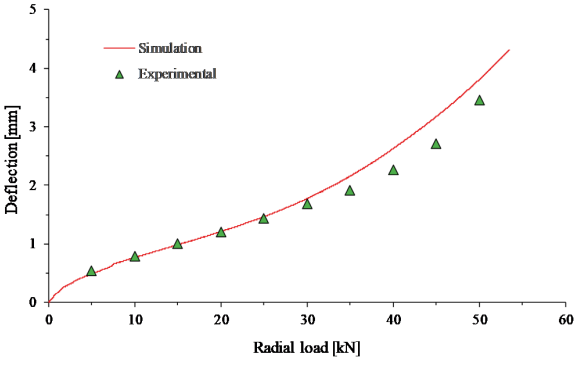

Fig. 8. *Comparison of experiments and simulation results*

Through the tensile test and finite element simulation, it can be seen that the deformation of the hinge unit is caused by the bending deformation of the pin. As can be seen from Fig. 8, the finite element simulation is a relatively good match with the hinge unit tensile test curve, for which the maximum relative error is 14.4 %, and the average error is 4.9 %. Thus, the finite element model validity of the pin-hinge unit assembly is verified, and the requirements of later research are met.

2 LIFE PREDICTION OF PIN UNDER FINITE-LIFE DESIGN

The mechanical structure of the anti-fatigue design (fatigue life design) is divided into finite-life design and infinite-life design. Infinite-life design is suitable for fixed mechanical structures, while the finite-life design is applied to a movable mechanical structure, and the finite-life design is much closer to the real environment. The basic flow chart of finite-life design is shown in Fig. 9.

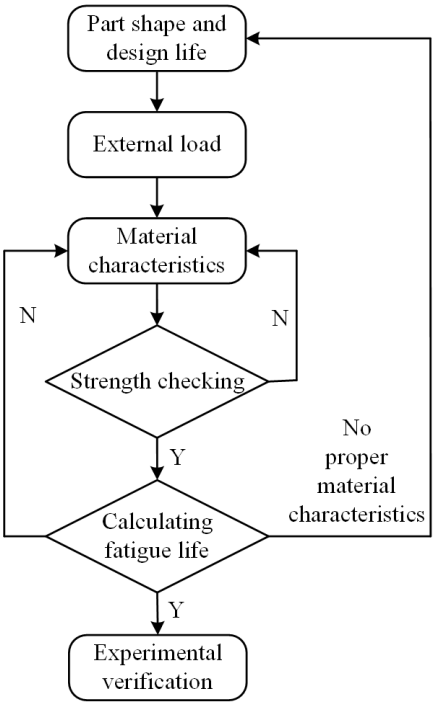

Fig. 9. *Finite-life design flow*

2.1 Mechanical Analysis of ME-Wheel

The stress of the hinge unit at different positions is analysed when the ME-Wheel is stationary; the hinge unit 1 to 12 is clockwise from the top hinge unit, as shown in Fig. 10a. From the ME-Wheel's bearing way, the suspension hub is in the suspended state when the ME-Wheel is subjected to loads from suspension hub. The upper half of the hinge units 1, 2, 3, 11, 12 is in the stretched state, Hinge units 5, 6, 7, 8, 9 in the lower part are under compression and bending deformation around the hinge point; at this time, the hinge unit does not bear any force. Hinge unit 4 and 10 are in a level-free condition, and the bearing force of hinge units is shown in Fig. 10b.

If the bearing force of the ME-Wheel in the initial position is FZ, the forces of hinge Units 1, 2, 3, 11, 12 are F1, F22, F32, F31, F21. The force balance equation of the ME-Wheel can be expressed as:

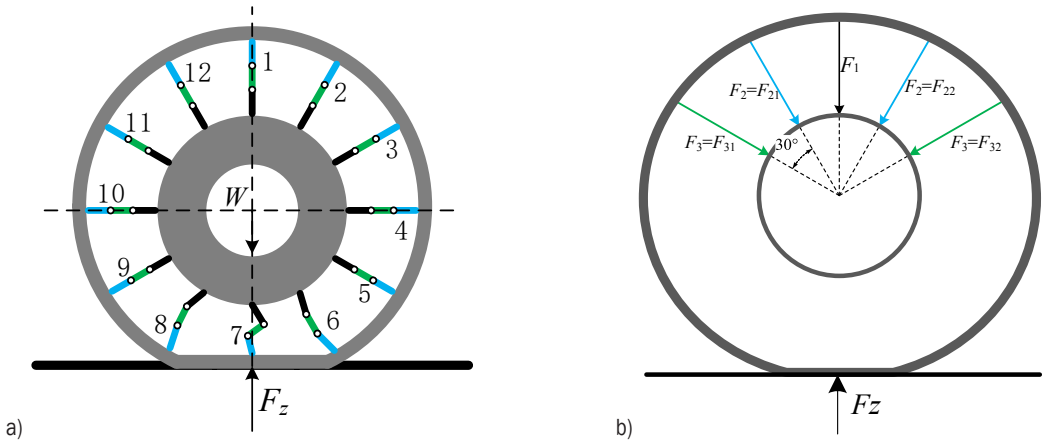

Fig. 10. *The characterization of hinge unit for ME-Wheel; a) the number of hinge unit, and b) the load conditions of hinge unit*

$$\begin{cases} F_{21} = F_{22} \\ F_{31} = F_{32} \\ F_Z = F_1 + 2F_{21}\cos\dfrac{\pi}{6} + 2F_{31}\cos\dfrac{\pi}{3} \cdot \\ \quad = F_1 + 2F_{22}\cos\dfrac{\pi}{6} + 2F_{32}\cos\dfrac{\pi}{3} \end{cases} \quad (1)$$

For convenience, F_{21} and F_{22} are marked as F_2, F_{31} and F_{32} are marked as F_3. Therefore, the above equation becomes

$$\begin{cases} F_2 = F_{21} = F_{22} \\ F_3 = F_{31} = F_{32} \\ F_Z = F_1 + 2F_2\cos\dfrac{\pi}{6} + 2F_3\cos\dfrac{\pi}{3} \end{cases} . \quad (2)$$

If the deformation amount of hinge Unit 1 is Δl_1, hinge Unit 2 and 12 is Δl_2, and the hinge Unit 3 and 11 is Δl_3, all hinge unit tensile stiffness is EA_J, and the original length is l, the physical deformation equation is:

$$\begin{cases} \Delta l_1 = \dfrac{F_1 l}{EA_J} \\ \Delta l_2 = \dfrac{F_2 l}{EA_J} \\ \Delta l_3 = \dfrac{F_3 l}{EA_J} \end{cases} . \quad (3)$$

According to the tensile deformation of hinge unit deformation, the compatibility equation of deformation is:

$$\begin{cases} \Delta l_2 = \Delta l_1 \cos\dfrac{\pi}{6} \\ \Delta l_3 = \Delta l_1 \cos\dfrac{\pi}{3} \end{cases} . \quad (4)$$

The solution obtained by Eqs. (2), (3) and (4) is:

$$\begin{cases} F_1 = \dfrac{1}{3}F_Z \\ F_2 = \dfrac{\sqrt{3}}{6}F_Z \\ F_3 = \dfrac{1}{6}F_Z \end{cases} . \quad (5)$$

Seen from the above analysis and calculation results, the closer a hinge unit is located to the middle of the vertical position, the greater the force.

The pin in the ME-Wheel connects the clamping ring, hinge unit, and the suspension hub to each other, and allows the hinge unit to freely rotate within a certain angle between the clamping ring and the suspension hub during the moving process. Furthermore, the pin can also transfer torque from the suspension hub centre to the ME-Wheel.

When the ME-Wheel runs straight, the pin mainly bears the bending moment and shear force. A simplified drawing of the pin under stress is shown in Fig. 11.

According to the actual force of the hinge unit, q in Fig. 11 is uniform load, q and F_S are the tension from the suspension hub and the supporting force from the hinge unit. The pin length is expressed by l. Based on the mechanical model in the diagram, the mechanical equilibrium equation is as follows,

$$\sum F = 0, \quad \sum M = 0, \quad (6)$$

and calculates,

$$2F_S = F, \quad M = \frac{ql^2}{8}, \tag{7}$$

$$\tau = \frac{F_S}{A}, \tag{8}$$

where F_S is the support force from the hinge unit, M is the bending moment on the pin, τ is the shear force on the pin, and A is the cross-sectional area of the pin.

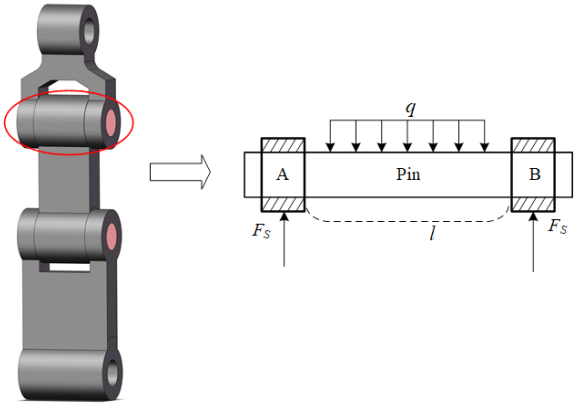

Fig. 11. *Pin force diagram*

When a vehicle moves, the tire is subjected to dynamic loads from the road. The formula is expressed as,

$$F_Z = DF_{jZ}, \tag{9}$$

where F_{jZ} is the vertical static load of the tire, and D is the tire dynamic load coefficient.

According to the road testing, the average driving speed of the vehicle is 45 km/h, the road roughness coefficient S_0 = 2×10^{-6} m, taking the dynamic load factor is 2.1 **[31]**, calculates the dynamic load of the ME-Wheel as 36,015 N. The detailed calculation results are shown in Table 1.

Table 1. *Calculation results of ME-Wheel mechanics*

Model	F_1 [N]	τ [MPa]	M [N·mm]
Pin	12005	53.1	25504

When the ME-Wheel is cornering, the force of the vehicle is shown in Fig. 12.

It can be seen from Fig. 12, the establishment of the vehicle when turning the frame of reference, the wheel will be used by the inertia force at this time. If the vehicle is regarded as a rigid body, its inertial centrifugal force is,

$$F_x = MR\omega^2 = \frac{MV^2}{R}, \tag{10}$$

where M is the vehicle mass, the R is the turning radius, and V is the instantaneous speed of the turning.

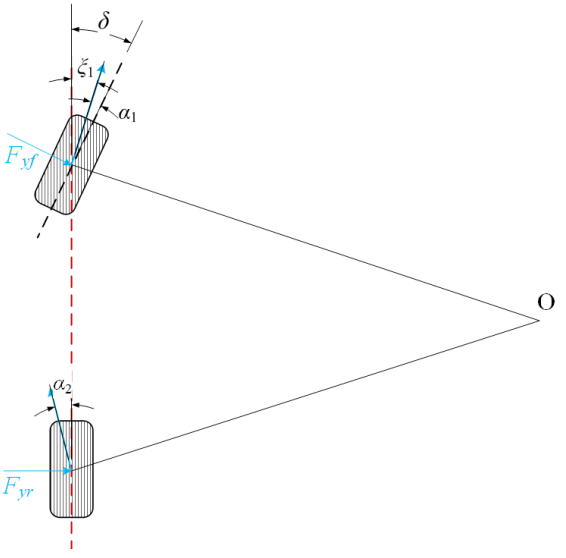

Fig. 12. *Wheel steering force*

When the vehicle turns, its lateral force is provided by friction, and its value cannot exceed the ground adhesion, that is:

$$\begin{cases} F_y \le F_\varphi \\ F_{y\max} = F_\varphi = \varphi F_N \end{cases}, \tag{11}$$

where φ is the adhesion coefficient and F_N is the dynamic load of the wheel. Vehicle steering is due to the lateral force of the tire. For all vehicles running at a speed of V, the sum of all lateral forces on the tire is equal to mass multiplied by the centripetal acceleration, that is,

$$\sum F_y = F_{yf} + F_{yr} = \frac{MV^2}{R}. \tag{12}$$

Among them, F_{yf} and F_{yr} are the lateral forces acting on the front and rear axle of the ME-Wheel, respectively.

Table 2. *The relationship between adhesion and lateral force*

Speed [km/h]	Adhesion [N]	ME-Wheel lateral force [N]	Pin lateral force [N]
0	9800	0	0
10	27440	2500	208.3
20	29400	10000	833.3
30	31360	22500	1875
40	33320	33320	2776.7

Because the ME-Wheel has 12 hinge units, the lateral force of each hinge (pin) unit is F_Y/12.

With each ME-Wheel bearing 1 t load, the speed is 0 km/h to 40 km/h, φ = 1, its adhesion and lateral force are calculated, as shown in Table 2.

2.2 Pin Life Prediction

When the ME-Wheel moves, the loads of the hinge unit and pin are periodic loads. To study the mechanism of stress cycle and fatigue failure of the pin during wheel motion, the higher stress point of the pin is picked up and its stress is analysed. Fig. 13 shows the variation stress of a dangerous point with a loading angle.

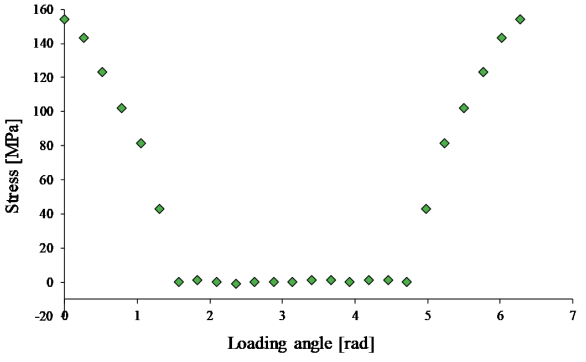

Fig. 13. *The stress of the dangerous point with the loading angle*

Seen from Fig. 13, the pin is subjected to symmetric cyclic stress. For the bending load applied symmetric cyclic stress, an improved Buch S-N curve is used [32]. Compared with the Buch idealization curve, the improved Buch curve is reflected in two aspects. First, the S-N curve of the part under the bending load should not be parallel to the S-N curve of the material. Second, the life N should be the turning point life N0 instead of constant 106. Its parts S-N curve is calculated by the following formula, and the corrected part S-N curve is shown in Fig. 14.

$$\lg N = \lg N_0 - m_2\left(\lg\sigma - \lg\sigma_{-1D}\right), \tag{13}$$

where M_2 is the slope factor of the S-N curve, and the expression is as follows,

$$m_2 = \frac{\lg N_0 - 3}{\lg\left(\dfrac{0.9\sigma_b}{\sigma_{-1D}}\right)}, \tag{14}$$

where σ_{-1} is the fatigue limit of material under symmetric cyclic stress; σ_{-1D} is the bending fatigue limit of the component, N_0 is the life at the turning point; σ_b is the tensile strength of the material.

$$\sigma_{-1D} = \frac{\sigma_{-1}}{K_{\sigma D}}, \tag{15}$$

$$K_{\sigma D} = \frac{K_\sigma + \dfrac{1}{\beta} - 1}{\varepsilon}, \tag{16}$$

where K_σ is the effective bending stress concentration factor, ε is the size correction factor, and β is the surface quality correction factor.

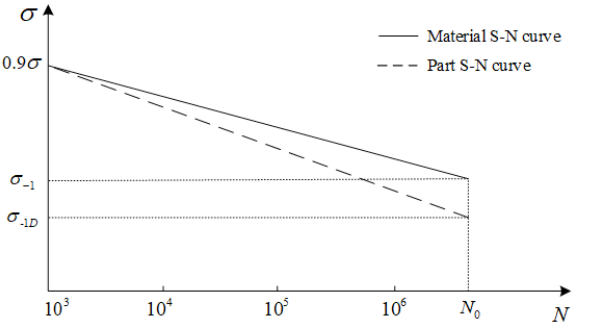

Fig. 14. *Corrected part S-N curve*

The work safety factor is calculated by Eq. (17):

$$n_\sigma = \frac{\sigma_{-1DN}}{\sigma_{\max}}, \tag{17}$$

where σ_{-1DN} is the fatigue life of the component when the design life is N. the design requires life of ME-Wheel is not less than 6000 km.

$$K_\sigma = \frac{\sigma_{-1}}{\left(\sigma_{-1}\right)_k}. \tag{18}$$

The size correction factor ε is obtained from the size coefficient curve, as shown in Fig. 15:

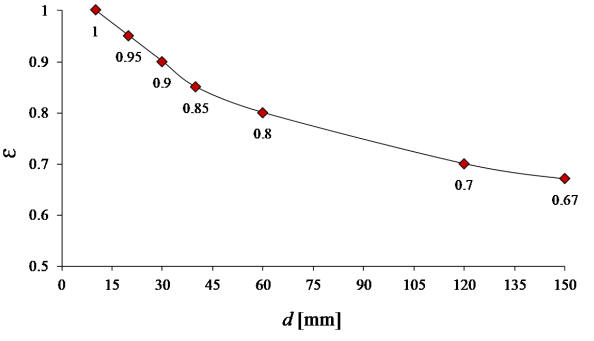

Fig. 15. *Size coefficient curve*

$$\sigma_s = \frac{M}{W}, \tag{19}$$

where W is the flexural factor of the section, the pin is cylindrical, and thus can be expressed by the following equation,

$$W = \frac{\pi d^3}{32}. \quad (20)$$

The material parameters of the ME-Wheel pin used in the formula are shown in Table 3.

Table 3. *Pin material parameters*

Model	Material Properties				
Pin	σ_{-1} [MPa]	σ_b [MPa]	K_σ	β	N_0
	380	710	1.8	0.92	3.4×10^6

The dynamics analysis model and pin size parameters in Section 2.1 are taken in Eq. (19); it obtains σ_s = 150 MPa. and n_σ = 2.44 is calculated by Eq. (17). According to the shape of the pin $[n]$ = 2, $n_\sigma > [n]$, it shows that components of the finite-life design are used safely in the design life of N.

The calculated stress of the component is,

$$\sigma_g = [n]\sigma_{\max}, \quad (21)$$

where σ_g=300 MPa is calculated by Eq. (21). According to Fig. 14, the modified component S-N curve, the cycle number of the ME-Wheel can be calculated as $N = 2.6\times10^6$ times, so the ME-Wheel life is 7300 km. which is calculated by the finite-life design method.

The turning velocity of the testing vehicle is 20 km/h, according to Tables 1 and 2, it can be obtained that the value of vertical load for the pin is 12,005 N, however, the value of lateral force is 833.3 N. Obviously, the lateral forces account for merely 6.94% of the vertical load. Moreover, theoretical calculations are based on the maximum vertical load value (the calculated value is conservative), but the calculated value of lifespan is not accurate enough because of coupling with the lateral force. Therefore, the influence of the lateral force should be neglected in the computing processes. However, to ensure the authenticity of simulation analysis, the composite conditions, including straight moving and steering motion, are comprehensively considered in the following finite element analysis.

3 LIFE PREDICTION AND EXPERIMENTAL VERIFICATION OF THE ME-WHEEL

3.1 Three-Dimensional Model of a Virtual Proving Ground

The durability test of a vehicle proving ground is the main way to test the fatigue durability of the vehicle. The test road in the vehicle durability proving ground includes high-speed runway (cement road), cobblestone pavement, washboards, Belgium block road and so on; each road makes the vehicle loads unique. Building a durability model of a virtual proving ground can give more realistic road load spectrum for ME-Wheel fatigue analysis.

The cobblestone pavement not only provides vertical loads for the ME-Wheel but also provides greater lateral and longitudinal impact loads; the washboard surface give periodic harmonic vibration and is often used to study the fatigue strength of the wheel under forced vibration; the Belgium block road is a random load road that is used to examine the structural strength and vibration characteristics of the ME-Wheel, and is one of the roads used in automotive durability testing. Therefore, a virtual proving ground model is built by the cobblestone pavement, washboards, Belgium block road and the cement road can better simulate the real running conditions of ME-Wheel. Not only is the computation time is saved, but also sufficient input load to the ME-Wheel is used to check the durability of the component. Moreover, the quick prediction of the ME-Wheel lifespan is realized.

According to the real proving ground situation, the specific parameters of durability road model are shown in Table 4. The cement road, Belgium block road, cobblestone pavement, washboards, curve, the length are 30 m, 15 m, 15 m, 15 m, 62 m, respectively, and the width is 2 m. The durability road model is shown in Fig. 16.

Table 4. *The parameters of the durability road*

Road	Stone size [mm]	Average height [mm]	Stone spacing [mm]	Diameter [m]
Washboards	620	20	880	--
Belgium block road	200×120	5	--	--
Cobblestone pavement	90 to 200	10	--	--
Curve	--	--	--	80

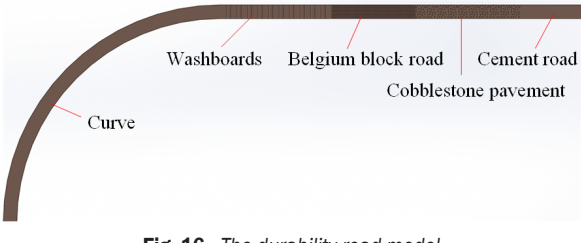

Fig. 16. *The durability road model*

3.2 ME-Wheel Durability Simulation

According to the load to test the vehicle, the vertical load of 9800 N is applied in the centre of the suspension hub (the weight of the test vehicle is 4 tons, and each wheel bears a 1 ton load), the road is fixed, the contact between the road and the ME-Wheel is surface-to-surface contact; the gravity direction is defined as vertical downwards; a variable speed motor at the centre of the suspension hub is applied; the speed on the cement road is 60 km/h; on the cobblestone pavement, Belgium block road, washboards, the speed is 30 km/h, and 20 km/h on the curve. The ME-Wheel motion simulation is shown in Fig. 17. The total running distance of the ME-Wheel is 137 m, and the simulation time is 18.3 s. Based on the motion simulation analysis, the dynamic load between the flexible tire body and the road surface is extracted by time as the abscissa, and the ME-Wheel load spectrum is established, as shown in Fig. 18. Seen from Fig. 18, the cobblestone pavement and washboard surfaces have a greater impact on ME-Wheel, so the enhancement coefficient of the two kinds of road is larger when the driving time is about 11 s, a slight slip phenomenon occurs during the cornering of the ME-Wheel. The specific enhancement coefficients for different roads are shown in Table 5.

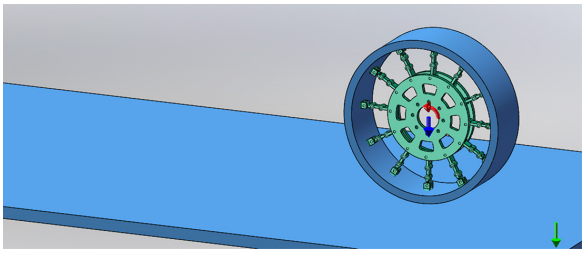

Fig. 17. *ME-Wheel motion simulation*

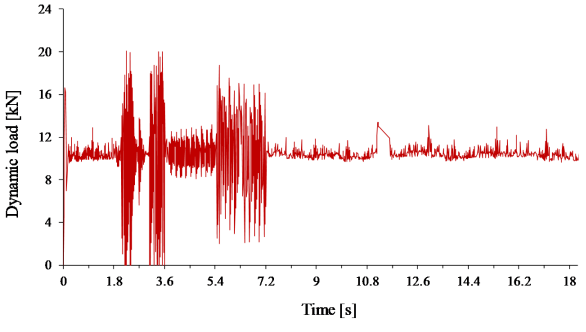

Fig. 18. *ME-Wheel load spectrum*

To make the collected load spectrum, information can be used for the analysis and calculation of fatigue performance; the rain-flow counting method is used for the cumulative frequency distribution statistics of the load history. The stress amplitude and mean values of each node are calculated by the rain flow counting tool and obtains amplitude-mean rain flow matrix, as shown in Fig. 19.

Table 5. *Enhancement coefficient of different road*

Road	Speed [km/h]	Enhancement coefficient	Proportion of roads [%]	Comprehensive enhancement coefficient
Cement road	60	0.8	21.90	5.22
Cobblestone pavement	30	19	10.95	
Belgium block road	30	4.4	10.95	
Washboards	30	18.5	10.95	
Curve	20	1.0	45.25	

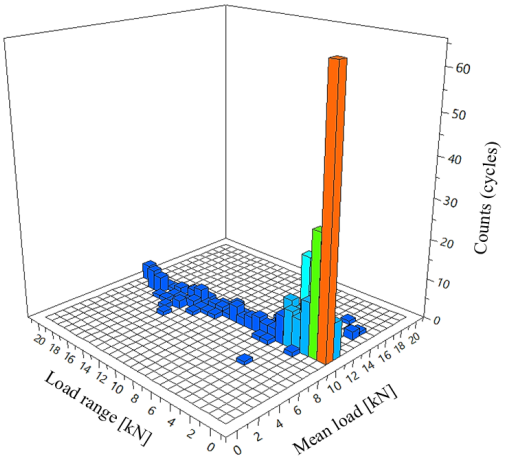

Fig. 19. *Rain flow matrix*

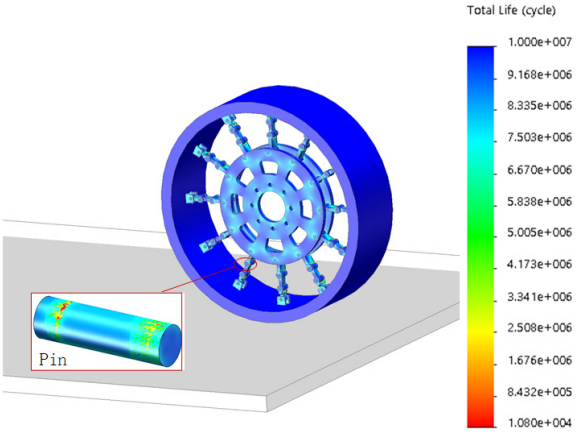

Fig. 20. *ME-Wheel durability simulation results*

The survival rate is set to 95 % by using the nominal stress method and Goodman correction model

in the simulation of the ME-Wheel. The durability of the ME-Wheel simulation results is shown in Fig. 20.

Seen from Fig. 20, the pin life is the lowest, and the minimum number of cycles on the endurance road is 1.08×10^4. Therefore, the overall life of the ME-Wheel structure obtained via dynamic finite element durability analysis is $(1.08\times10^4)\times137\times5.22=7723.8$ km. In Section 2.2, the theoretical calculation result is 7300 km, and the error of simulation result is about 5.49 %. Thus, the finite element analysis of durability verifies the correctness of the finite-life design method used in this paper to calculate the pin life.

3.3 Endurance Road Testing

The test vehicle is a certain type of military vehicle that replaces all pneumatic tires with ME-Wheels and tests the ME-Wheel durability on endurance road. The vehicle odometer to record the driving distance is used. Specific data for endurance road testing are shown in Table 6. Fig. 21 is an endurance road testing image of ME-Wheel.

Table 6. *ME-Wheel endurance road testing data*

Road	Speed [km/h]	Enhancement coefficient	Proportion of roads [%]	Comprehensive enhancement coefficient
Cement road	60	0.8	30	7.32
Cobblestone pavement	30	19	20	
Belgium block road	30	4.4	20	
Washboards	30	18.5	10	
Gravel road	30	3.8	10	
Scale road	30	1.8	5	
Twist road	10	1.6	5	

Fig. 21. *ME-Wheel endurance road testing*

The total vehicle mileage is about 1200 km, and the ME-Wheel pin is broken. According to Table 6, it is calculated that the overall life of the ME-Wheel structure is 1200 × 7.32 = 8784 km.

A comparison of endurance road testing, theoretical calculations and finite element simulation, shows that the three results are close to each other. The deviation between the theoretical calculation and endurance road testing is 16.9 %, and the finite element calculation and endurance road testing deviation is only 12.07 %. Moreover, the validity of the simulation and theoretical calculation is verified. Through the analysis of above results, more reasonable deviation sources are:

1) The virtual endurance road is not complete; only five typical roads are selected and accounting for more than the road modelling and simulation.
2) The speed, weight and other parameters of test vehicle are slightly different from the simulation environment, which results in deviation during vehicle testing.
3) During the design of the ME-Wheel, the parameters used in ME-Wheel dynamic load calculation and finite-life design are conservative. Thus, the theoretical calculation and simulation results of ME-Wheel are smaller than the endurance road testing results to improve the safety factor.

4 CONCLUSIONS

1) The ME-Wheel finite element model is established, and its correctness is verified by bench test and tensile test. Based on the simulation results of ME-Wheel static strength, it ascertains that the weakest component is the pin, because the most stress is concentrated on it.
2) A life prediction model is suitable for the ME-Wheel, which is established by the finite-life design, and the theoretical life of the ME-Wheel can be predicted with relative precision. The results of theoretical calculation are compared with the durability simulation results and the endurance road testing results, the deviations are 5.49 % and 16.9 %, respectively.
3) The virtual vehicle proving ground model is established, and the ME-Wheel life is predicted by the durability simulation. The comparison error between the simulation and endurance road tests is 12.07 %, which shows that the durability-enhanced virtual proving ground model and motion simulation analysis can predict the ME-Wheel life relatively accurately. Furthermore, the analysis method applied in this paper can not only reduce the vehicle test time but also provide a reference for durability optimization in the future.

5 ACKNOWLEDGEMENTS

Authors would like to thank the supported by the National Natural Science Foundation of China (No. 11672127), the Major Exploration Project of the General Armaments Department of China (No. NHA13002), the Fundamental Research Funds for the Central Universities (No. NP2016412), and Jiangsu Innovation Program for Graduate Education and the Fundamental Research Funds for the Central Universities (No. KYLX16_0330).

6 REFERENCES

[1] Kumar, A.S., Kumar, R.K. (2016). Force and moment characteristics of a rhombi tessellated non-pneumatic tire. *Tire Science and Technology*, vol. 44, no. 2, p. 130–148. **DOI:10.2346/tire.16.440205**.

[2] Cho, J.R., Lee, J.H., Jeong, K.M., Kim, K.W. (2012). Optimum design of run-flat tire insert rubber by genetic algorithm. *Finite Elements in Analysis and Design*, vol. 52, p. 60-70, **DOI:10.1016/j.finel.2011.12.006**.

[3] Jo, H., Lee, C., Kim, K., Kim, D. (2013). Vibration Characteristics of Non-pneumatic Tire with Honeycomb Spokes. *Transactions of the Korean Society of Automotive Engineers*, vol. 21, no. 4, p. 174–180. **DOI:10.7467/ksae.2013.21.4.174**.

[4] Ju, J., Kim, D.M., Kim, K. (2012). Flexible cellular solid spokes of a non-pneumatic tire. *Composite Structures*, vol. 94, no. 8, p. 2285-2295, **DOI:10.1016/j.compstruct.2011.12.022**.

[5] Lee, Y.L., Pan, J., Hathaway, R.B., Barkey, M. (2005). *Fatigue Testing and Analysis*. Elsevier, New York.

[6] Liu, J., Wang, Y., Li, W. (2010). Simplified fatigue durability assessment for rear suspension structure. *International Journal of Automotive Technology*, vol. 11, no. 5, p. 659-664, **DOI:10.1007/s12239-010-0078-1**.

[7] Carpinteri, A., Spagnoli, A., Vantadori, S. (2009). Size effect in S–N curves: A fractal approach to finite-life fatigue strength. *International Journal of Fatigue*, vol. 31, no. 5, p. 927-933, **DOI:10.1016/j.ijfatigue.2008.10.001**.

[8] Gasmi, A., Joseph, P.F., Rhyne, T.B., Cron, S.M. (2012). Development of a two-dimensional model of a compliant non-pneumatic tire. *International Journal of Solids and Structures*, vol. 49, no. 13, p. 1723-1740, **DOI:10.1016/j.ijsolstr.2012.03.007**.

[9] Gasmi, A., Joseph, P.F. (2012). Contact solutions for a circular orthotropic beam accounting for transverse normal strain. *International Journal of Engineering Science*, vol. 55, p. 1-17, **DOI:10.1016/j.ijengsci.2012.01.011**.

[10] Kim K, Ju J. (2015). Mechanical metamaterials with 3D compliant porous structures. *Composite Structures*, vol. 132, p. 874-884, **DOI:10.1016/j.compstruct.2015.06.060**.

[11] Heo, H., Ju, J., Kim, D.M., Kim, H. (2014). A computational study of the flow around an isolated non-pneumatic tire. *SAE International Journal of Passenger Cars: Mechanical Systems*, vol. 7, no. 1, p. 405-412, **DOI:10.4271/2014-01-9123**.

[12] Kim, K., Ju, J., Kim, D. (2013). Static contact behaviors of a non-pneumatic tire with hexagonal lattice spokes. *SAE International Journal of Passenger Cars: Mechanical Systems*, vol. 6, no. 3, p. 1518-1527, **DOI:10.4271/2013-01-9117**.

[13] Wang, C., Ayalew, B., Rhyne, T., Cron, S., Dailliez, B. (2015). Static analysis of a thick ring on a unilateral elastic foundation. *International Journal of Mechanical Sciences*, vol. 101-102, no. 429-436, **DOI:10.1016/j.ijmecsci.2015.08.015**.

[14] Wang, C., Ayalew, B., Rhyne, T., Cron, S., Dailliez, B. (2016). Forced in-plane vibration of a thick ring on a unilateral elastic foundation. *Journal of Sound and Vibration*, p. 380, p.279-294, **DOI:10.1016/j.jsv.2016.06.010**.

[15] Zhao, Y.Q., Zang, L.G., Chen, Y.Q., Li, B., Wang, J. (2015). Non-pneumatic mechanical elastic wheel natural dynamic characteristics and influencing factors. *Journal of Central South University*, vol. 22, no. 5, p. 1707-1715, **DOI:10.1007/s11771-015-2689-1**.

[16] Wang, W., Zhao, Y.Q., Wang, J., Zang, L.G. (2012). Structure analysis and ride comfort of vehicle on new mechanical elastic tire. *Proceedings of the FISITA 2012 World Automotive Congress*, Beijing, p. 199-209, **DOI:10.1007/978-3-642-33795-6_17**.

[17] Wang, Q., Zhao, Y.Q., Du, X.B., Zhu, M.M., Fu, H.X. (2016). Equivalent stiffness and dynamic response of new mechanical elastic wheel. *Journal of Vibroengineering*, vol. 18, no. 1, p. 431-445.

[18] Zang, L.G., Zhao, Y.Q., Jiang, C., Li, B., Wang, W. (2015). Mechanical elastic wheel's radial stiffness characteristics and their influencing factors. *Journal of Vibration and Shock*, vol. 34, no. 8, p. 181-186. (in Chinese)

[19] Zang, L.G., Zhao, Y.Q., Li, B., Wang, Q., Fu, H.X. (2015). Static radical stiffness characteristics of non-pneumatic mechanical elastic wheel. *Acta Armamentarii*, vol. 36, no. 2, p. 355-362 (in Chinese)

[20] Li, B., Zhao, Y.Q., Zang, L.G. (2014). Closed-form solution of curved beam model of elastic mechanical wheel. *Journal of Vibroengineering*, vol. 16, no. 8, p. 3951-3962.

[21] Du, X.B., Zhao, Y.Q., Wang, Q., Fu, H.X. (2017). Numerical analysis of the dynamic interaction between a non-pneumatic mechanical elastic wheel and soil containing an obstacle. *Proceedings of the Institution of Mechanical Engineers, Part D: Journal of Automobile Engineering*, vol. 231, no. 6, p. 731-742, **DOI:10.1177/0954407016660946**.

[22] Du, X.B., Zhao, Y.Q., Lin, F., Fu, H.X., Wang, Q. (2017). Numerical and experimental investigation on the camber performance of a non-pneumatic mechanical elastic wheel. *Journal of the Brazilian Society of Mechanical Sciences and Engineering*, vol. 39, no. 9, p. 3315-3327, **DOI:10.1007/s40430-016-0702-8**.

[23] Akrache, R., Lu, J. (2011). Integrated design for fatigue life estimation of structures. *Strojniški vestnik - Journal of Mechanical Engineering*, vol. 57, no. 7-8p. 547-554, **DOI:10.5545/sv-jme.2008.043**.

[24] Sokolov, S.L. (2010). Prediction of the fatigue life of pneumatic tires. Journal of Machinery Manufacture and Reliability, vol. 39, no. 5, p. 459-465, **DOI:10.3103/S1052618810050092**.

[25] Sokolov, S.L. (2007). Calculation of the stress-strain state of pneumatic tires by the finite element method. *Journal of Machinery Manufacture and Reliability*, vol. 36, no. 1, p. 45-49, **DOI:10.3103/S1052618807010098**.

[26] Topac, M.M., Ercan, S., Kuralay, N.S. (2012). Fatigue life prediction of a heavy vehicle steel wheel under radial loads by using finite element analysis. *Engineering Failure Analysis*, vol. 20, no. 3p. 67-79, **DOI:10.1016/j.engfailanal.2011.10.007**.

[27] Rosa, U., Nagode, M., Fajdiga, M. (2007). Evaluating thermo-mechanically loaded components using a strain-life approach. *Strojniški vestnik - Journal of Mechanical Engineering*, vol. 53, no. 10, p. 605-620.

[28] Aghdam, N.J., Hassanifard, S., Ettefagh, M.M., Nanvayesavojblaghi, A. (2014). Investigating fatigue life effects on the vibration properties in friction stir spot welding using experimental and finite element modal analysis. *Strojniski vestnik - Journal of Mechanical Engineering*, vol. 60, no. 11, p. 735-741, **DOI:10.5545/sv-jme.2013.1324**.

[29] Saoudi, A., Bouazara, M. Marceau, D. (2011). Fatigue failure study of the lower suspension vehicle arm using a multiaxial criterion of the strain energy density. *Strojniski vestnik - Journal of Mechanical Engineering*, vol. 57, no. 4, p. 345-356, **DOI:10.5545/sv-jme.2009.074**.

[30] Su, H. (2010). Automotive structural durability design using dynamic simulation and fatigue damage sensitivity techniques. *SAE International Journal of Materials & Manufacturing*, vol. 3, no. 1, p. 1-12, **DOI:10.4271/2010-01-0001**.

[31] Park, D.W., Papagiannakis, A.T., Kim, I.T. (2014). Analysis of dynamic vehicle loads using vehicle pavement interaction model. *KSCE Journal of Civil Engineering*, vol. 18, no. 7, p. 2085-2092, **DOI:10.1007/s12205-014-0602-3**.

[32] Buch, A. (1988). *Fatigue Strength Calculation*. Trans Tech Publication, Zürich.

List of reviewers who reviewed manuscripts in 2017

Hamidreza Abbasi, Iran
Boris Aberšek, Slovenia
Azhar B. Abu Bakar, Malaysia
Bachir Achour, Tunisia
Mohamed M.Z. Ahmed, Egypt
Mehmet Akar, Turkey
Veysel Alankaya, Turkey
Dragan Aleksendrić, Serbia
Khalil Alipour, Iran
Miha Ambrož, Slovenia
Manuel Arias-Montiel, Mexico
Ciril Arkar, Slovenia
Slave Armenski, R. Macedonia
Kamil Arslan, Turkey
Viktor P. Astakhov, USA
Eugen Axinte, Romania
Azridjal Aziz, Indonesia
Gytautas Balevičius, Lithuania
Sebastian Baloš, Serbia
Jani Barle, Slovenia
Stuart Barnes, UK
Branko Bauer, Slovenia
Bernd-Arno Behrens, Germany
Saoussen Belghith, Tunisia
Aleš Belšak, Slovenia
Károly Beneda, Hungary
Anton Bergant, Slovenia
Mustafa Kemal Bilici, Turkey
Cristina Maria Biris, Romania
Chris Blenkinsopp, UK
Ana Madevska Bogdanova, R. Macedonia
Miha Boltežar, Slovenia
Andrej Bombač, Slovenia
Éd Claudio Bordinassi, Brazil
Marek Boryga, Poland
Francesco Bottiglione, Italy
Jean Bouyer, France
Josip Brnić, Croatia
Blaž Brodnik Žugelj, Slovenia
Stijn Broekaert, Belgium
Miha Brojan, Slovenia
Adam Bureček, Czech Republic
Helena Burger, Slovenia
Peter Butala, Slovenia
Michele Calì, Italy
Paolo Casoli, Italy
Ramón Barber Castaño, Spain
Kadir Cavdar, Turkey
H. Kursat Celik, Turkey
Yikai Chen, China
Peng Cheng, USA
Eliodoro Chiavazzo, Italy
Leszek Marek Chybowski, Poland
Oğuz Çolak, Turkey
Franco Concli, Italy
Eduardo Corral, Spain
Dario Croccolo, Italy
Vesna Čančer, Slovenia
Gregor Čepon, Slovenia
Martin Česnik, Slovenia
Lucija Čoga, Slovenia
Franci Čuš, Slovenia
Doriana Marilena D'Addona, Italy
José Gilberto Dalfré Filho, Brazil
Piotr Danielczyk, Poland
Jos Darling, UK
Massimiliano De Agostinis, Italy
Mariusz Deja, Poland
Zhangxian Deng, USA
Baila Diana Irinel, Romania
Burak Dikici, Turkey
Zlate Dimkovski, Sweden
Anselmo Eduardo Diniz, Brazil
Igor Drstvensek, Slovenia
Dina V. Dudina, Russian Federation
Matevž Dular, Slovenia
Manar Abd Elhakim Eltantawie, Egypt
Igor Emri, Slovenia
Selcuk Erkaya, Turkey
Xavier Escaler, Spain
Patrice Estellé, France
Alessandro Fasana, Italy
Michel Feidt, France
Imre Felde, Hungary
Liljana Ferbar Tratar, Slovenia
Cuneyt Fetvaci, Turkey
Tomasz Figlus, Poland
Paulo Flores, Portugal
Agostino Gambarotta, Italy
Laszlo Garbai, Hungary
Andrés Gabriel García, Argentina
Ehsan Ghassemali, Singapore
Gilbert-Rainer Gillich, Romania
Patrick Glouannec, France
Adam Glowacz, Poland
Sandro Goñi, Argentina
Darko Goričanec, Slovenia
Niccolò Grossi, Italy
Janez Grum, Slovenia
Lucjan Gucma, Poland
Huseyin Gurbuz, Turkey
Leo Gusel, Slovenia
Shivakanth Gutta, USA
Witold Habrat, Poland
Reinhard Hackenschmidt, Germany
Miroslav Halilovič, Slovenia
Guangbo Hao, Ireland
Boštjan Harl, Slovenia
Marek Hawryluk, Poland
Zeyin He, China

The Editorial would like to thank all the reviewers in participating in reviewing process.
We appreciate the time and effort and greatly value the assistance as a manuscript reviewer for Strojniški vestnik – Journal of Mechanical Engineering.

Vsebina

Strojniški vestnik - Journal of Mechanical Engineering
letnik 64, (2018), številka 1
Ljubljana, januar 2018
ISSN 0039-2480

Izhaja mesečno

Razširjeni povzetki (extended abstracts)

Strojniški vestnik - Journal of Mechanical Engineering 64(2018)1, SI 3

Prejeto v recenzijo: 2017-03-29
Prejeto popravljeno: 2017-06-15
Odobreno za objavo: 2017-08-29

Integrativen proces konstruiranja na podlagi CAE v fazi snovanja konstrukcije vozila L7e

Roman Pawel Jedrzejczyk[1,*] – Michael Sigmar Alb[1,2] – Thomas Jost[1]
[1] Raziskovalno središče VIRTUAL VEHICLE, Avstrija
[2] Univerza v Padovi, Italija

Strojna industrija zadnje desetletje išče metodiko konstruiranja, ki bi sistematično poenotila podporo orodij CAE v procesu konstruiranja. Bili so razni poskusi kombiniranja inženirskih in numeričnih orodij za konstruktorje, s katerimi naj bi izboljšali potek procesa konstruiranja. Čeprav je marsikateri projekt privedel do izboljšanja posameznih korakov oz. faz konstrukcijskega procesa, pa uporabnost konstrukcijskih procesov na osnovi simulacij še vedno ni bila kos zahtevam industrije.

V zadnjem času je bilo predstavljenih več predlogov za konstrukcijske procese na osnovi CAE (CDDP), katerih učinkovitost je vprašljiva. Mnogi CDDP so opredeljeni preveč na široko, zato povezave med koraki CDDP ostajajo nejasne in v večini primerov nezadostne. Drugi pristopi k CDDP omogočajo uporabo široke palete različne programske opreme in orodij, s čimer pa se poveča tveganje ponavljanja vmesnikov med procesi. Industrija zato potrebuje preprosto in univerzalno metodologijo za CDDP, ki jo bo mogoče preprosto prilagoditi specifičnim pogojem in potrebam v industriji.

Avtorji so podali predloge izboljšav in novih rešitev za integrativen proces konstruiranja na podlagi CAE (ICDDP), s katerim postane proces CDDP zanesljivejši, učinkovitejši in bolj predvidljiv. ICDDP na novo opredeljuje vlogo orodij CAE ter pozicionira optimizacijsko tehnologijo kot gonilno silo celotnega konstrukcijskega procesa. Faze konstruiranja v ICDDP za sekvenčno vodenje procesa so: (1) konceptualna zasnova, (2) kristalizacija zasnove in (3) dovršitev zasnove. Natančno opredeljene povezave med zaporednimi koraki omogočajo nemoteno ponavljanje korakov ICDDP pri novih izdelkih. V korakih ICDDP je uporabljen samo en programski paket za simulacije (Altair OptiStruct®), kjer so zbrane ključne metode za optimizacijo in simulacijo. V ICDDP bo po potrebi mogoče integrirati tudi druge vrste programske opreme. Programska oprema za simulacije ne zahteva niti dodatnega znanja niti posebnega usposabljanja uporabnikov. Glavni koraki in faze konstruiranja ICDDP so univerzalni in za izvedbo je mogoče uporabiti tudi drugo programsko opremo z nujnimi simulacijskimi in optimizacijskimi metodami – delno ali povsem znotraj izbranega programskega okolja.

V članku je predstavljena tudi uporaba faze konceptualne zasnove pri načrtovanju konstrukcije novega vozila L7e (eQuad). Ta faza ICDDP ilustrira posebno metodologijo za vodenje optimizacije topologije konstrukcije novega vozila eQuad, kakor tudi korak izpeljave geometrijske rešitve, ki razkriva pretvorbo bionskih oblik v grobo izvedljivo geometrijo. Inženirji in konstruktorji aktivno iščejo možnosti za uporabo različnih materialov pri gradnji lahkih konstrukcij in v tem delu je predstavljena posplošitev rezultatov optimizacije topologije, ki uporablja rezultate za en material pri pripravi zasnove konstrukcije iz drugega materiala. Še pomembnejši prispevek je funkcionalna metodologija za boljše razumevanje rezultatov optimizacije topologije. Za podane obremenitvene primere je podana tudi numerična verifikacija preprostega geometrijskega modela. Rezultati dokazujejo, da je pristop ICDDP primeren za snovanje inovativnih in lahkih konstrukcij oz. za občutno zmanjšanje mase pri novih konstrukcijah. Faza konceptualne zasnove pri ICDDP daje bistveno lažje rešitve kot klasični pristop (za primer brez obremenitev trka). V izvirni zasnovi konstrukcije vozila eQuad so bile obremenitve trka zanemarjene. Nova konstrukcija vozila eQuad, v kateri so upoštevane tudi obremenitve trka, je rezultat prve faze ICDDP z večjo maso (94 kg) kot pri originalni zasnovi (82 kg). Kljub temu pa korak izpeljave geometrijske rešitve (GSD) zagotavlja, da iz prve faze ICDDP z lahko zasnovo izhajajo dragocene konstrukcijske opcije (ICDDP GSD za jeklo 60 kg in za aluminij 40 kg).

Prispevek opisuje orodje, ki je pripravljeno za uporabo in pokriva celoten konstrukcijski postopek z glavnimi razvojnimi koraki in fazami do prvega funkcionalnega prototipa nove konstrukcije. Inženirji bodo lahko z opisanim konstrukcijskim orodjem iskali primerne rešitve za dane zahteve. Postopek poleg tega omogoča načrtovanje novih lahkih konstrukcij povsem od začetka.

Ključne besede: konstruiranje na podlagi CAE, konstrukcija vozila L7e, konceptualna zasnova, topološka optimizacija, lahka konstrukcija, izpeljava geometrijske rešitve

*Naslov avtorja za dopisovanje: Raziskovalno središče VIRTUAL VEHICLE, Inffeldgasse 21/A, 8010 Graz, Avstrija, RomanPawel.Jedrzejczyk@v2c2.at

Strojniški vestnik - Journal of Mechanical Engineering 64(2018)1, SI 4

Prejeto v recenzijo: 2017-06-15
Prejeto popravljeno: 2017-10-18
Odobreno za objavo: 2017-11-06

Uporaba LCS in informacijske entropije v novem združenem algoritmu za identifikacijo značilk slabšanja

Haotian Wang[1] – Jian Sun[2,*] – Xiusheng Duan[1] – Ganlin Shan[1] – Wen Yang[2]

[1] Kolidž za strojništvo, Shijiazhuang 050003, Kitajska
[2] Nacionalno središče za preizkušanje elektronske opreme, Kitajska

Identifikacija značilk slabšanja hidravličnih črpalk je eden glavnih korakov pri vzdrževanju po stanju. Pomembna je tudi za napovedovanje in upravljanje stanja (PHM) hidravličnih črpalk. Predstavljen je algoritem LCS za združevanje signalov o vibracijah, ki v celoti izkorišča razpoložljive informacije o napakah. Predstavljena metoda z združenimi značilnostmi omogoča učinkovitejši opis in uspešno vrednotenje procesa slabšanja hidravličnih črpalk.

Predstavljen je algoritem LCS za združevanje signalov o vibracijah na podlagi prilagojenega tradicionalnega sestavljenega spektralnega algoritma, ki omogoča popolno izkoriščanje informacij o napakah. Za prvi značilki sta bili izbrani entropija močnostnega spektra višjega reda LCS in singularna entropija višjega reda, kot sta opredeljeni v teoriji Shannonove in Tsallisove entropije. Predstavljena je tudi metoda za združevanje značilk na podlagi informacijske entropije, ki uspešno izboljšuje konciznost in učinkovitost metode.

Rezultati analize kažejo, da je predlagana metoda primerna za učinkovito vrednotenje procesa slabšanja črpalke. Tudi iz rezultatov eksperimentov sledi, da združene značilke bistveno učinkoviteje popisujejo proces slabšanja hidravlične črpalke.

Raziskava, v okviru katere je bil napisan pričujoči članek, je končana, obstaja pa več možnih smeri za prihodnje raziskave. Metodo LCD za združevanje signalov vibracij bi bilo mogoče uporabiti tudi v drugih nalogah prepoznavanja vzorcev ali diagnosticiranja napak. Metoda združevanja na podlagi informacijske entropije po drugi strani prinaša določeno izgubo vsebine informacij in v prihodnjih raziskavah bi zato bilo mogoče pristopiti z izboljšanimi pristopi.

Predstavljena je metoda LCS za združevanje signalov o vibracijah, ki omogoča ekstrakcijo podatkov o napakah. Za prvi značilki sta bili izbrani entropija močnostnega spektra višjega reda LCS in singularna entropija višjega reda, ki sta opredeljeni v Shannonovi in Tsallisovi entropiji.

Predlagana je metoda združevanja značilk na podlagi informacijske entropije za izboljšano konciznost in učinkovitost.

Rezultati eksperimentov so pokazali, da združene značilke bistveno učinkoviteje popisujejo slabšanje hidravlične črpalke.

Ključne besede: identifikacija značilk slabšanja, združevanje informacij, dekompozicija na lokalni značilni skali, sestavljeni spekter LCD, informacijska entropija, hidravlična črpalka

*Naslov avtorja za dopisovanje: Luoyang Electronic Equipment Test Center of China, Luoyang 471003, Kitajska, hehetcs@163.com

Strojniški vestnik - Journal of Mechanical Engineering 64(2018)1, SI 5

Prejeto v recenzijo: 2017-10-14
Prejeto popravljeno: 2017-11-27
Odobreno za objavo: 2017-11-29

Numerična raziskava izboljšanja prenosa toplote pri nizkotlačnem toku nanofluida Al_2O_3-zrak v pravokotni kotanji z dvema rebroma na vroči steni

Wael Al-Kouz[1,*] – Suhil Kiwan[2] – Ammar Alkhalidi[3] – Ma'en Sari[4] – Aiman Alshare[1]

[1] Nemško-jordanska univerza, Oddelek za mehatroniko, Jordanija
[2] Jordanska znanstveno-tehniška univerza, Oddelek za strojništvo, Jordanija
[3] Nemško-jordanska univerza, Oddelek za energetiko, Jordanija
[4] Nemško-jordanska univerza, Oddelek za strojništvo in vzdrževanje, Jordanija

V članku je predstavljena numerična raziskava stacionarnega dvodimenzionalnega laminarnega prenosa toplote z naravno konvekcijo pri toku plinastega nizkotlačnega nanofluida skozi pravokotno kotanjo dolžine L z dvema polnima rebroma na vroči steni. Takšni tokovi se pojavljajo pri mnogih tehničnih aplikacijah, kot so denimo jedrski reaktorji in naprave za hlajenje elektronske opreme.

V študiji so bile uporabljene fizikalne veličine v naslednjem razponu: $0 \leq Kn \leq 0.1$, $10^3 \leq Ra \leq 10^6$, $0 \leq \phi \leq 0.2$, $L_F/L = 0{,}5$, $H_F = 0{,}25$ do $0{,}75$. Razpon Knudsenovega števila je bil izbran tako, da pokriva režim zveznega in drsečega toka, medtem ko razpon Rayleighovega števila pokriva vse režime prenosa toplote, od prevladujočega prevoda do prevladujoče konvekcije.

Za simulacijo je bila uporabljena tehnika končnih volumnov z adaptivno mrežo. Opravljen je bil tudi preskus neodvisnosti mreže za ugotavljanje vpliva števila elementov v mreži na rezultate. Koda, ki je bila uporabljena za vse simulacije, je bila validirana na več primerih iz literature in rezultati simulacij se odlično ujemajo s podatki iz literature.

Rezultati simulacij kažejo, da je Nusseltovo število sorazmerno z Rayleighovim številom in obratno sorazmerno s Knudsenovim številom. Ugotovljeno je bilo tudi, da se prenos toplote izboljša z razpršitvijo nanodelcev Al_2O_3 v osnovnem nizkotlačnem plinastem toku. V razponu volumskih deležev, ki je bil obravnavan v študiji, se je izkazalo, da se Nusseltovo število povečuje z volumskim deležem nanodelcev. Določena sta bila tudi hitrostni in temperaturni profil vzdolž središčnice kotanje pri različnih Knudsenovih in Rayleighovih številih za prikaz drsenja in temperaturnega skoka na mejah. Izrisane so tudi tokovnice in izoterme za različne vrednosti Knudsenovega števila in volumskega deleža nanodelcev. Končno je podana še funkcijska zveza med vsemi obravnavanimi veličinami in Nusseltovim številom: $Nu = 0{,}2196\ Ra^{0{,}0829}\ Kn^{-0{,}511}\ \phi^{0{,}104}$. Ta zveza predstavlja prispevek na področju znanosti prenosa toplote v nanofluidih in bo v pomoč inženirjem pri projektiranju termodinamičnih sistemov s tovrstnimi tokovi. Šibka odvisnost Nusseltovega števila od Rayleighovega števila v funkcijski zvezi izhaja iz obravnavanega razpona Rayleighovega števila. Na podlagi predlagane zveze je mogoče izrisati več glavnih krivulj za prikaz vpliva preučevanih veličin na Nusseltovo število. Prikazana je ena glavna krivulja.

V prihodnjih študijah bi bilo mogoče razširiti razpon fizikalnih veličin in tako pokriti širši razpon volumskega deleža nanodelcev in Rayleighovega števila za režim prenosa toplote s prevladujočo konvekcijo. Preučiti bi bilo mogoče tudi različne lokacije reber in vpliv kota nagiba na Nusseltovo število. Ena od možnih raziskovalnih tem je tudi vpliv poroznosti reber.

Ključne besede: naravna konvekcija, prenos toplote, nizek tlak, kotanja, nanofluid, rebro

*Naslov avtorja za dopisovanje: Nemško-jordanska univerza, Oddelek za mehatroniko, Jordanija, wael.alkouz@gju.edu.jo

Strojniški vestnik - Journal of Mechanical Engineering 64(2018)1, SI 6

Prejeto v recenzijo: 2017-08-01
Prejeto popravljeno: 2017-11-24
Odobreno za objavo: 2017-12-11

Analiza stanja pri transportu razsutega premoga na transporterju s strgali po metodi diskretnih elementov

Xuewen Wang* – Bo Li – Zhaojian Yang
Tehniška univerza v Taiyuanu, Kolidž za strojništvo, Kitajska

Transporterji s strgali so glavna oprema za transport premoga v premogovnikih, od njihovega stanja pa sta odvisna proizvodna zmogljivost in rentabilnost podjetja. Malo je študij, ki bi obravnavale lastnosti materiala v fazi transporta ter interakcije med premogom in transporterjem s strgali, še manj pa jih natančno opisuje razmerja med transportom razsutega tovora in delovnimi stanji transporterja s strgali. Zaradi pomanjkanja raziskovalnih podatkov prihaja do odstopanj pri varnosti, zanesljivosti in učinkovitosti transporta, ki vplivajo na celoten proces transporta materiala. Cilji študije so bili naslednji: (1) opredelitev modela interakcije med razsutim premogom in transporterjem s strgali s programskim paketom EDEM; (2) preučitev porazdelitve velikosti in hitrosti kosov premoga pri različnih pogojih, kot so različne transportne hitrosti, transportni kot, hitrost podajanja in višina rudarjenja; ter (3) preučitev vpliva hitrosti transporta in količnika statičnega trenja na masni pretok.

Za preučitev interakcij med transporterjem s strgali in premogom je bila uporabljena metoda diskretnih elementov (DEM). Model žleba je bil izdelan s programsko opremo NX7.5 UG (Siemens PLM, München, Nemčija), model razsutega premoga pa je bil narejen v paketu EDEM. Določeno je bilo stabilno referenčno stanje in nato so bile uporabljene različne vrednosti parametrov za preučitev delovanja transporterja v različnih pogojih. Porazdelitev velikosti delcev in hitrosti razsutega premoga je bila analizirana pri različnih transportnih hitrostih, transportnih kotih, hitrostih podajanja in višinah rudarjenja s spreminjanjem transportnih pogojev na transporterju. Preučen je bil tudi vpliv hitrosti transporta, količnika statičnega trenja in masnega pretoka.

Rezultati kažejo, da je model interakcije v paketu EDEM uporaben za simulacijo delovnega procesa transporterja s strgali. Pridobljeni so bili obratovalni parametri v različnih razmerah, ki bi jih bilo težko določiti z eksperimenti. Ugotovljeno je bilo tudi, da porazdelitev velikosti kosov premoga ni povezana s parametri transportnega stanja v fazi stabilnega transporta. Večji kosi se med transportom zbirajo na višje ležečih, manjši kosi pa na nižje ležečih mestih. Hitrost razsutega premoga v sprednjem predelu transporterja s strgali je bila enaka hitrosti strgal, medtem ko je bil premog na drugih mestih počasnejši. Masni pretok razsutega premoga se je povečeval z večanjem hitrosti transporta in je največjo vrednost dosegel pri vrednosti količnika statičnega trenja med kosi 0,4. DEM lahko odpravi pomanjkljivosti MKE pri preučevanju gibanja ter sil med delci, kot so kosi razsutega premoga, in tako omogoča pripravo zanesljivejše teoretične osnove za razvoj in projektiranje transporterjev s strgali.

Omeniti je treba, da zgornji zaključki veljajo le za posebno obliko kosov (sestavljenih iz štirih krogel) in za tri različne velikosti (0,5, 1 in 1,3). Vedenje v drugačnih razmerah bo treba šele raziskati. Rezultat študije je metoda za analizo porazdelitve velikosti in hitrosti kosov premoga v različnih pogojih, ki je primerna tudi za preučevanje masnega pretoka. Študija bo pomagala premogovnikom pri nadzoru transporta razsutega premoga in transportne zmogljivosti transporterjev s strgali v različnih pogojih. Projektanti bodo lahko z analizo porazdelitve velikosti in hitrosti kosov premoga preučevali mehanizme obrabe za optimizacijo konstrukcije transporterja s strgali in doseganje protiobrabne obstojnosti srednjega žleba, s tem pa daljše življenjske dobe transporterja.

Ključne besede: transporter s strgali, razsuti premog, metoda diskretnih elementov (DEM), masni pretok

*Naslov avtorja za dopisovanje:Tehniška univerza v Taiyuanu, Kolidž za strojništvo, Taiyuan, Kitajska, wxuew@163.com

Strojniški vestnik - Journal of Mechanical Engineering 64(2018)1, SI 7

Prejeto v recenzijo: 2017-08-03
Prejeto popravljeno: 2017-11-20
Odobreno za objavo: 2017-11-22

Nelinearno vodenje robotskega manipulatorja s fleksibilnim zgibom in eksperimentalna validacija

Waqar Alam[1] – Adeel Mehmood[1] – Khurram Ali[1] – Usman Javaid[1] – Soltan Alharbi[2] – Jamshed Iqbal[2,3,*]

[1] Oddelek za elektrotehniko, Inštitut za informacijske tehnologije COMSATS, Islamabad, Pakistan
[2] Oddelek za elektrotehniko in računalništvo, Univerza v Dždedi, Saudova Arabija
[3] Oddelek za elektrotehniko, Nacionalna univerza FAST, Islamabad, Pakistan

Glavna skrb pri industrijskih aplikacijah je natančno vodenje vrha manipulatorja po zahtevani trajektoriji. Predlaganih je bilo že veliko algoritmov za vodenje gibanja manipulatorja po trajektoriji, toda ker te metode vodenja pogosto ne upoštevajo trenja, elastičnosti zgibov in dinamike aktuatorjev, manipulatorji ne dosegajo želene točnosti trajektorije in zato prihaja do nezaželenih oscilacij okrog želenega položaja in težav pri vodenju.

Zahteva po visoki točnosti in hitrosti robotskih manipulatorjev predstavlja zahteven raziskovalni problem. Zaradi teh zahtev in omejitev se pojavljajo različni izzivi na področju vodenja.

Cilj predstavljene raziskave je zasnova in implementacija robustnih nelinearnih pristopov k vodenju za sledenje manipulatorja s fleksibilnim zgibom po želeni trajektoriji in posledično točno sledenje vrha želenemu kotnemu položaju. V sistemu so modelirane negotovosti, kot so trenje, elastičnost zgiba in dinamika aktuatorjev, ki v sistem vnašajo nelinearnost. Dinamika modela sistema je bila izpeljana po Euler-Lagrangeovi metodi. Sistem ima dve prostostni stopnji.

Zasnovana je bila nelinearna shema vodenja z drsnim režimom (tradicionalni in integralni SMC) za lokalno stabilizacijo zaprtozančnega sistema v vseh stanjih. Za eksperimentalno validacijo predlaganih zakonov vodenja je bil zasnovan in izdelan električni fleksibilni manipulator z enim členom. Zasnovani krmilni algoritmi so bili razviti in eksperimentalno validirani na uporabniško razviti platformi. Rezultati, pridobljeni v paketu MATLAB/Simulink in na eksperimentalni platformi, potrjujejo učinkovitost predlaganih krmilnih algoritmov.

Ključne besede: manipulator s fleksibilnim zgibom, krmilni algoritmi, drsni režim vodenja, integralni drsni režim vodenja

*Naslov avtorja za dopisovanje: Department of Electrical Engineering, FAST National University of Computer and Emerging Sciences, H-11/4, Islamabad, Pakistan, jamshed.iqbal@nu.edu.pk

Strojniški vestnik - Journal of Mechanical Engineering 64(2018)1, SI 8

Prejeto v recenzijo: 2017-06-29
Prejeto popravljeno: 2017-12-13
Odobreno za objavo: 2017-12-18

Napovedovanje utrujenostne trajnostne dobe kolesa brez pnevmatike po metodi projektiranja za omejeno življenjsko dobo

Zhen Xiao – You Qun Zhao* – Fen Lin – Ming Min Zhu – Yao Ji Deng
Univerza za aeronavtiko in astronavtiko, Oddelek za avtomobilsko tehniko, Kolidž za energetiko in elektroenergetiko, Kitajska

Kolesa spadajo med najpomembnejše dele vozil, pri vojaških vozilih pa morajo biti še posebej varna pred pokom tudi v različnih ekstremnih okoljih. Da bi se izognili prediranju, spuščanju in ostalim težavam z običajnimi pnevmatikami, je bil razvit in preučen nov tip varnostnega kolesa brez pnevmatike, imenovan mehansko elastično kolo oz. ME-Wheel. Sestavljeno je iz upogljivega telesa, tečajev, sornikov, vpenjalnega obroča, povezanih elastičnih obročev in pesta. Preučena je trajnost kolesa z namenom podaljšanja njegove dobe uporabnosti. Določiti je mogoče tudi najboljši interval za preventivno vzdrževanje, ki zagotavlja varnost in zanesljivost kolesa ME-Wheel v delovnih pogojih. Kolo je med vožnjo izpostavljeno kompleksnim spreminjajočim se obremenitvam, zato je zelo težko napovedati njegovo dobo uporabnosti. V ta namen je bila najprej uporabljena metoda konstruiranja za končno življenjsko dobo in izdelan je bil model kolesa po MKE, točnost pa je bila nato preverjena na preizkuševališču z nateznim preizkusom.

Rezultati simulacij statične trdnosti kolesa kažejo, da je najšibkejša komponenta sornik, kjer je tudi največja koncentracija napetosti. Z enoosnimi nateznimi preizkusi tečajnih enot je bila potrjena ustreznost modela kolesa ter enote tečajev in sornikov po MKE za simulacijo. Iz rezultatov nateznega preizkusa in simulacije po MKE sledi, da so deformacije tečajne enote posledica upogibnih deformacij sornika. Simulacija po MKE se razmeroma dobro ujema s krivuljo nateznega preizkusa tečajne enote: največja relativna napaka je bila 14,4 % in povprečna napaka 4,9 %. Tako je potrjena ustreznost modela za napovedovanje življenjske dobe kolesa ME-Wheel, ki je bil določen po metodi konstruiranja za omejeno življenjsko dobo. Teoretično življenjsko dobo kolesa je mogoče napovedati razmeroma natančno. Rezultati teoretičnih izračunov so bili primerjani z rezultati simulacije trajnosti in z rezultati vzdržljivostnih cestnih preizkusov, odstopanje pa znaša 5,49 oz. 16,9 %. Nato je bil postavljen še virtualni model preizkuševališča za vozila, s pomočjo katerega je bila opravljena simulacija trajnosti za napoved življenjske dobe kolesa ME-Wheel. Razlika med rezultati simulacije in vzdržljivostnega cestnega preizkusa znaša 12,07 %. To pomeni, da je mogoče z modelom virtualnega preizkuševališča in analizo simulacije vožnje razmeroma točno napovedati življenjsko dobo kolesa.

Teoretični izračuni in simulacije, ki so bili opravljeni v okviru te raziskave za napovedovanje življenjske dobe kolesa ME, se dobro ujemajo z rezultati eksperimentov, predlagana metoda pa je zato primerna tudi za raziskave trajnosti drugih mehanskih konstrukcij. Uporabljena analitična metoda prihrani čas pri preizkušanju in je obenem referenca za nadaljnjo optimizacijo trajnosti kolesa.

Teoretični izračuni za napoved življenjske dobe sornika temeljijo na maksimalni vertikalni obremenitvi (izračunana vrednost je konzervativna), toda izračunana življenjska doba ni dovolj točna, ker so bile v računskem procesu zanemarjene bočne sile in njihov vpliv. Prihodnje raziskave bodo zato osredotočene na analizo omejene življenjske dobe koles v sestavljenih pogojih vožnje naravnost in v ovinek.

Ključne besede: vozilo, kolo brez pnevmatike, trajnost, konstruiranje za omejeno življenjsko dobo, analiza po metodi končnih elementov, preizkus življenjske dobe

*Naslov avtorja za dopisovanje: niverza za aeronavtiko in astronavtiko, No.29 Yudao Street Qinhuai District, Nanjing 210016, Kitajska, yqzhao@nuaa.edu.cn

DOKTORSKE DISERTACIJE

Na Fakulteti za strojništvo Univerze v Ljubljani sta obranila svojo doktorsko disertacijo:

- dne *1. decembra 2017* **Jernej PIRNAR** z naslovom: »Računalniška simulacija toka fluida skozi prožni kanal nespecificiranih oblik z aplikacijo na biološkem sistemu« (mentor: prof. dr. Branko Širok, somentor: doc. dr. Andrej Bombač);

Obstruktivna apneja med spanjem (angl. Obstructive sleep apnoea - OSA) je motnja dihanja v spanju, ki zaradi večnivojskih vzročnih mehanizmov še ni povsem pojasnjena, kar terja nadaljnjo pozornost raziskovalcev različnih strok. S sklopljeno računalniško FSI-simulacijo poskušamo razložiti pojav trepetanja mehkega neba z uvulo in nastanek obstruktivne zapore žrela pri toku zraka skozi zgornjo dihalno pot človeka. Osredinimo se na območje velofarinksa, kjer je podajnost zgornjih dihal najvišja. V fazi vdiha se zaradi subatmosferskega intraluminalnega tlaka pojavi oženje žrela, ob izdihu pa se dihalna pot zaradi nadtlaka razširi. Z računalniško simulacijo napovemo sočasen pojav trepetanja mehkega neba. Frekvenca trepetanja, ki kaže na pojav smrčanja, je enaka 17,8 Hz. Pokažemo, da trepetanje mehkih struktur ni posledica nestabilnosti uporabljene numerične sheme sklopljenja. Ko krajevno skalo opazovanja respiratornega sistema zmanjšamo, razkrijemo, da je tok fluida dvofazen, mehanski sistem pa dvojno sklopljen. Razvijemo in zgradimo fizikalni eksperiment, ki zajema bistvene karakteristike zgornjih dihal - turbulentni curek in recirkulacijo toka ter prožno steno, omočeno s plastjo kapljevinskega filma. Ugotovimo, da se sposobnost dušenja fluktuacij strižne in tlačne obremenitve poveča z večanjem debeline, viskoznosti ali površinske napetosti kapljevinskega filma. S spreminjanjem fizikalnih lastnosti sluzi respiratornega sistema bi zato lahko uravnavali stimulus in aktivacijo mehanoreceptorjev ter posredno vplivali na pojav obstruktivne apneje med spanjem;

- dne *22. decembra 2017* **Blaž BRODNIK ŽUGELJ** z naslovom: »Značilnosti realne kontaktne površine na mikro nivoju« (mentor: prof. dr. Mitjan Kalin);

V splošnem strojništvu se pogoje v kontaktu računa z upoštevanjem nominalne kontaktne površine med dvema površinama, ki je bistveno večja od dejanske kontaktne površine. Upoštevanje takšne predpostavke vodi v izračun milejših kontaktnih pogojev kot so ti v resnici. V doktorski nalogi smo raziskovali vpliv inženirsko relevantnih materialov in topografskih lastnosti na dejansko obnašanje v kontaktu dveh ravnih površin pri statičnih pogojih obremenjevanja. V ta namen je bilo razvito namensko preizkuševališče, ki omogoča analizo kontakta na submikronskem nivoju. Rezultati so pokazali, da se pri doseženi meji tečenja kovine v kontaktu obnašajo zelo podobno, medtem ko so vidnejše razlike posledica različnih topografskih lastnosti. Nasprotno kovinam, polimer izkazuje drugačno obnašanje v kontaktu kot kovine. Podrobna eksperimentalna analiza deformacije vršičkov je pokazala, da na obnašanje v kontaktu pomembno vplivajo tako mehanske kot tudi geometrijske spremembe kontaktnih vršičkov. Eksperimentalne rezultate smo primerjali z najbolj uveljavljenimi teoretičnimi modeli za napovedovanje obnašanja v kontaktu. Zaradi predpostavk, na katerih temeljijo teoretični modeli, prihaja do vidnejših odstopanj v primerjavi z dejanskim obnašanjem v kontaktu.

Information for Authors

All manuscripts must be in English. Pages should be numbered sequentially. The manuscript should be composed in accordance with the Article Template given above. The maximum length of contributions is 10 pages. Longer contributions will only be accepted if authors provide juastification in a cover letter. For full instructions see the Information for Authors section on the journal's website: http://en.sv-jme.eu .

SUBMISSION:

Submission to SV-JME is made with the implicit understanding that neither the manuscript nor the essence of its content has been published previously either in whole or in part and that it is not being considered for publication elsewhere. All the listed authors should have agreed on the content and the corresponding (submitting) author is responsible for having ensured that this agreement has been reached. The acceptance of an article is based entirely on its scientific merit, as judged by peer review. Scientific articles comprising simulations only will not be accepted for publication; simulations must be accompanied by experimental results carried out to confirm or deny the accuracy of the simulation. Every manuscript submitted to the SV-JME undergoes a peer-review process.

The authors are kindly invited to submit the paper through our web site: http://ojs.sv-jme.eu. The Author is able to track the submission through the editorial process - as well as participate in the copyediting and proofreading of submissions accepted for publication - by logging in, and using the username and password provided.

SUBMISSION CONTENT:

The typical submission material consists of:

- A **manuscript** (A PDF file, with title, all authors with affiliations, abstract, keywords, highlights, inserted figures and tables and references),
- Supplementary files:
  - a **manuscript** in a WORD file format
  - a **cover letter** (please see instructions for composing the cover letter)
  - a ZIP file containing **figures** in high resolution in one of the graphical formats (please see instructions for preparing the figure files)
  - possible **appendicies** (optional), cover materials, video materials, etc.

Incomplete or improperly prepared submissions will be rejected with explanatory comments provided. In this case we will kindly ask the authors to carefully read the Information for Authors and to resubmit their manuscripts taking into consideration our comments.

COVER LETTER INSTRUCTIONS:

Please add a **cover letter** stating the following information about the submitted paper:

1. Paper **title**, list of **authors** and their **affiliations**.
2. **Type of paper**: original scientific paper (1.01), review scientific paper (1.02) or short scientific paper (1.03).
3. A **declaration** that neither the manuscript nor the essence of its content has been published in whole or in part previously and that it is not being considered for publication elsewhere.
4. State the **value of the paper** or its practical, theoretical and scientific implications. What is new in the paper with respect to the state-of-the-art in the published papers? Do not repeat the content of your abstract for this purpose.
5. We kindly ask you to suggest at least two **reviewers** for your paper and give us their names, their full affiliation and contact information, and their scientific research interest. The suggested reviewers should have at least two relevant references (with an impact factor) to the scientific field concerned; they should not be from the same country as the authors and should have no close connection with the authors.

FORMAT OF THE MANUSCRIPT:

The manuscript should be composed in accordance with the Article Template. The manuscript should be written in the following format:

- A **Title** that adequately describes the content of the manuscript.
- A list of **Authors** and their **affiliations**.
- An **Abstract** that should not exceed 250 words. The Abstract should state the principal objectives and the scope of the investigation, as well as the methodology employed. It should summarize the results and state the principal conclusions.
- 4 to 6 significant **key words** should follow the abstract to aid indexing.
- 4 to 6 **highlights;** a short collection of bullet points that convey the core findings and provide readers with a quick textual overview of the article. These four to six bullet points should describe the essence of the research (e.g. results or conclusions) and highlight what is distinctive about it.
- An **Introduction** that should provide a review of recent literature and sufficient background information to allow the results of the article to be understood and evaluated.
- A **Methods** section detailing the theoretical or experimental methods used.
- An **Experimental section** that should provide details of the experimental set-up and the methods used to obtain the results.
- A **Results** section that should clearly and concisely present the data, using figures and tables where appropriate.
- A **Discussion** section that should describe the relationships and generalizations shown by the results and discuss the significance of the results, making comparisons with previously published work. (It may be appropriate to combine the Results and Discussion sections into a single section to improve clarity.)
- A **Conclusions** section that should present one or more conclusions drawn from the results and subsequent discussion and should not duplicate the Abstract.
- **Acknowledgement** (optional) of collaboration or preparation assistance may be included. Please note the source of funding for the research.
- **Nomenclature** (optional). Papers with many symbols should have a nomenclature that defines all symbols with units, inserted above the references. If one is used, it must contain all the symbols used in the manuscript and the definitions should not be repeated in the text. In all cases, identify the symbols used if they are not widely recognized in the profession. Define acronyms in the text, not in the nomenclature.
- **References** must be cited consecutively in the text using square brackets [1] and collected together in a reference list at the end of the manuscript.
- **Appendix(-icies)** if any.

SPECIAL NOTES

Units: The SI system of units for nomenclature, symbols and abbreviations should be followed closely. Symbols for physical quantities in the text should be written in italics (e.g. *v*, *T*, *n*, etc.). Symbols for units that consist of letters should be in plain text (e.g. ms^{-1}, K, min, mm, etc.). Please also see: http://physics.nist.gov/cuu/pdf/sp811.pdf .

Abbreviations should be spelt out in full on first appearance followed by the abbreviation in parentheses, e.g. variable time geometry (VTG). The meaning of symbols and units belonging to symbols should be explained in each case or cited in a **nomenclature** section at the end of the manuscript before the References.

Figures (figures, graphs, illustrations digital images, photographs) must be cited in consecutive numerical order in the text and referred to in both the text and the captions as Fig. 1, Fig. 2, etc. Figures should be prepared without borders and on white grounding and should be sent separately in their original formats. If a figure is composed of several parts, please mark each part with a), b), c), etc. and provide an explanation for each part in Figure caption. The caption should be self-explanatory. Letters and numbers should be readable (Arial or Times New Roman, min 6 pt with equal sizes and fonts in all figures). Graphics (submitted as supplementary files) may be exported in resolution good enough for printing (min. 300 dpi) in any common format, e.g. TIFF, BMP or JPG, PDF and should be named Fig1.jpg, Fig2.tif, etc. However, graphs and line drawings should be prepared as vector images, e.g. CDR, AI. Multi-curve graphs should have individual curves marked with a symbol or otherwise provide distinguishing differences using, for example, different thicknesses or dashing.

Tables should carry separate titles and must be numbered in consecutive numerical order in the text and referred to in both the text and the captions as Table 1, Table 2, etc. In addition to the physical quantities, such as *t* (in italics), the units [s] (normal text) should be added in square brackets. Tables should not duplicate data found elsewhere in the manuscript. Tables should be prepared using a table editor and not inserted as a graphic.

REFERENCES:

A reference list must be included using the following information as a guide. Only cited text references are to be included. Each reference is to be referred to in the text by a number enclosed in a square bracket (i.e. [3] or [2] to [4] for more references; do not combine more than 3 references, explain each). No reference to the author is necessary.

References must be numbered and ordered according to where they are first mentioned in the paper, not alphabetically. All references must be complete and accurate. Please add DOI code when available. Examples follow.

Journal Papers:

Surname 1, Initials, Surname 2, Initials (year). Title. Journal, volume, number, pages, DOI code.

[1] Hackenschmidt, R., Alber-Laukant, B., Rieg, F. (2010). Simulating nonlinear materials under centrifugal forces by using intelligent cross-linked simulations. *Strojniški vestnik - Journal of Mechanical Engineering,* vol. 57, no. 7-8, p. 531-538, DOI:10.5545/sv-jme.2011.013.

Journal titles should not be abbreviated. Note that journal title is set in italics.

Books:

Surname 1, Initials, Surname 2, Initials (year). Title. Publisher, place of publication.

[2] Groover, M.P. (2007). *Fundamentals of Modern Manufacturing*. John Wiley & Sons, Hoboken.

Note that the title of the book is italicized.

Chapters in Books:

Surname 1, Initials, Surname 2, Initials (year). Chapter title. Editor(s) of book, book title. Publisher, place of publication, pages.

[3] Carbone, G., Ceccarelli, M. (2005). Legged robotic systems. Kordić, V., Lazinica, A., Merdan, M. (Eds.), Cutting Edge Robotics. Pro literatur Verlag, Mammendorf, p. 553-576.

Proceedings Papers:

Surname 1, Initials, Surname 2, Initials (year). Paper title. Proceedings title, pages.

[4] Štefanić, N., Martinčević-Mikić, S., Tošanović, N. (2009). Applied lean system in process industry. *MOTSP Conference Proceedings*, p. 422-427.

Standards:

Standard-Code (year). Title. Organisation. Place.

[5] ISO/DIS 16000-6.2:2002. *Indoor Air – Part 6: Determination of Volatile Organic Compounds in Indoor and Chamber Air by Active Sampling on TENAX TA Sorbent, Thermal Desorption and Gas Chromatography using MSD/FID.* International Organization for Standardization. Geneva.

WWW pages:

Surname, Initials or Company name. Title, from http://address, date of access.

[6] Rockwell Automation. Arena, from *http://www.arenasimulation.com,* accessed on 2009-09-07.

EXTENDED ABSTRACT:

When the paper is accepted for publishing, the authors will be requested to send an **extended abstract** (approx. one A4 page or 3500 to 4000 characters). The instruction for composing the extended abstract are published on-line: http://www.sv-jme.eu/information-for-authors/ .

COPYRIGHT:

Authors submitting a manuscript do so on the understanding that the work has not been published before, is not being considered for publication elsewhere and has been read and approved by all authors. The submission of the manuscript by the authors means that the authors automatically agree to transfer copyright to SV-JME when the manuscript is accepted for publication. All accepted manuscripts must be accompanied by a Copyright Transfer Agreement, which should be sent to the editor. The work should be original work by the authors and not be published elsewhere in any language without the written consent of the publisher. The proof will be sent to the author showing the final layout of the article. Proof correction must be minimal and executed quickly. Thus it is essential that manuscripts are accurate when submitted. Authors can track the status of their accepted articles on http://en.sv-jme.eu/.

PUBLICATION FEE:

Authors will be asked to pay a publication fee for each article prior to the article appearing in the journal. However, this fee only needs to be paid after the article has been accepted for publishing. The fee is 320 EUR (for articles with maximum of 6 pages), 400 EUR (for articles with maximum of 10 pages), plus 40 EUR for each additional page. The additional cost for a color page is 90.00 EUR. These fees do not include tax.

Strojniški vestnik -Journal of Mechanical Engineering
Aškerčeva 6, 1000 Ljubljana, Slovenia,
e-mail: info@sv-jme.eu

9 770039 248001
ISSN 0039-2480

http://www.sv-jme.eu

Contents

Papers